FEDERAL UNIVERSITY OF ESPÍRITO SANTO
CIVIL ENGINEERING DEPARTMENT
GRADUATE PROGRAM IN CIVIL ENGINEERING

LUCAS FADINI FAVARATO

# ON THE COMPOSITE BEHAVIOR OF A REBAR TRUSS RIBBED SLAB WITH INCORPORATED SHUTTERING MADE OF LIPPED CHANNEL SECTION

VITÓRIA, BRAZIL
2021

LUCAS FADINI FAVARATO

# ON THE COMPOSITE BEHAVIOR OF A REBAR TRUSS RIBBED SLAB WITH INCORPORATED SHUTTERING MADE OF LIPPED CHANNEL SECTION

Master's thesis presented to the Civil Engineering Graduation Program from the Federal University of Espirito Santo as partial fulfillment of the requirement for the Master degree in Civil Engineering.
Research field: Structures.

Supervisors:
Prof. D.Sc. Adenilcia Fernanda Grobério Calenzani
Prof. D.Sc. Juliana da Cruz Vianna Pires

VITÓRIA, BRAZIL
2021

Ficha catalográfica disponibilizada pelo Sistema Integrado de
Bibliotecas - SIBI/UFES e elaborada pelo autor

---

F272o

Favarato, Lucas Fadini, 1994-
On the composite behavior of a rebar truss ribbed slab with incorporated shuttering made of lipped channel section / Lucas Fadini Favarato. - 2021.
111 f. : il.

Orientadora: Adenilcia Fernanda Grobério Calenzani.
Coorientadores: Vianna Juliana da Cruz, Ferrareto Johann Andrade.
Tese (Mestrado em Engenharia Civil) - Universidade Federal do Espírito Santo, Centro Tecnológico.

1. Engenharia de estruturas. 2. Estruturas de aço. 3. Concreto armado. 4. Lajes. 5. Pesquisa experimental. I. Calenzani, Adenilcia Fernanda Grobério. II. Juliana da Cruz, Vianna. III. Johann Andrade, Ferrareto. IV. Universidade Federal do Espírito Santo. Centro Tecnológico. V. Título.

CDU: 624

---

**ON THE COMPOSITE BEHAVIOR OF A REBAR TRUSS RIBBED SLAB WITH INCORPORATED SHUTTERING MADE OF LIPPED CHANNEL SECTION**

Master's thesis presented to the Civil Engineering Graduate Program from the Center of Technology from the Federal University of Espírito Santo as partial requirement to the degree of Master in Civil Engineering (research field: structures).

Approved on August 26th, 2021.

**DEFENSE COMMITTEE:**

Prof. Adenilcia Fernanda Grobério Calenzani, D.Sc.
*Federal University of Espírito Santo (UFES)*
*Supervisor*

Prof. Juliana da Cruz Vianna Pires, D.Sc.
*Federal University of Espírito Santo (UFES)*
*Co-supervisor*

Johann Andrade Ferrareto, D.Sc.
*ArcelorMittal Construction – France, D.Sc. USP*
*Co-supervisor ArcelorMittal*

Prof. Macksuel Soares de Azevedo, D.Sc.
*Federal University of Espírito Santo (UFES)*
*Internal member*

Prof. Rodrigo Barreto Caldas, D.Sc.
*Federal University of Minas Gerais (UFMG)*
*External member*

# ACKNOWLEDGMENTS

To *God*, the most incredible and perfectionist Engineer in this universe, who has given me life and has filled me with peace and strength.

To my parents *Antenor* and *Antonia* and to my sister *Victoria*, to whom I express my immense gratitude. Thank you for making me a man of integrity and honor as well as for giving me values of utmost importance. You are my rock.

To my sweetheart *Larissa* for what we have built together in the last years. Thank you for the patience, the support and, mainly, the love. You've made my way much more joyful and I'm so glad to share it with you! Also, thank you for being such a committed teacher of statistics and for your support on the Laboratory of Structures during this research.

To my supervisor *Prof. D.Sc. Fernanda Calenzani*, whose excellence guided me through this research. In addition to the humanity, to the professionalism and to the open-mindedness, thank you for the friendship, for the motivation and for the interest in my projects. I deeply acknowledge you for awaking my interest into steel construction. You are an outstanding example of professional and person.

To my co-supervisor *Prof. D.Sc. Juliana Vianna*, whose advices toward this research were highly appreciated. Thank you so much for the support and for the friendship too. I cannot put down in words how much I acknowledge you.

To my co-supervisor and friend *D.Sc. Johann Ferrareto,* who supported me a lot toward this research. Besides, thank you for the friendship, for the opportunities and for the time you dedicated to this fascinating project. It has been such an honor to work with you since 2018.

To *Daniel Candido* and *André Vasconcelos*, partners in this research, for the valuable discussions on the behavior of the slab system analyzed in here. Moreover, thank you for the friendship and for your collaboration in all papers we've written together. *Daniel*, your support at the laboratory was highly appreciated.

Special thanks to my uncle *Mauricio Fadini* who supported me in the production of some testing apparatus. Moreover, I'd like to expand the acknowledgements to my cousin *Prof. D.Sc. Rodrigo Fadini* for sharing helpful insights on static analysis.

To *Alexandre Gama*, the Head of Construction Development Area at ArcelorMittal Brazil FCLATAM. Thank you for being supportive and opened in all kinds of discussions. My immense gratitude to you for all the opportunities and, mostly, for the trust.

To my estimated colleagues and co-workers *Luis Augusto Pupin, Jetson Lemos Ferreira, Angela Duarte, Cintia Rodrigues, Eliana Scopel* and *Rui Matos* from ArcelorMittal R&D for the support not only in this research but also on the other pleasant projects we carry out together. Besides, I'd like to thank *Renata Obiala* for the cooperation and valuable discussions on composite steel and concrete field in the past year.

To my colleagues *Christien Hauegen, Eduardo Machado, Henrique Severiano, Bruno Kneipel, Juliovany Drumond, José Tepedino* and *Claudeir Silveira* from ArcelorMittal Flat Carbon Steel for the support on the demands arisen from this research.

To *CAPES – Coordenação de Aperfeiçoamento de Pessoal de Nível Superior* on account of the research grant provided in the first months of the Master's.

To *ArcelorMittal,* for the financial support during this research.

To *Prof. D.Sc. Ronaldo Pilar* for the assistance in all stages of the experimental program. Thank you for dedicating your time to support me on concrete casting and curing, on control of concrete specimens and, essentially, on the shared knowledge to accomplish the results shown herein. Working with you was an honor.

To *Prof. D.Sc. Patrício Pires* for the readiness and the support not only throughout this research, but since the beginning of my professional career. I'm honored to have you as a friend.

To *Prof. D.Sc. Macksuel Azevedo* and *Prof. D.Sc. Rodrigo Caldas* due to the availability to compose the defense committee. Thanks for your valuable remarks and technical contributions that have surely enriched this work.

To *Eric Penedo*, *Ricardo* and *Renato* from Brascontec for the support to our research by testing our thirty-six concrete samples. Your assistance was highly appreciated.

To *Breno, Márcio* and *Henrique* for the support in all experiments conducted at the Federal University of Espírito Santo. My most sincere "thank you" for the excellence and readiness during execution of my experimental program.

To *Reginaldo* who supported me in the preparation and execution of wood formworks as well as propping installation to all the slab samples.

To *Alessandro* and *Wallace* from Envix Engenharia for the support with activities at the lab.

To all my colleagues and family for the friendship and support.

To *Anália, Cleto, Hilda, Isolina* and *Octávio* due to the love and encouragements during my entire life. I miss you a lot.

To you, *reader*, for your interest.

# ABSTRACT

FAVARATO, L. F. **On the composite behavior of a rebar truss ribbed slab with incorporated shuttering made of lipped channel section.** 2021. 111p. Master's Thesis – Civil Engineering Graduate Program, Federal University of Espírito Santo. Vitória, 2021.

Composite slabs are high-performant structural elements made of concrete and of structural cold-formed steel sections, mechanically connected to grant the shear transfer between them. Furthermore, they play an important role in design of structures due to the dead load reduction as well as loads into foundations. On account of increased demand for industrialized systems for buildings, composite slabs can produce great impact in reduction of floor depth while spanning longer to meet architectural needs for column-free areas. In this context, a novel system was recently released in the market as an optimized version of the reinforced concrete ribbed slabs, although made of a cold-formed steel lipped channel section as permanent shuttering fastened to a rebar truss through uniformly distributed plastic connectors. Likewise, light filling blocks usually made in Expanded Polystyrene are employed between ribs to reduce dead loads. However, the shear behavior between shuttering and concrete at bottom ribs had not been fully investigated through full-scale experiments, reason why it's still designed as a non-composite system. Data found in the literature has evidenced full-interaction between both structural materials when tested with span of $2500\ mm$ and shear span of $625\ mm$ $(L/4)$, although it's insufficient to draw a safe conclusion regarding its shear behavior. As such, this research expanded the aforementioned test scope to include extra four-point bending tests according to the EN 1994-1-1 (CEN, 2004) with same span of $2500\ mm$, however with a larger shear span of $833\ mm$ $(L/3)$. Additionally, reinforced concrete slabs with same dimensions and without the steel shuttering were cast and tested under identical conditions to quantify the formwork contribution to the slab strength. It was observed that the lipped channel steel profile fully interacted with concrete with no end-slips, which has increased the characteristic bending resistance in more than $80\%$ while soaring the ductility in five times when compared to the concrete slabs without the steel shuttering. Finally, seven models found in the literature to calculate the effective moment of inertia were compared with testing results, from which the cracked stiffness approach yielded to best results.

**Keywords:** rebar truss composite slab; full-interaction design; lipped channel steel section; four-point bending test; effective moment of inertia; longitudinal shear.

# RÉSUMÉ

FAVARATO, L. F. **Analyse du comportement des dalles nervurées à poutrelles en treillis avec coffrage en profil U formé à froid.** 2021. 111p. Dissertation du Master – Programme d'Études Supérieures en Génie Civil, Université Fédérale d'Espírito Santo. Vitória, 2021.

Les dalles mixtes sont des éléments structuraux très performants constitués par de béton et par de profilés structuraux en acier formés à froid, reliés pour assurer le transfert du cisaillement entre eux. En plus, elles jouent un rôle important dans la conception des structures en ce qui concerne la réduction des charges permanentes et des charges dans les fondations. En raison de la demande croissante de systèmes industrialisés pour les bâtiments, les dalles composites peuvent avoir un impact important sur la réduction de la hauteur des planchers tout en ayant une portée plus grande pour répondre aux besoins architecturaux des régions sans poteau. Dans ce contexte, un nouveau système a récemment été lancé sur le marché comme une version optimisée des dalles nervurées traditionnelles en béton armé, mais composé d'une section en U en acier formé à froid, sujet à flexion par rapport au petit axe, comme coffrage permanent fixé à un treillis d'armature par des connecteurs en plastique uniformément répartis. De même, des hourdis en polystyrène expansé sont utilisés entre les nervures pour réduire les charges permanentes. Cependant, le comportement au cisaillement entre le coffrage et le béton au niveau des nervures inférieures n'a pas été entièrement étudié par des essais en vraie grandeur, raison pour laquelle il est toujours conçu comme un système non mixte. Alors que les données trouvées dans la littérature ont mis en évidence une interaction complète entre les deux éléments structurels essayé avec une portée de $2500\,mm$ et une portée de cisaillement de $625\,mm\,(L/4)$, elles sont insuffisantes pour s'assurer sur son comportement au cisaillement. Ainsi, cette recherche a élargi le programme expérimental susmentionné pour comprendre un groupe supplémentaire d'essais de flexion quatre points selon la norme EN 1994-1-1 (CEN, 2004) avec la même portée de $2500\,mm$, mais avec une portée de cisaillement plus grande de $833\,mm\,(L/3)$. Alors, des dalles en béton armé de mêmes dimensions - mais sans le coffrage en acier - ont été coulées et testées dans des conditions identiques afin de quantifier la contribution du coffrage à la résistance finale de la dalle. Par conséquence, le profilé d'acier en U a pleinement interagi avec le béton sans aucun glissement d'extrémité mesuré, ce qui a augmenté la résistance à la flexion caractéristique de plus de $80\%$ tout en multipliant la ductilité par cinq. Enfin, sept modèles trouvés dans la littérature pour calculer le moment d'inertie effectif ont été comparés aux résultats des essais, parmi lesquels l'approche de la rigidité fissurée a donnée les meilleurs résultats.

**Mots-clés:** dalle mixte avec poutrelles en treillis; conception en interaction totale; profilé en acier en U; essai de flexion quatre points; moment d'inertie effectif; cisaillement longitudinal.

# LIST OF FIGURES

# LIST OF TABLES

## LIST OF INITIALS AND ABBREVIATIONS

| | |
|---|---|
| CC | **C**hemical **C**uring |
| CFS | **C**old-**F**ormed **S**teel |
| CoSFB | **Co**mposite **S**lim **F**loor **B**eam |
| FE | **F**inite **E**lement |
| GHG | **G**reen **H**ouse **G**ases |
| LVDT | **L**inear **V**ariable **D**ifferential **T**ransformer |
| NA | **N**eutral **A**xis |
| PNA | **P**lastic **N**eutral **A**xis |
| PSC | **P**artial **S**hear **C**onnection |
| RC | **R**einforced **C**oncrete |
| SCC | **S**elf-**C**onsolidating **C**oncrete |
| SFB | **S**lim **F**loor **B**eam |
| SG | **S**train **G**auge |
| WC | **W**et **C**uring |

## TABLE OF CONTENTS

# 1

# INTRODUCTION

According to the EN 1994-1-1 (CEN, 2004), composite elements are structural members consisting of concrete and of structural or cold-formed steel (CFS), linked by shear connection to limit the longitudinal slip between them as well as to restrict the separation of one component from the other, achieving a higher performance than the case when both are cast separately. It means that concrete – usually reinforced – contributes to the final strength of a steel beam, slab, column or connection, which brings about advantages such as reduction in structural steel consumption, savings in transport, structural stability, reduction in floor's depth, increase in construction speed, reduction and/or elimination of temporary shuttering and propping and, mainly, sustainability (COUCHMAN; MULLETT; RACKHAM, 2009; QUEIROZ; PIMENTA; MARTINS, 2012; VIANNA, 2005; VIANNA *et al*., 2007).

Furthermore, the composite design plays an important role in dead load reduction of structures while diminishing loads on foundations. In this scenario, composite floors have been considered as ones with highest impact in the weight of buildings and it's getting more relevant with the demand for high column spacing (AHMED; TSAVDARIDIS, 2019). Braun, Hechler and Birarda (2009), for example, reported a case study in which a 140 m² column free space was achieved on account of an innovative floor system, combining composite slim floor beams (CoSFB) and steel decking. This brought about flexibility and economy in construction as well as it fulfilled the requirements for sustainability, with efficient use of raw material and slender steel members when compared to the traditional slim floor beam (SFB).

In a formal manner, composite slabs are efficient systems employed in frame building that bring together a cold-formed steel sheeting and structural concrete as a single structural element to support external loads (GROSSI; SANTOS; MALITE, 2020). As such, the profiled shuttering supports the wet concrete and other construction loads during execution phase and, when concrete reaches 75% of its compressive strength, it gets incorporated to the slab, partial or fully working as tensile reinforcement. Hence, the composite action is set.

However, if the load-carrying capacity is not enough, the reinforcement area can be increased by incrementing shuttering thickness or by adding steel bars in concrete slab (GHOLAMHOSEINI *et al*., 2014; PEREIRA; SIMÕES, 2019).

Nevertheless, the interface between hardened concrete slab and shuttering is responsible for transferring shear between both elements, allowing them to work compositely. In most of cases, the loss of connection under medium spans is recognized as a compelling ultimate limit-state of these slabs (GHOLAMHOSEINI, 2018; YI *et al*., 2021). In this scenario, the development of high-performance technologies to bond both components has been deeply investigated in the literature, such as Ferrer, Marimon and Casafont (2018) who proposed and patented crown-shaped cuttings in the profile webs in replacement to embossments. The solution was tested on commercial profiles, granting the full interaction until complete failure of all assessed samples.

Whereas the load capacity of composite slabs is defined after concrete curing, Lawson and Popo-Ola (2013) state that the construction condition determines the largest achieved span or the amount of propping to preserve structural integrity of shuttering during concrete pouring. On account of increased width-to-thickness ratios from cross-sectional elements, cold-formed members are susceptible to premature buckling under compression and can have their strength and stiffness affected (DAR *et al*., 2020; QIAO *et al*., 2020; ZHANG *et al*., 2020).

Meanwhile, concerns about sustainable development have gained popularity among project owners, business stakeholders and general contractors. The traditional investment-oriented approach that prevailed hitherto is giving rise to project analysis procedures based on life-cycle performance of solutions for buildings. As such, material made of renewable and recyclable sources can sharply contribute to reductions in green-house gases (GHG) emissions as well as to savings in net fresh water consumption during fabrication (WALDMANN; MAY; THAPA, 2017).

That's why composite elements are commonly praised as sustainable systems, mainly steel on account of environmental performance and its efficiency. For example, although construction industry in Brazil has not completely handled the full potential of steel construction (DE ANDRADE et al., 2004), ArcelorMittal is the first steelmaking company to issue Environmental Product Declarations (EPD) to all steel solutions according to NBR ISO 14025

(ABNT, 2015) and EN 15804+A1 (CEN, 2013), allowing engineers and professionals to assess sustainable performance of buildings.

It's worth to mention that when composite slabs first appeared in the market in 1938 in the United States and in the end of 1950s in Europe, the cold-formed sheeting was exclusively used as permanent shuttering and, hence, tensile reinforcement bars were needed to support external loads, such as traditional reinforced concrete (RC) slabs (CRISINEL; O'LEARY, 1996; FERRER; MARIMON; CASAFONT, 2018).

So far, there is a system in Brazilian market commercialized under the same conditions, known as Trelifácil® (ARCELORMITTAL BRASIL, 2017b), which must be understood as an improvement of traditional RC rebar truss ribbed slabs (Figure 1a). It's composted by a CFS lipped channel section in minor bending fastened to a rebar truss through uniformly distributed plastic connectors (Figure 1b), being around 80% lighter, safer and more ergonomic than a RC rib during assemble. In addition, it's composed by light filling blocks usually made in Expanded Polystyrene, concrete and additional rebar in the bottom rib if needed. This system is different from the steel deck because the formwork is intermittent over slab extension and, hence, it demands filling blocks to occupy the voids, which means much less productivity. Furthermore, its composite behavior is still unknown.

(a) (b)

**Figure 1.** Structural systems for ribbed slabs: (a) reinforced concrete ribbed slab; and (b) Trelifácil®.
Source: ARCELORMITTAL BRASIL (2017a, b)

To address this problem, this research investigated the mechanical behavior of this rebar truss ribbed slab with incorporated shuttering made of lipped channel section, quantifying the contribution of the cold-formed profile to the final strength and stiffness of slab through full-scale experimental tests.

## 1.1 RESEARCH JUSTIFICATION

According to Mohammed, Karim and Hammood (2017), the employ of slabs with incorporated sheeting brings about cost savings and ease of installations but, at the same time, it requires complex experimental procedures to effectively assess the longitudinal shear strength at the interface between the hardened concrete and steel profile, such the m–k method proposed by Porter and Ekberg (1976) and adapted by design codes as the EN 1994-1-1 (CEN, 2004).

Besides, the interest by steel-concrete composite slabs has grown in the past decades due to economic, social and environmental potential impacts arisen from steel deck design. A bibliographic survey conducted at Scopus database has shown that 742 papers comprising investigations on testing procedures or improvements on the referred system were published between 1970 and 2021, most of them after 2013 (Figure 2a). In this ranking, China leads with 51% of researches while Brazil occupies the tenth position with only 3% (Figure 2b).

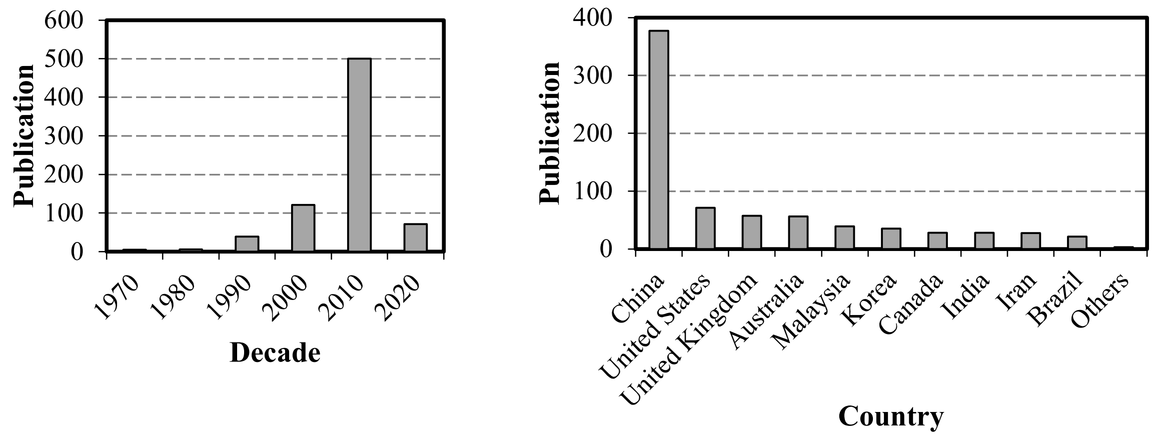


(a) (b)

**Figure 2.** Relevance of composite slab research from Scopus database.
Source: Author.

Regarding the slab system presented herein, the only papers found in the literature proposed an analytical design procedure based on standard codes to assess its resistance, however neglecting any contribution from the CFS section, taking into account only on RC rib strength because, until that moment, its shear behavior was unknown. In addition, the amount of propping was defined taking into consideration barely the CFS section rigidity in minor bending, neglecting the rebar truss reinforcement, which underestimates its real capacity (FAVARATO *et al*., 2019, 2020).

Afterwards, Candido (2021) evaluated the Trelifácil® behavior under flexure through full-scale tests by assessing the strength and stiffness of the system before concrete curing and the load capacity of slab after concrete curing. In addition, Gomes (2020) proposed a finite element model via Ansys to reproduce experimental behavior before concrete curing for different configurations.

Nevertheless, further investigation on the composite phase is needed because Candido (2021) limited his research to the slab strength by performing the four-point bending test into three identical samples with only one shear span. As such, additional data is needed to reach a conclusive remark on the composite behavior of rebar truss ribbed slab with CFS lipped channel section. Finally, to support the calculation of displacements in the serviceability limit-state, models available in the literature still must be validated against experimental data. To summarize, this research bridges the gap in this field for simply supported slabs at room temperature. The objectives are presented in the sequence.

## 1.2 OBJECTIVES

The general purpose of this research is to assess the mechanical behavior of a rebar truss ribbed slab with shuttering made of lipped channel section through four-point bending test as per the EN 1994-1-1 (CEN, 2004), checking if there is any degree of composite action (full or partial).

The specific objectives are:

a) Prepare three full-scale samples of rebar truss ribbed slab with CFS lipped channel section and test them according to the EN 1994-1-1 (CEN, 2004) with a different shear span than found in the literature, referred as TS2.5_16_0.33;
b) Prepare three full-scale samples of rebar truss ribbed slab without shuttering and test them under same procedure according to the EN 1994-1-1 (CEN, 2004), referred as RCS2.5_16_0.33;

c) Compare test results in terms of strength to quantify the CFS lipped channel section influence in the slab resistance;
d) Assess the end-slips between the CFS lipped channel and the concrete ribs as well as the collapse modes;
e) Evaluate if models available in the literature to calculate the displacements of composite slabs are valid to the system investigated here.

## 1.3 STRUCTURE OF THE DISSERTATION

**Chapter one** is dedicated to the introduction. Topics related to the origin of composite slabs, their advantages and innovations are discussed. Then, the objectives, the justification and the structure of the dissertation are presented.

**Chapter two** presents the literature review with regards to standardized guidelines to composite slabs. Also, it focuses on procedures to full-scale experiments addressed to composite slabs.

**Chapter three** declares materials and methods used to carry out the experimental analyses. Tests are detailed with prescriptions, pictures of equipment, instrumentation and schemes of samples.

**Chapter four** shows the experimental results and presents the comparisons settled with analytical equations arisen from the specialized literature. Finally, it addresses discussions regarding the outlined results.

**Chapter five**, finally, is dedicated to present the conclusion of the research and the suggestions for future works and developments.

# 2

# REVIEW OF THE LITERATURE

## 2.1 STANDARDIZED DESGIN OF COMPOSITE SLABS

In accordance with the EN 1994-1-1 (CEN, 2004), sheeting must transfer horizontal shear in the interface with concrete, which can be provided by three mechanisms (DANIELS; CRISINEL, 1993; SOLTANALIPOUR *et al.*, 2020; VIANNA, 2005):

- Chemical bonding: it refers to the bonding between the surface of steel deck and cement paste. In spite of its brittleness and low reliability, this is the first mechanism that actually occurs in composite slabs and no end slip is observed for initial stages of loading as a consequence of its pronounced stiffness (full interaction). Nevertheless, as soon as the first cracks in concrete appear, chemical bonding no more accounts for the shear resistance and, therefore, is not considered in design as an effective connection.

- Mechanical interaction: it stems from the interaction near changes in the sheeting's geometry, such as embossments. The shear resistance in the most decks can be attributed to mechanical interlocking. To be sure, its efficiency is strongly dependent on the embossments' shape.

- Frictional interaction: it is proportional to the normal forces applied at the interface between steel shuttering and concrete. In fact, it arises from concrete confining in steel re-entrant profiles or at the supports of the composite slab. Whenever no embossments are provided, the steel section deformations in serviceability guarantee the frictional interlocking.

It's important to state that mechanical and frictional interlocking represent the same phenomenon, however under different geometric conditions. In addition, once the chemical bond disappears, mechanical and frictional interactions control the composite action. For example, Figure 3 shows the relation between the shear resistance and slip as assessed by Daniels and Crisinel (1993). The experimental results overestimate chemical bond due to the absence of imposed curvature as well as suggest a nonlinear shear transfer distribution over length (DANIELS; CRISINEL, 1993).

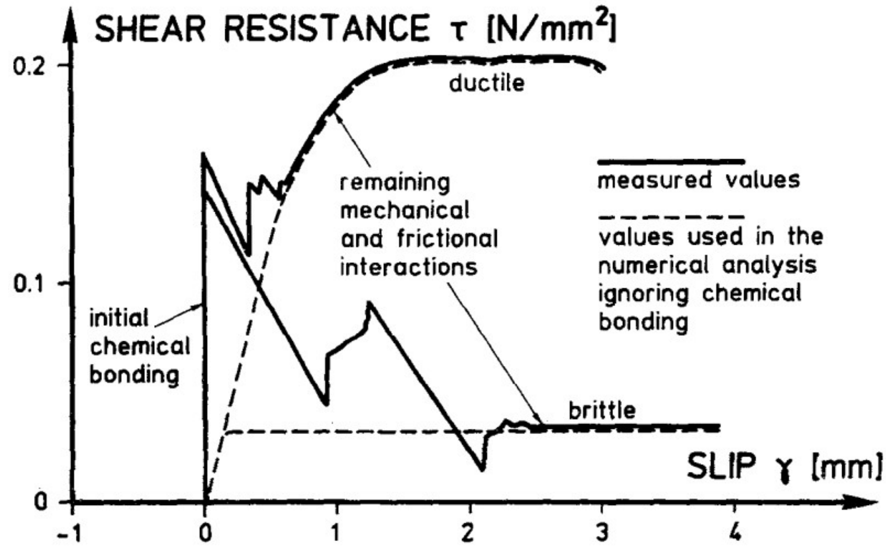


**Figure 3.** Shear resistance versus slip in composite slabs.
Source: Daniels and Crisinel (1993).

Actually, the steel sheeting and its properties influence the interlocking mechanism. The EN 1994-1-1 (CEN, 2004) reports the end anchorage provided by weld stud bolts, according to Figure 4 (slab number 3, only in combination with frictional or mechanical interlocking), and end anchorage by deformation of the ribs at the end of sheeting combined with frictional interlocking, according to Figure 4 (slab number 4), as optional shear transfer mechanisms. Still, other means can be set, but they are not within the scope of the standard.

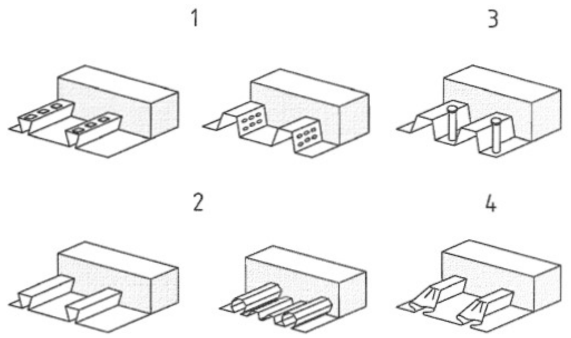


**Figure 4.** Means of interlocking in composite decks.
Source: EN 1994-1-1 (CEN, 2004).

Both EN 1994-1-1 (CEN, 2004) and NBR 8800 (ABNT, 2008) outline equations for the design of composite slabs considering bending, vertical and longitudinal shear resistances as well as deflections in the serviceability limit-state. However, since this research looks forward to assessing the interaction between steel and concrete into a slab system for the simply supported condition, designs for vertical shear and hogging bending are not detailed here.

### 2.1.1 Sagging moment resistance ($M_{pl,Rd}$)

In the plurality of design cases, the plastic neutral axis (PNA) lies on concrete above steel shuttering (GROSSI; SANTOS; MALITE, 2020), according to Figure 5. Denoting by $t_c$ the concrete layer thickness and by $a$ the PNA depth, then the plastic resistance must be calculated according to Eq. (1) – Eq. (3).

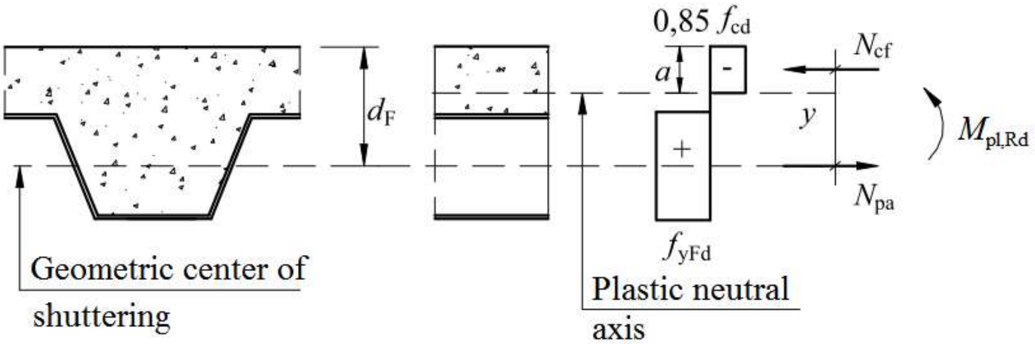


**Figure 5.** Stresses in cross-section due to bending.
Source: adapted from NBR 8800 (ABNT, 2008).

$$N_{pa} = A_{F,ef} f_{yFd} \qquad \text{Eq. (1)}$$

$$a = \frac{N_{pa}}{0.85 f_{cd} b} \qquad \text{Eq. (2)}$$

$$M_{pl,Rd} = N_{pa}(d_F - 0.5a) \qquad \text{Eq. (3)}$$

Where $N_{pa}$ is the tensile force on shuttering, $A_{F,ef}$ is the shuttering effective cross-sectional area associated to unitary length of $1000\ mm$, $f_{yFd}$ is the shuttering design yield resistance, $f_{cd}$ is the concrete compressive design strength, $b$ is the unitary slab length taken as $1000\ mm$ and $d_F$ is the distance from the slab top to shuttering geometric center.

### 2.1.2 Longitudinal shear resistance $\left(V_{l,Rd}\right)$

The loss of composite action on account of shear can be assessed through the m-k method, applied to slabs with mechanical or frictional interlocking. In the case, the maximum design shear force cannot exceed the longitudinal shear resistance $V_{l,Rd}$, calculated according to Eq. (4).

$$V_{l,Rd} = \frac{bd_F}{\gamma_{sl}}\left(m\frac{A_{F,ef}}{bL_s} + k\right) \qquad \text{Eq. (4)}$$

Where $m$ and $k$ are the empirical constants determined according to section 2.3 and $L_s$ is the shear span, taken as: (a) $L/4$ in case of simply supported slabs ($L$ is the slab span) for uniformly distributed loads; (b) the distance between the support and a concentrated load in case of two symmetrically applied loads; or (c) the quotient between maximum bending moment and maximum reaction for other load conditions.

## 2.2 COMPOSITE SLABS WITH ADDITIONAL REBAR

The Brazilian National design code NBR 8800 (ABNT, 2008) state that, in case of additional rebar in the composite slab, Eq. (1) – Eq. (3) must be adapted accordingly to take into account the extra strength provided by steel reinforcement bars. Nevertheless, the standard supplies no method to guide if any consideration should be done.

In this context, Grossi, Santos and Malite (2020) proposed an analytical model to assess the longitudinal shear capacity of composite slabs with additional rebar (Figure 6a) by extending the m-k method, assuming the additional reinforcement area as third variable in addition to the $m$ and $k$ arisen from tests with no steel bars.

On account of absence of researches on this field, the performance of composite slabs with additional rebar was little investigated until Grossi (2016). Hence, 11 samples were tested under four-point bending test as per the EN 1994-1-1 (CEN, 2004), showing that insertion of rebar increased the longitudinal shear ductility and the load carrying capacity linearly with reinforcement area denoted by $A_s$ (Figure 6b), allowing for better use of plastic strength of materials.

It's important to state that the m-k method is considered here because it applies to ductile or brittle shear behaviors, while the partial shear connection (PSC) one can exclusively be addressed to slabs with ductile shear behavior.

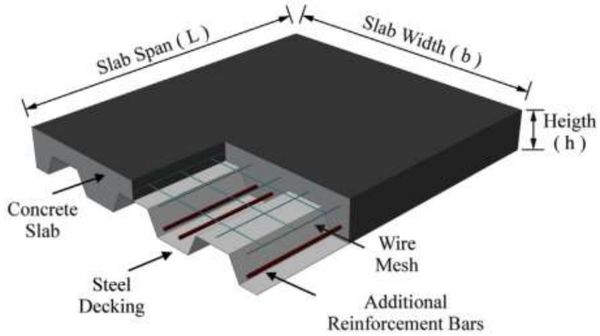


(a)

Source: Grossi, Santos and Malite (2020)

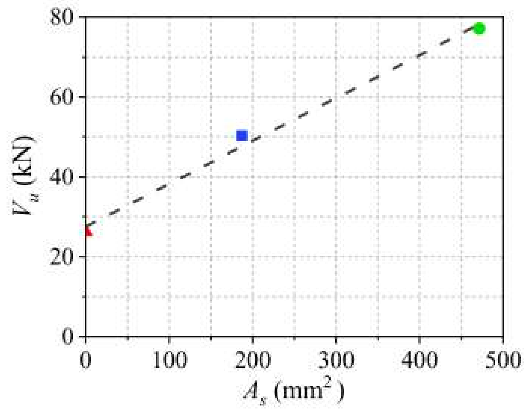


(b)

Source: Grossi (2016)

**Figure 6.** Composite slabs with additional rebar: (a) scheme; and (b) longitudinal shear behavior.

### 2.2.1 Sagging moment resistance $(M_{pl,Rd})$

According to Grossi, Santos and Malite (2020), the flexural capacity of composite slabs with additional rebar can be derived from rigid plastic analysis assuming yielding of steel elements and concrete crushing on the top. Same assumption was made by Stark and Brekelmans (1996) when developing equations to the plastic design of continuous composite slabs.

The PNA can be located in the concrete slab, between the upper face of steel deck and the center of the additional rebar or between the center of the additional rebar and the lower flange of the steel decking. However, the last configuration requires high rates of steel reinforcements and a very thin concrete slab, which is impossible from the practical point of view (GROSSI, 2016). Moreover, in most of cases the PNA relies on concrete, next to top (Figure 7). As such, only this formulation is presented here, according to Eq. (5) to Eq. (9).

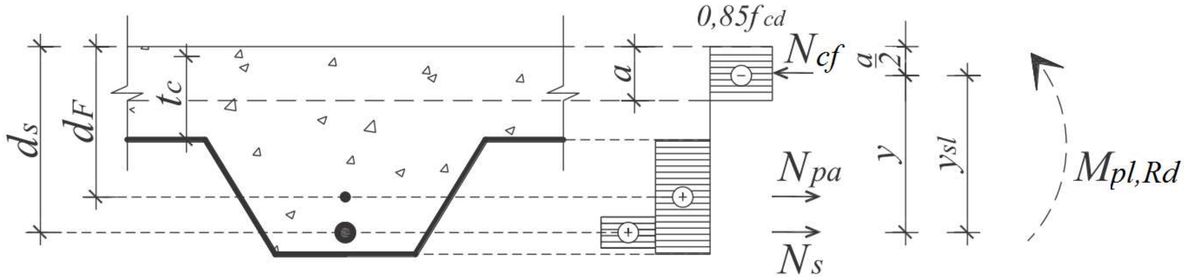


**Figure 7.** Stresses in cross-section with additional rebar due to bending.
Source: Grossi, Santos and Malite (2020).

$$N_{pa} = A_{F,ef} f_{yFd} \quad \text{Eq. (5)}$$

$$N_s = A_s f_{ysd} \quad \text{Eq. (6)}$$

$$N_{cf} = 0.85 f_{cd} ba \quad a \leq t_c \quad \text{Eq. (7)}$$

$$a = \frac{N_{pa} + N_s}{0.85 f_{cd} b} \quad \text{Eq. (8)}$$

$$M_{pl,Rd} = N_{pa}\left(d_F - \frac{a}{2}\right) + N_s\left(d_s - \frac{a}{2}\right) \quad \text{Eq. (9)}$$

Where $A_s$ is the additional rebar area, $f_{ysd}$ is the reinforcement design yield resistance, $N_s$ is the tensile force in additional rebar and $d_s$ is the distance from concrete upper surface and the geometric center of additional rebar.

### 2.2.2 Longitudinal shear resistance $(V_{l,Rd})$

The m–k method presented by the EN 1994-1-1 (CEN, 2004) is adapted from Porter and Ekberg (1976), but it does not take into account contribution from additional rebar to the shear resistance. The analytical model proposed by Grossi, Santos and Malite (2020) assumes that yield strength is reached by all reinforcement bars, which actually occurs to rates below 1.4% between steel area and the concrete area above the upper flange of steel decking $(b \times t_c)$. This condition is equivalent to $a/d_F \leq 0.5$, where $a$ is the PNA depth and $d_F$ is the distance from concrete top to center of gravity of steel shuttering. Equating the moment equilibrium in the shear span, as depicted Figure 8, it leads to Eq. (11).

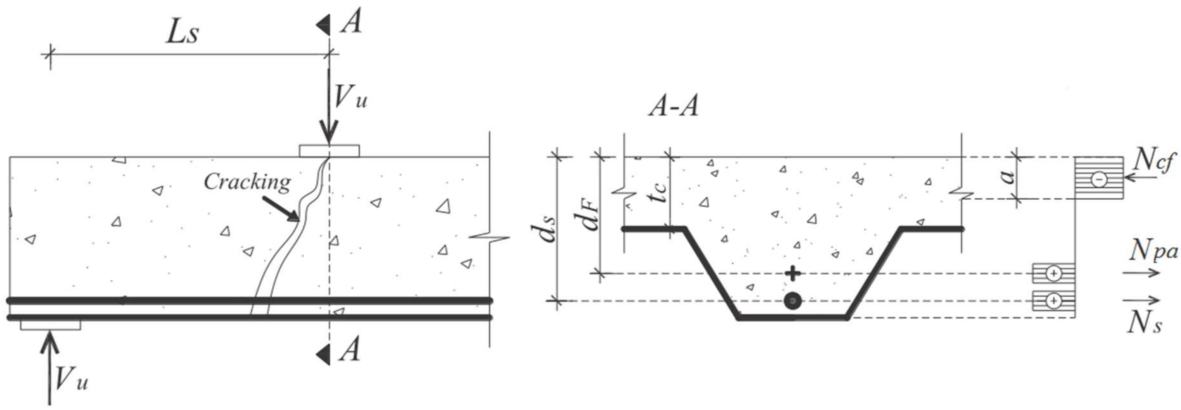


**Figure 8.** Free body diagram exhibiting internal forces on section A-A.
Source: Grossi, Santos and Malite (2020).

$$V_u L_s - N_{pa}\left(d_F - \frac{a}{2}\right) - N_s\left(d_s - \frac{a}{2}\right) = 0 \quad \text{Eq. (10)}$$

$$V_u L_s = N_{pa}\left(d_F - \frac{a}{2}\right) + N_s\left(d_s - \frac{a}{2}\right) \quad \text{Eq. (11)}$$

However, the longitudinal shear failure commonly occurs with the PNA close to the upper concrete surface. It means that, when reinforcement rate is under 1.0%, $a/2$ is small, hence $a/2 \ll d_F$ and $a/2 \ll d_s$. Therefore, $d_F - a/2 \cong d_F$ and $d_s - a/2 \cong d_s$, being Eq. (11) simplified to Eq. (12). Additionally, the tensile force on steel decking $N_{pa}$ is limited to friction in the supports $(k_1)$ and shear transfer capacity on the interface between steel and concrete $(k_2)$, which gives rise to the standard constants $m = k_1/A_{F,ef}$ and $k = k_2$. As such, the longitudinal shear capacity of composite slabs with additional rebar may be calculated according to Eq. (18).

$$V_u L_s = N_{pa} d_F + N_s d_s \quad \text{Eq. (12)}$$

$$V_u L_s = (k_1 + k_2 b L_s) d_F + N_s d_s \quad \text{Eq. (13)}$$

$$V_u L_s = k_1 d_F + k_2 b L_s d_F + N_s d_s \quad \text{Eq. (14)}$$

$$V_u = \frac{k_1 A_{F,ef} b d_F}{A_{F,ef} b L_s} + \frac{k_2 b L_s d_F}{L_s} + \frac{N_s d_s}{L_s} \quad \text{Eq. (15)}$$

$$V_u = \frac{k_1 A_{F,ef} b d_F}{A_{F,ef} b L_s} + \frac{k_2 b L_s d_F}{L_s} + \frac{N_s b d_s d_F}{b L_s d_F} \quad \text{Eq. (16)}$$

$$\frac{V_u}{b d_F} = \frac{k_1 A_{F,ef}}{A_{F,ef} b L_s} + k_2 + \frac{N_s d_s}{b L_s d_F} \quad \text{Eq. (17)}$$

$$V_{l,Rd} = \frac{bd_F}{\gamma_{sl}}\left[m\frac{A_{F,ef}}{bL_s} + k + \frac{N_s d_s}{bd_F L_s}\right] \quad \text{Eq. (18)}$$

Where $V_u$ and $V_{l,Rd}$ are the nominal and design shear resistance, respectively.

## 2.3 TESTING PROCEDURE

According to the Annex B from the EN 1994-1-1 (CEN, 2004), the test seeks to determine the empirical constants $m$ and $k$ or the longitudinal shear strength $\tau_{u,Rd}$ used in the PSC method. Variables to be investigated include steel thickness, grade, density and coating, slab depth and the shear span.

The test must be performed in the simply supported condition and equal loads must be introduced in two lines distant $L/4$ from supports (Figure 9) by two spreader steel beams, where $L$ is the slab span. The symbol "1" indicates a neoprene pad or similar placed under the sections to normalize the contact surface (dimension: $b \times m, m \leq 100\ mm$). In addition, the distance between the centerline of supports and the end of slab (overhang) must not exceed $100\ mm$.

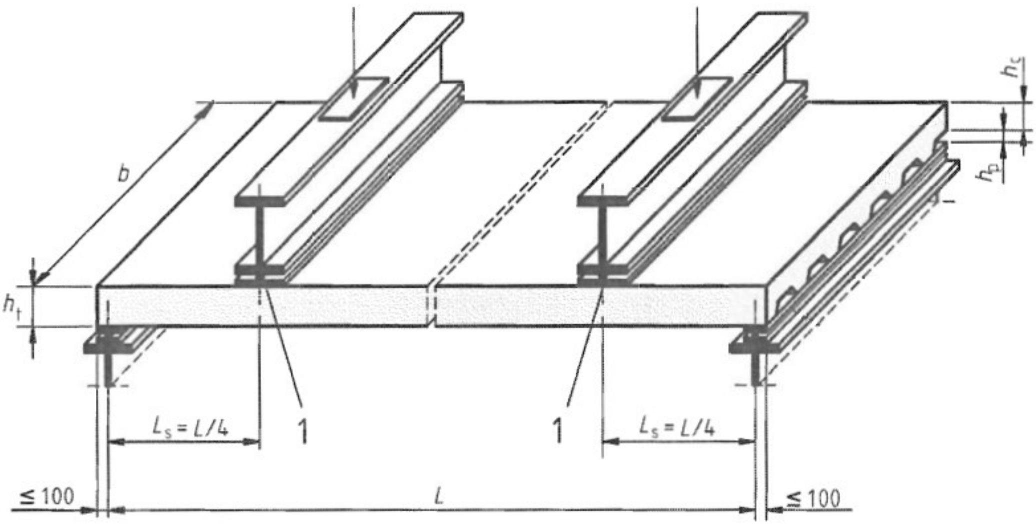


**Figure 9.** Four-point bending test arrangement.
Source: EN 1994-1-1 (CEN, 2004).

For each investigated variable, two groups of three tests must be carried out. In the first case, the shear span must be as long as possible and then, in the last case, it should be as short as possible. In both cases, samples are expected to failure under longitudinal shear.

### 2.3.1 Sample preparation

The slabs should be cast in the fully supported condition, which is the most unfavorable case for the shear failure since no stress is acting on shear interface in this situation, and shuttering must be employed as it's fabricated. Moreover, mesh reinforcements might be included in slab samples in de compression zone to prevent cracking due to temperature as well as to avoid problems during transportation.

Furthermore, all samples must be fabricated with same concrete mix, granting same proportion between cement, sand, gravel and water. The tensile and ultimate strengths of formwork also must also be determined. Finally, each group of slabs should be tested within 2 days as stated in the EN 1994-1-1 (CEN, 2004).

### 2.3.2 Experiment procedure

The first specimen from each group must be subjected to an increasing progressive static load until failure in one hour at least. Hence, the level of cyclic steps to next tests can be easily defined. The collapse load ($W_t$) is the sum of imposed load at failure and dead load of specimen and spreader beams. Then, when two last prototypes are subjected to cyclic load, the lower value should be not greater than $0,2W_t$ and the upper one must be not less than $0,6W_t$ according to the EN 1994-1-1 (CEN, 2004).

### 2.3.3 Calculation of $m$ and $k$ constants

According to section 9.7.3 from the EN 1994-1-1 (CEN, 2004), the shear behavior is ductile if failure load exceeds the load that causes an end-slip of 0,1 mm by 10% or more. Nevertheless, if collapse occurs with midspan deflection surpassing $L/50$, than the failure load must be assumed as the one at $L/50$. Otherwise, it may be considered as brittle.

In case of ductile behavior, the shear force at failure is 50% of failure load $W_t$ ($V_t = 0.5W_t$). On the other case, $V_t$ must be reduced by 0.8 and, thus, $V_t = 0.4W_t$ (Figure 10).

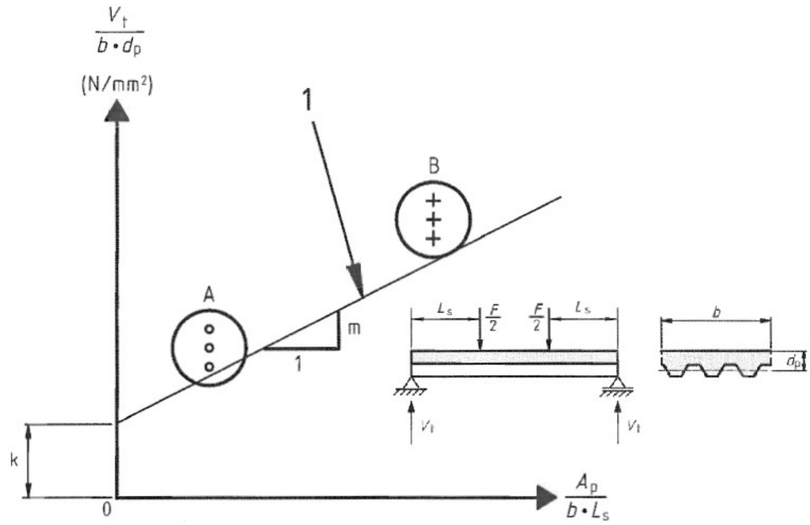


**Figure 10.** Analysis of test results.
Source: EN 1994-1-1 (CEN, 2004).

Finally, the $m$ and $k$ constants are assessed by linear adjustment of plotted points in diagram in Figure 10, where A corresponds to group with largest shear span and B to group with smallest one.

### 2.3.4 Practical guidelines according to specialized literature

Whereas the EN 1994-1-1 (CEN, 2004) presents clear recommendation on the four-point bending test to assess the load capacity under longitudinal shear behavior of composite slabs, it's important to investigate in the literature how procedures are actually carried out to ensure reliability of test results.

Meanwhile, Soltanalipour *et al.* (2020) investigated the accuracy of standardized testing procedures in the mechanical response of composite slabs by changing the load arrangement from 4-point to uniformly distributed, as specified in design codes. After experimental and finite element analyses for long and short spans, they concluded that 4-point bending showed higher shear resistance than the uniform load test for the analyzed open-rib shuttering (Figure 11). Therefore, it influenced more the composite slab resistance rather than any other parameter.

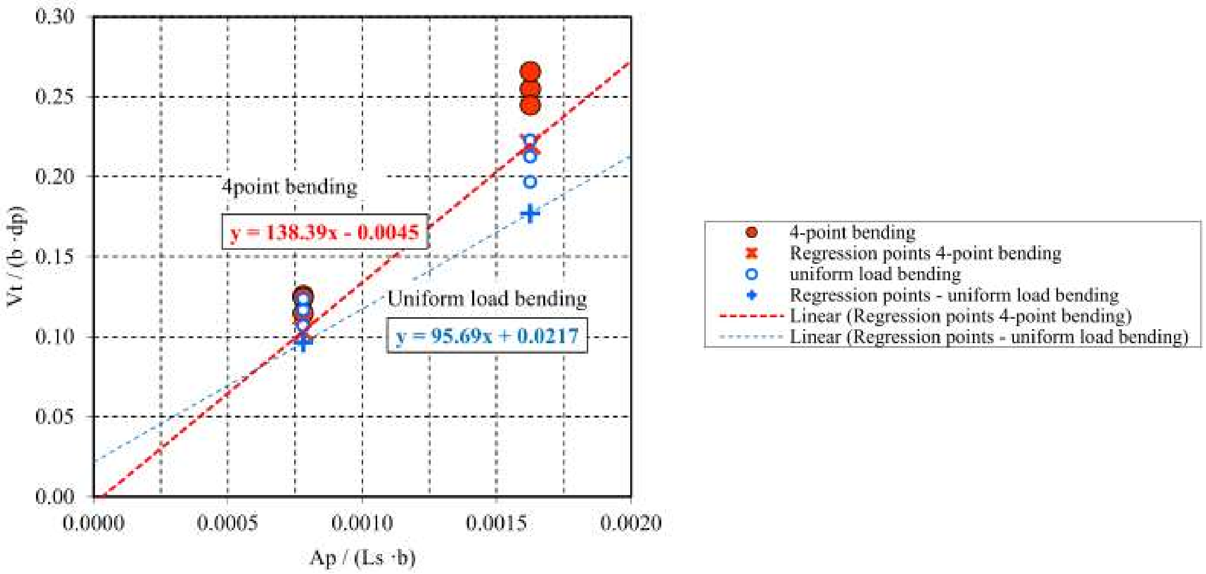


**Figure 11.** Comparison between 4-point and uniform bending tests.
Source: Soltanalipour *et al*. (2020).

This happens because alternative load arrangements not prescribed in the EN 1994-1-1 (CEN, 2004), such as 4, 6, 10 and 18-point bending or uniform by airbags, vacuum chamber or overlaid weights, give rise to different interaction forces between concrete and sheeting. Hence, distinct cracking patterns are observed while various resistances to longitudinal shear can be obtained to same slab design as numerically determined by Veljković (1998) and Holomek and Bajer (2012). Here, embossments play an important role by providing the necessary re-entrant angle to grant concrete's vertical retention to grant the composite behavior (SOLTANALIPOUR *et al*., 2020)

Moreover, full priority should be dedicated to the definition of spans and shear spans for experimental campaign, which can be challenging when dealing with innovative systems never tested before. The EN 1994-1-1 (CEN, 2004) requires two groups with different shear spans (A and B in Figure 10), but it does not provide further information regarding alternative testing arrangements, for example, such as fixed span with different shear spans. Depending on laboratorial capacity or sample fabrication conditions, it can be a promising strategy, which is already adopted by several researches according to Table 1.

**Table 1.** Typical shear span ratios adopted at the 4-point bending test (continues).

| **Researcher** | **Deck's height** $h\ [mm]$ | **Span** $L\ [mm]$ | **Shear span** $L_s\ [mm]$ | $\frac{L_s}{L}$ |
|---|---|---|---|---|
| Ferraz (1999) | 75 | 1800 | 300 | 1/6 |
| | | 1800 | 450 | 1/4 |
| | | 1800 | 600 | 1/3 |
| | | 3600 | 900 | 1/4 |
| | | 3600 | 1500 | 1/2.4 |
| Souza-Neto (2001) | 75 | 1800 | 300 | 1/6 |
| | | 1800 | 450 | 1/4 |
| | | 1800 | 600 | 1/3 |
| | | 3600 | 900 | 1/4 |
| | | 3600 | 1500 | 1/2.4 |
| Costa (2009) | 60 | 2500 | 450 | 1/5.6 |
| | | 2500 | 800 | 1/3.125 |
| Gholamhoseini *et al.* (2014) | 40<br>55<br>57<br>70 | 3100 | 517 | 1/6 |
| | | 3100 | 775 | 1/4 |
| | | 3400 | 567 | 1/6 |
| | | 3400 | 850 | 1/4 |
| Sieg (2015) | 55 | 1800 | 450 | 1/4 |
| | | 3600 | 900 | 1/4 |
| Hossain *et al.* (2016) | 51<br>76 | 1800 | 300 | 1/6 |
| | | 1800 | 380 | 1/4.7 |
| | | 1800 | 450 | 1/4 |
| | | 1800 | 530 | 1/3.4 |
| | | 1800 | 600 | 1/3 |

**Table 1.** Typical shear span ratios adopted at the 4-point bending test (conclusion).

| | | | | |
|---|---|---|---|---|
| Waldmann, May and Thapa (2017) | 51<br>56 | 4000 | 600 | 1/6.7 |
| | | 4000 | 1000 | 1/4 |
| Arrayago *et al.* (2018) | 58 | 2500 | 625 | 1/4 |
| | | 4300 | 1075 | 1/4 |

Finally, crack inducers should be place across complete slab width under concentrated loads to better define the shear span, to eliminate tensile strength at concrete element as well as to ease crack propagation as recommended by the EN 1994-1-1 (CEN, 2004). However, their application during fabrication of prototypes was suppressed in several researches on account of aim of study to reproduce the slab behavior as they are cast at construction site, such as Abas *et al.*, (2013), Costa (2009), Ferraz (1999), Gholamhoseini *et al.* (2014), Grossi, Santos and Malite (2020), Hossain *et al.* (2016), Sieg (2015), Souza-Neto (2001) and Zhang *et al.* (2020).

## 2.4 LOAD-DISPLACEMENT RESPONSE

The deflections of composite slabs are not properly addressed in many design codes such as the NBR 8800 (ABNT, 2008), stating that maximum displacement in serviceability must not exceed $L/350$, where $L$ is the span length measured in parallel to ribs, not disclosing the procedure for such calculation. Moreover, Costa *et al.* (2021) complement that other codes as the CSSBI S3 (CANADIAN SHEET STEEL BUILDING INSTITUTE, 2017) suggest the average moment of inertia of both uncracked and cracked sections to assess the effective flexural stiffness of the composite section. Although, it leads to untrustworthy results and it do not reproduce the behavior of composite slabs.

Indeed, the load-displacement response of composite slabs is complex because of early concrete cracking, recognized as the main source of nonlinearity in first load stages. Then, inelastic creep and shrinkage increment deformation with time and, in case of continuous slabs, they affect the distribution of bending moment according to Costa *et al.* (2021) and Gholamhoseini, Gilbert and Bradford (2016).

Nevertheless, there are models calibrated with tests in the literature to calculate the response of composite slabs under static load (COSTA et al., 2021). Different from composite beams, where long-term effects are taken into account by reducing the modular ratio to $1/3$ as per the NBR 8800 (ABNT, 2008), the vertical deflections of composite slabs are usually calculated at short-term after homogenization of the steel-concrete cross-section.

For instance, Figure 12 represents a generic section of a composite slab. The calculation of both uncracked and cracked moments of inertia is based on elastic theory. In the first case, the concrete in tension contributes to stiffness of slab and, otherwise, concrete areas below the neutral axis are neglected.

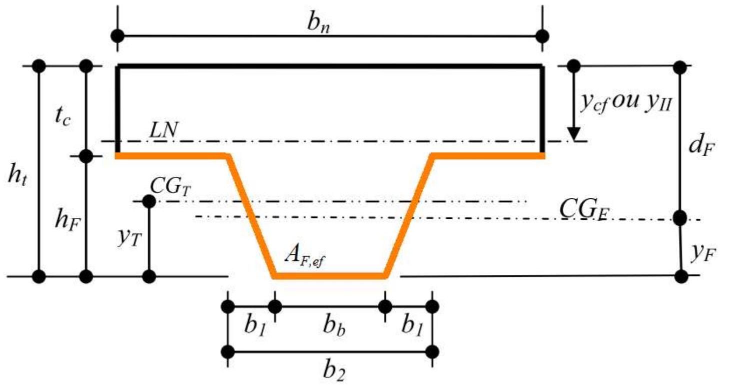


**Figure 12.** Generic cross-section of a steel-concrete composite slab.
Source: COSTA *et al*. (2021).

The inertia of uncracked section ($I_{cf}$) must be calculated according to Eq. (19) to Eq. (24), where $\alpha_E$ is the modular ratio, $E_a$ is the steel modulus of elasticity, $E_{cs}$ is the secant modulus of elasticity of concrete, $A_T$ is the web's trapezoidal area, $y_T$ is the distance from trapezoidal area centroid to the bottom shuttering, $I_T$ is the moment of inertia of trapezoidal area, $y_{cf}$ is the neutral axis depth of uncracked section and $I_F$ is the steel deck moment of inertia. Remaining variables are defined in Figure 12.

$$\alpha_E = \frac{E_a}{E_{cs}} \quad \text{Eq. (19)}$$

$$A_T = \frac{b_2 + b_b}{2} h_F \quad \text{Eq. (20)}$$

$$y_T = \frac{h_F(3b_b + 4b_1)}{6(b_b + b_1)} \quad \text{Eq. (21)}$$

$$I_T = \frac{b_b h_F^3}{12} + b_b h_F \left(y_T - \frac{h_F}{2}\right)^2 + \frac{b_1 h_F^3}{18} + b_1 h_F \left(h_F - y_T - \frac{h_F}{3}\right)^2 \quad \text{Eq. (22)}$$

$$y_{cf}=\frac{\frac{b_n t_c^2}{2}+A_T(h_t-y_T)+\alpha_E A_{F,ef} d_F}{b_n t_c+A_T+\alpha_E A_{F,ef}} \quad \text{Eq. (23)}$$

$$I_{cf}=\frac{b_n t_c^3}{12}+b_n t_c\left(y_{cf}-\frac{t_c}{2}\right)^2+I_T+A_T\left(h_t-y_{cf}-y_T\right)^2+\alpha_E I_F+\alpha_E A_{F,ef}\left(d_F-y_{cf}\right)^2 \quad \text{Eq. (24)}$$

Finally, the inertia of cracked section $(I_{II})$ should be obtained according to Eq. (25) to Eq. (27), where $y_{II}$ is the neutral axis depth of cracked section.

$$\rho=\frac{A_{F,ef}}{b_n d_F} \quad \text{Eq. (25)}$$

$$y_{II}=\begin{cases}\left(\sqrt{\rho^2\alpha_E^2+2\rho\alpha_E}-\rho\alpha_E\right)d_F & y_{II}<t_c\\ t_c & y_{II}\geq t_c\end{cases} \quad \text{Eq. (26)}$$

$$I_{II}=\frac{b_n y_{II}^3}{3}+\alpha_E I_F+\alpha_E A_{F,ef}(d_F-y_{II})^2 \quad \text{Eq. (27)}$$

According to the EN 1994-1-1 (CEN, 2004), deflections should be calculated using elastic analysis, neglecting the effects of shrinkage. In this sense, numerous models to assess the effective moment of inertia $\left(I_{eff}\right)$ of composite slabs are available in the literature, which are summarized in Table 2, i.e., Eq. (28) to Eq. (34).

**Table 2.** Assessment of the effective moment of inertia in composite slabs.

| **Model** | **Source** | **Analytical expression for $I_{eff}$** | **Comments** |
|---|---|---|---|
| Eq. (28)<br>M1 | CSSBI S3:2017<br>Johnson (2004) | $I_{eff} = \frac{I_{cf} + I_{II}}{2}$ | Predicted stiffness does not represent measured displacement values. |
| Eq. (29)<br>M2 | Tenhovuori, Karkkainen, Kanerva (1996) | $I_{eff} = I_{cf}\left(\frac{M_r}{M_a}\right)^3 + I_{II}\left[1 - \left(\frac{M_r}{M_a}\right)^3\right] \leq I_{cf}$ | It's an extension of equations from Branson (1963) to composite slabs. |
| Eq. (30)<br>M3 | Souza-Neto (2001) | $I_{eff} = I_{cf}\left(\frac{M_r}{M_a}\right)^3 + \frac{I_{II}}{20}\left[1 - \left(\frac{M_r}{M_a}\right)^3\right] \leq I_{cf}$ | It adjusts Branson's (1963) equation to reduce the contribution of cracked moment of inertia. |
| Eq. (31)<br>M4 | EN 1994-1-1 (CEN, 2004) | $M_a < M_r \therefore I_{eff} = I_{cf}$<br>$M_a \geq M_r \therefore$<br>$I_{eff} = I_{cf}\left(\frac{M_r}{M_a}\right)^2 + I_{II}\left[1 - \left(\frac{M_r}{M_a}\right)^2\right] \leq I_{cf}$ | It suggests the use of equations addressed to concrete elements according to the EN1992-1-1 (CEN, 2004) to calculate the effective moment of inertia of composite sections. |
| Eq. (32)<br>M5 | Costa *et al.* (2021) | $I_{eff} = I_{cf}\left(\frac{M_r}{M_a}\right)^2 \leq I_{cf}$ | It ignores the contribution arisen from cracked section when $M_a \geq M_r$. |
| Eq. (33)<br>M6 | Costa *et al.* (2021) | $I_{eff} = I_{cf}\left(\frac{M_r}{M_a}\right)^2 + \frac{I_{II}}{10}\left[1 - \left(\frac{M_r}{M_a}\right)^2\right] \leq I_{cf}\ or\ I_{II}$ | If the slab behavior is ductile, than $I_{eff} = I_{cf}$ when $M_a < M_r$. Otherwise, $I_{eff} = I_{II}$. |
| Eq. (34)<br>M7 | Costa *et al.* (2021) | $I_{eff} = I_{II}\left(\frac{M_r}{M_a}\right)^2 \leq \frac{I_{cf} + I_{II}}{2}$ | The effective moment of inertia is calculated based exclusively on the cracked section. |

$M_r$ is the cracking moment of slab, calculated according to Eq. (36), and $M_a$ is the moment acting on serviceability due to external loads. In addition, $f_{ck}$ is the characteristic compressive strength of concrete, used in MPa in Eq. (35), $f_{ct}$ is the direct tensile strength of concrete, $y_t$ is the distance between geometric center of section and extreme fiber under tension and $\alpha_1$ is a coefficient that associates the bending strength to the direct tensile strength taken as 1.2 for T-shaped sections.

$$f_{ct} = 0.3 f_{ck}^{\frac{2}{3}} \qquad \text{Eq. (35)}$$

$$M_r = \frac{\alpha_1 f_{ct} I_{cf}}{y_t} \qquad \text{Eq. (36)}$$

## 2.5 NEW COMPOSITE SYSTEMS FOR SLABS

Motivated by the benefits arisen from composite construction, several researches have been conducted worldwide in order to develop high performance flooring systems. In Brazil, Takey (2001) developed an efficient composite ribbed slab using CFS profiles and light filling material, eliminating shuttering and propping during construction (Figure 13-a). Four-point bending tests were carried out in order to assess the shear resistance in the interface between steel and concrete and the load capacity. The results were satisfactory when compared to the behavior of precast RC lattice girder slabs. Beltrão (2003) and Vieira (2003) studied similar systems through experimental analyses as well.

Then, Vianna (2005) proposed an optimized CFS profile, with stiffeners in the top flange (Figure 13-b). Pull-out test were carried out to determine the shear resistance and, afterwards, four-point bending tests were performed to evaluate the ultimate failure load and deflections, also investigating the failure modes in the composite slabs. Results were also satisfactory.

Sieg (2015) examined the mechanical behavior of a composite deck using an alternative profile, being the ultimate strength determined before and after concrete curing. Fourteen four-point bending tests were conducted on the composite deck and, then, the design equations for the "m-k" method were obtained considering the ultimate limit state of longitudinal shear.

Grossi (2016) evaluated the influence of additional rebar in trapezoidal decks as an alternative to the increase in the deck's gauge to span longer. Nevertheless, being this an unusual system available in the market, there's a gap in standardizes formulations to this case. He conducted several full scale tests on steel deck samples, with and without additional rebar, concluding that higher ductility and higher strength were observed in the new configuration. Finally, he presented an alternative method to design composite slabs with additional rebar based on the *m* and *k* constants from standard tests.

More recently, Lauwens *et al*. (2018) investigated the influence of steel composition in the shear behavior by comparing ferritic stainless steel to carbon steel composite slabs. After assessing results from experimental campaign, they concluded that both behaviors are equivalent in terms of load capacity.

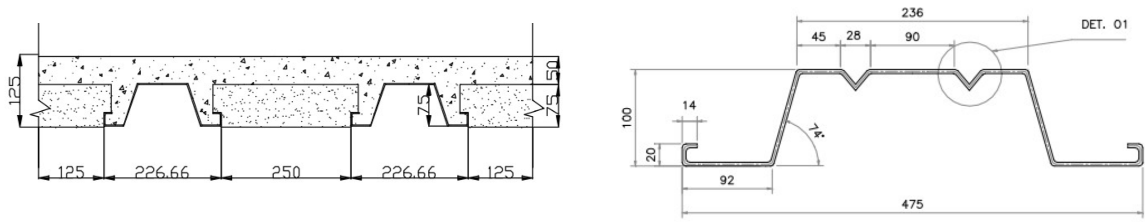


(a) (b)

**Figure 13.** Section of composite slabs tested by (a) Takey (2001) and (b) Vianna (2005).

The closest system to the one analyzed in this research was released by Tuper (2018), composed by a galvanized CFS section in minor bending, light filling material and concrete. However, no rebar truss is place above steel profiles, which differs this system from conventional precast concrete slabs. In most cases, ribs do not need additional rebar to resist the sagging bending moment after concrete curing due to very pronounced embossments on profile (Figure 14).

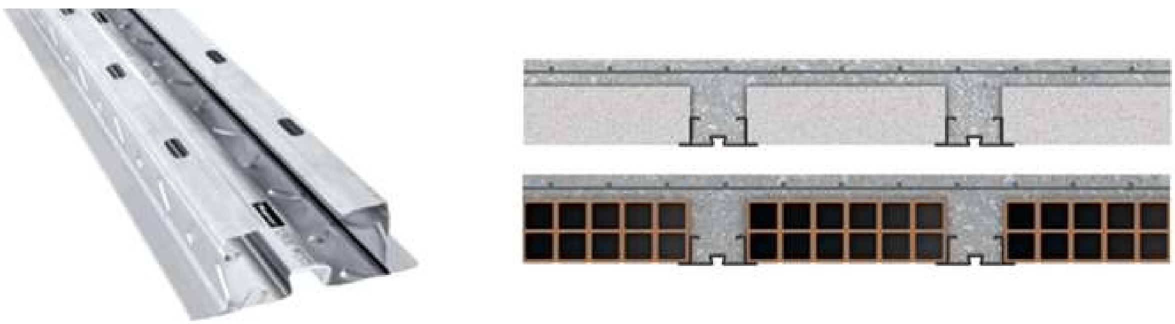

**Figure 14.** An overview of composite ribbed slab found in Brazilian market.
Source: Tuper (2018).

# 3

# MATERIALS AND METHODS

## 3.1 CHARACTERIZATION OF MATERIALS

### 3.1.1 Concrete

The concrete employed in this research was supplied by CONCREVIT, company located in Serra-ES/Brazil, for which a characteristic compressive strength, $f_{ck}$, equal to 30 MPa was requested. Because of reduced spaces between rebar trusses and cold-formed shuttering and due to difficulty in vibrating the concrete samples, self-consolidating concrete (SCC) was used. The mix design for both prototypes is presented in Table 3 – the same from Candido (2021), produced with CPIII-40 RS cement. It’s important to state that “TS2.5_16_0.33” denotes the composite rebar truss specimens while “RCS2.5_16_0.33” refers to the reinforced concrete ones. Further details on these codes are given in section 3.2.

**Table 3.** Concrete mix designs employed in the research – mass proportion.

| Test group | Cement CPIII-40 RS | Fine sand | Medium sand | Gravel 0 | w/c relation | PL additives | SP additives |
|---|---|---|---|---|---|---|---|
| TS2.5_16_0.33<br>RCS2.5_16_0.33 | 1.000 | 1.134 | 1.134 | 1.806 | 0.55 | 0.70% | 0.33% |

#### 3.1.1.1 Concrete flow assessment

Immediately after the concrete was received at the Laboratory of Structures (LEST) from the Center of Technology of Federal University of Espírito Santo (CT/UFES), its fluidity was assessed through the slump flow test (Figure 15) according to the NBR 15823-2 (ABNT, 2017a).

(a) (b)

**Figure 15.** Slump flow test: (a) preparation; and (b) result.
Source: Author.

#### 3.1.1.2 <u>Cylindrical strength</u>

Eighteen concrete cylindrical specimens for each group were prepared and identified according to the NBR 5738 (ABNT, 2016) and tested in agreement with the NBR 5739 (ABNT, 2018). As gravel 0 was employed, cylindrical specimens with $10\,cm$ of base diameter and $20\,cm$ of height were adopted. Specimens were divided in two groups of 9 as follows:

a) the first, named WC, was subjected to wet curing into a water tank saturated with $Ca(OH)_2$;
b) the second, named CC, was subjected to chemical curing (Figure 16a) with the product CURING® from Vedacit (Figure 16b), the same condition than full-scale concrete slab specimens.


(a) (b)

**Figure 16.** (a) Specimens subjected to chemical curing; (b) curing product used in the research.
Source: Author.

Then, 34 days after casting, the specimens were prepared at Laboratory of Testing in Construction Materials (LEMAC) at UFES, being faces previously adjusted (Figure 17a). Afterwards, specimens were tested at Brascontec, company located in Serra-ES/Brazil, using a $2000\,kN$ hydraulic press fabricated by Contenco model HD200T (Figure 17b).

(a) (b)

**Figure 17.** Preparation of specimen and testing.
Source: Author.

From 9 specimens in group WC and CC, the firsts 2 were subjected to failure under compression to determine their average strength ($f_{c,ef}$), the base parameter for secant modulus of elasticity test, in which the following 4 specimens were employed. Finally, the 3 last specimens were tested to assess the concrete compressive strength ($f_{c34}$), taken as the average value of 5 specimens (two firsts and three lasts).

3.1.1.3 Secant modulus of elasticity

Since the assessment of displacements in composite slabs depends on the concrete secant modulus of elasticity ($E_{cs}$), it was experimentally determined conforming to the NBR 8522 (ABNT, 2017b). Tests were carried out at Brascontec using the same equipment described in 3.1.1.2 (Figure 18a).

The procedure described in aforementioned standard recommends two samples to be tested to determine the average strength ($f_{c,ef}$) of group. Each of three specimens tested afterwards under the 8 load steps to calculate $E_{cs}$ should not deviate $\pm 20\%$ from $f_{c,ef}$ in terms of compressive strength ($f_c$). Nevertheless, since the first specimen presented $f_c/f_{c,ef} = 0.80$, the lower boundary specified by the NBR 8522 (ABNT, 2017b), an extra specimen was tested to not affect data set reliability, totalizing four instead of three.

Concrete strains are calculated based on two linear variable differential transformers (LVDT) placed 180º one from another (Figure 18b). Based on applied load, strains and cross-sectional area of specimens, stress-strain relation for employed concretes was obtained and, finally, secant modulus of elasticity was calculated at 40% of $f_c$, i.e., when $\sigma_c = 0{,}4f_c$ as adopted by Candido (2021).


(a)


(b)

**Figure 18.** (a) Secant modulus of elasticity test; (b) Specimens after test.
Source: Author.

3.1.1.4 Specific mass and weight

The specific mass of concrete was determined to support the calculation of dead-loads from slab prototypes. As such, immediately before rupture, all dry specimen from chemical curing (CC) were weighted ($m$) and measured – one height ($h$) and two diameters orthogonally assessed ($\emptyset_1, \emptyset_2$) as shown in Figure 19. Then, specific mass was calculated according to Eq. (37) and Eq. (38).

$$\emptyset_{ave} = \frac{\emptyset_1 + \emptyset_2}{2} \quad \text{Eq. (37)}$$

$$\rho_c = \frac{4m}{\pi h (\emptyset_{ave})^2} \quad \text{Eq. (38)}$$


(a) (b) (c)

**Figure 19.** Calculation of concrete specific mass: (a) mass; (b) height; and (c) diameter of specimen.
Source: Author.

Finally, concrete specific weight ($\gamma_c$) is obtained from specific mass ($\rho_c$) by multiplying it to the gravity acceleration ($g$), taken as $9.81\ m/s^2$, according to Eq. (39).

$$\gamma_c = g\rho_c = 9.81\rho_c \qquad \text{Eq. (39)}$$

### 3.1.2 Steel

Regarding steel from cold-formed shuttering, both yield and ultimate strength ($f_y$ and $f_u$, respectively) were adopted according to Candido (2021) since same batch was employed in this research. These tests were performed in the Metallurgy Laboratory from ArcelorMittal Vega (Santa Catarina, Brazil) as depicted in Figure 20. Young's modulus, on the other hand, was taken from the NBR 14762 as $200\ GPa$ (ABNT, 2010). Furthermore, since test results vary from $190\ GPa$ to $210\ GPa$, it's a common practice in the literature to employ nominal values as observed in Costa (2009), Sieg (2015), Bai *et al*. (2020), Zhang *et al*. (2020), Zhu *et al*. (2020) and Costa *et al*. (2021).

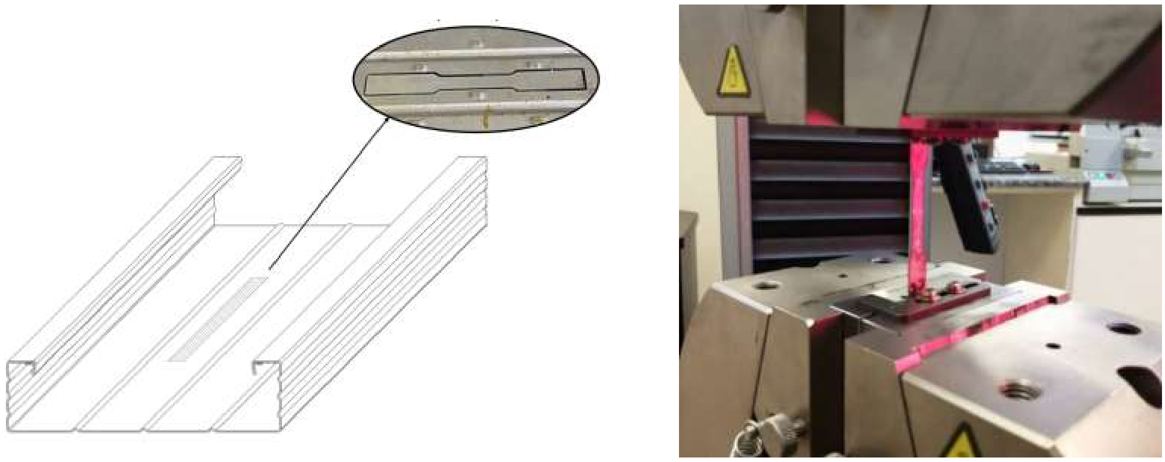

(a) (b)

**Figure 20.** Tensile test on cold-formed shuttering: (a) specimen extraction; and (b) test.
Source: Candido (2021).

Finally, nominal values of mechanical properties $f_y$ and $f_u$ of rebar trusses and wire meshes were adopted in this research. Young's modulus was adopted as nominal value of $210\ GPa$ according to NBR 6118 (ABNT, 2014).

## 3.2 EXPERIMENTAL PROGRAM

Candido (2021) was the first one to evaluate the mechanical behavior of the system investigated in this research by testing three full-scale isostatic samples with a shear span of $L/4$ and span $L$ equal to 2,5 m, observing the full interaction phenomenon in all cases. Each specimun was composed by two ribs interposed with light filling blocks made in polystyrene, two rebar trusses and two cold-formed profiles as depicted in Figure 21, which dimensions are summarized in Table 4. Note that $f_{c34}$ represents the compressive concrete strength and $E_{cs}$ the secant Young's module, both calculated with concrete samples in wet curing, which led to better results.

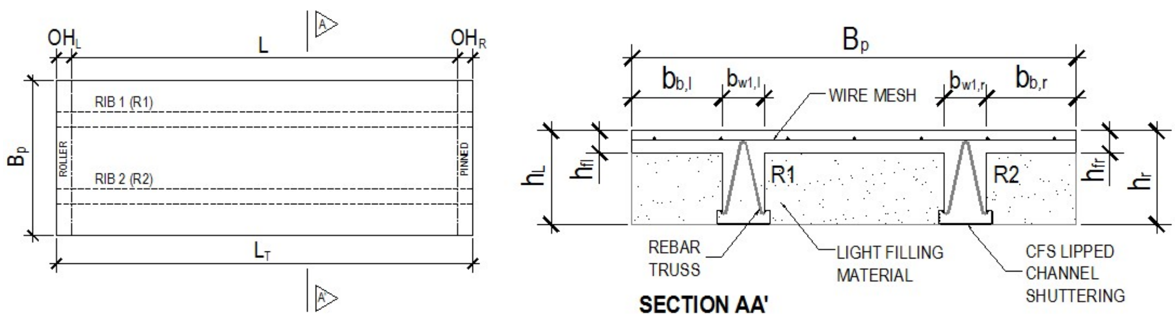


**Figure 21.** Dimension of samples and cross-sectional geometry.
Source: Author.

**Table 4.** Geometries of samples tested by Candido (2021).

| Parameter | TS2.5_16_0.25a | | TS2.5_16_0.25b | | TS2.5_16_0.25c | |
|---|---|---|---|---|---|---|
| | ***R1*** | ***R2*** | ***R1*** | ***R2*** | ***R1*** | ***R2*** |
| $L_T$ $[cm]$ | 270.00 | 270.00 | 269.90 | 270.00 | 270.00 | 269.50 |
| $OH_L$ $[cm]$ | 10.30 | 10.30 | 9.70 | 9.70 | 9.75 | 9.75 |
| $OH_R$ $[cm]$ | 9.80 | 9.80 | 9.80 | 9.80 | 10.00 | 10.00 |
| $L$ $[cm]$ | 249.90 | 249.90 | 250.20 | 250.70 | 250.00 | 250.00 |
| $B_p$ $[cm]$ | 101.65 | | 101.75 | | 101.65 | |
| $b_b$ $[cm]$ | 20.10 | 20.55 | 20.85 | 21.25 | 20.70 | 21.20 |
| $b_w$ $[cm]$ | 9.87 | 9.65 | 8.86 | 9.37 | 9.60 | 9.75 |
| $h$ $[cm]$ | 21.35 | 21.25 | 21.30 | 21.25 | 21.35 | 21.35 |
| $h_c$ $[cm]$ | 5.19 | 5.08 | 5.23 | 5.11 | 4.99 | 5.33 |
| $f_{c34}$ $[MPa]$ | 68.60 | | | | | |
| $E_{cs}$ $[GPa]$ | 35.19 | | | | | |
| Rebar truss model | TB 16L | | | | | |
| Wire mesh | Q75 = $\emptyset 3.8 \times \emptyset 3.8$, $15 \times 15$ $cm$ | | | | | |
| Shear span | 62.48 | | 62.61 | | 62.50 | |
| CFS profile surface treatment | Black | Black | Black | Black | Black | Black |

The code "TS2.5_16_0.25a", for example, denotes a Trelifácil slab (TS) cast with 2.5 m of span length (2.5) and a rebar truss 16 cm height (16), tested with shear span of $L/4 = 0.25L$ (0.25) and specimen "a". Codes "TS2.5_16_0.25b" and "TS2.5_16_0.25c" represent specimens "b" and "c" tested under the same conditions. Moreover, note that dimensions of each rib were taken separately and then employed to assess the bending resistance of each one, being the final sample strength calculated by the sum of both values.

Nevertheless, this data set is insufficient to reach a secure conclusion about the longitudinal shear behavior of slab system described here. On this account, six extra specimens were cast and tested to assess the load carrying capacity and the composite action between the cold-formed profile and the concrete rib. Previous theoretical analysis conducted by Favarato et al. (2021) for slab cross-sectional geometry as tested by Candido (2021) taking into account full-interaction suggested that vertical shear is critical for span lengths until $150.00$ $cm$. From this onwards, sagging bending moment governs the theoretical design as shown in Figure 22 and longitudinal shear is expected into this length range. It's important to state that vertical shear resistance was predicted according to Annex Q from NBR 8800 (ABNT, 2008), considering strengths provided by concrete, rebar truss diagonals and webs of cold-formed section.

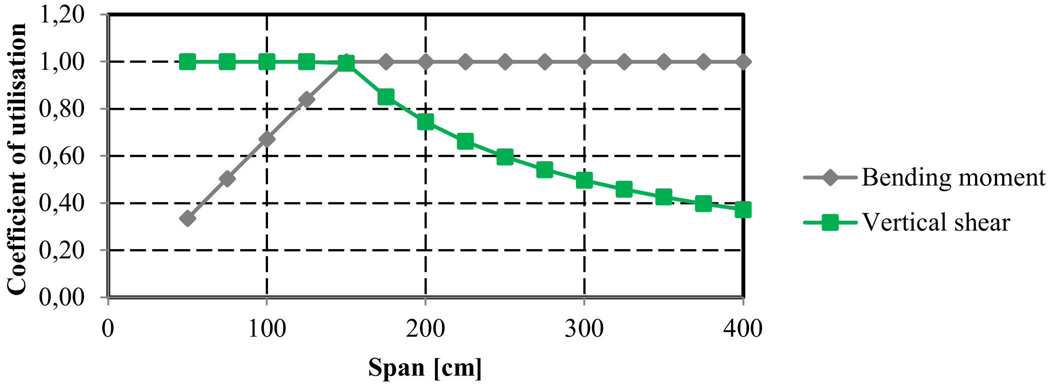


**Figure 22.** Predicted failure modes of rebar truss ribbed slab investigated in this research for different spans. Source: Favarato *et al.* (2021).

In addition, researchers summarized in Table 1 tested slab spans from 1800 mm to 4300 mm, data in accordance to Figure 22, where longitudinal shear failure is likely to happen, including 2500 mm as investigated by Candido (2021). Hence, models tested in this research are summarized in Table 5. Note that:

a) *TS2.5_16_0.33* designates the same composite sample configuration tested by Candido (2021), however with a different shear span ($L/3$ instead of $L/4$). This arrangement allows for complete assessment of shear behavior of slabs system studied here as the EN 1994-1-1 (CEN, 2004) requires, at least, two groups with three samples each calculate $m$ and $k$ constants of the steel deck. This research decided to test a different shear span where the longitudinal shear failure would be more likely to happen.

b) *RCS2.5_16_0.33* refers to reinforced concrete slab (RCS) with same span, cross-sectional geometry and shear span than TS2.5_16_0.33, although no steel shuttering as tension reinforcement is included.

**Table 5.** Sample dimension as tested in this research.

| **Parameter** | **3 x TS2.5_16_0.33** | **3 x RCS2.5_16_0.33** |
|---|---|---|
| $L_T$ $[cm]$ | 270.00 | 270.00 |
| $OH_L$ $[cm]$ | 10.00 | 10.00 |
| $OH_R$ $[cm]$ | 10.00 | 10.00 |
| $L$ $[cm]$ | 250.00 | 250.00 |
| $B_p$ $[cm]$ | 100.00 | 100.00 |
| $b_b$ $[cm]$ | 20.00 | 20.00 |
| $b_w$ $[cm]$ | 9.50 | 9.50 |
| $h$ $[cm]$ | 21.00 | 21.00 |
| $h_c$ $[cm]$ | 5.00 | 5.00 |
| Rebar truss | TB 16L | TB 16L |
| Wire mesh | Q75 = $\emptyset 3.8 \times \emptyset 3.8$, $150 \times 150$ $mm$ | Q75 = $\emptyset 3.8 \times \emptyset 3.8$, $150 \times 150$ $mm$ |
| Cold-formed area $[cm^2/rib]$ | 1.24 (1 section/rib) | 0 |
| Expected $f_{ck}$ $[MPa]$ | 30 | 30 |
| Shear span | $L/3$ | $L/3$ |
| Surface treatment | Black | Black |

Moreover, variables listed in Table 5 are illustrated in Figure 21, the geometry of CFS lipped channel section employed in such slabs is detailed in Figure 23a and rebar truss geometry is indicated in Figure 23b, where $h_0 = 25\ mm$. Finally, Table 6 and Table 7 contain, respectively, properties of the rebar truss and wire mesh employed in this research, both fabricated by ArcelorMittal.

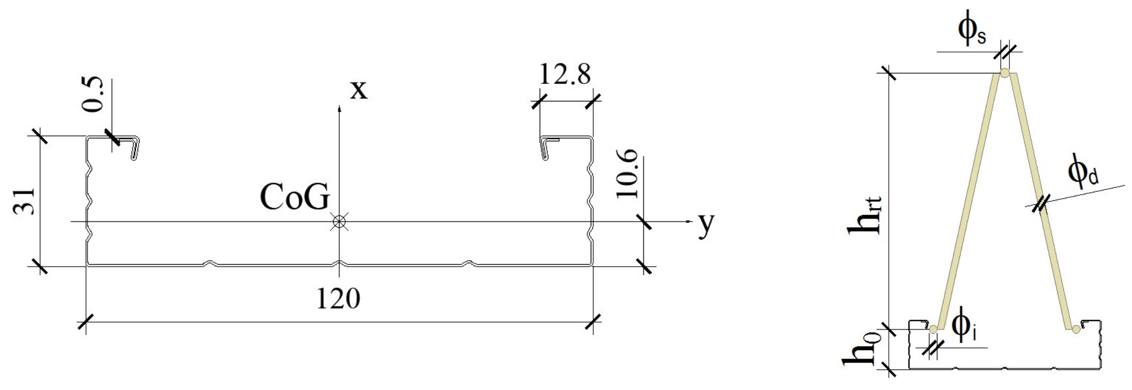


(a) (b)

**Figure 23.** (a) Cross-sectional nominal dimensions of lipped channel section; (b) General cross-section of rebar truss coupled to cold-formed profile.
Source: Author.

**Table 6.** Rebar truss properties.

| Model | $h_{rt}$ $[mm]$ | $\emptyset_s$ $[mm]$ | $\emptyset_d$ $[mm]$ | $\emptyset_i$ $[mm]$ | Dead load $[kg/m]$ |
|---|---|---|---|---|---|
| TB 8L | 80 | 6.0 | 4.2 | 4.2 | 0.735 |

Source: ARCELORMITTAL BRASIL (2017a).

**Table 7.** Wire mesh properties.

| Model | Mesh spacing $[mm \times mm]$ | $\emptyset$ $[mm \times mm]$ | $A_{s,wm}$ $[cm^2/m \times cm^2/m]$ |
|---|---|---|---|
| Q75 | 150 x 150 | 3.8 x 3.8 | 0.75 x 0.75 |

Source: ARCELORMITTAL BRASIL (2014).

## 3.3 LOAD PREVISION

The collapse load of tested samples was predicted taking into account the bending moment capacity, suppressing all resistance partial factors, based on design of steel and concrete composite or concrete structures, according to NBR 8800 (ABNT, 2008) and NBR 6118 (ABNT, 2014), respectively.

Dead loads arisen from slab sample as well as testing equipment as represented in Figure 24 must be also included in calculation of bending moment ($M_{Sk}$) acting on critical section until failure. If $G_{sp}$ is the characteristic value of slab dead load per length – including concrete, CFS profiles, rebar trusses, plastic connectors, light filling EPS blocks and wire meshes, $W_{eq}$ is dead load from neoprene, spreader beams, column (prop), load cell, plate, hinge and cylinders (props) and $F_{act}$ is the external force provided by the hydraulic actuator, then Eq. (42) allows for the estimation of needed force to lead to specimen failure when then bending moment on central critical section ($M_{Sk}$) is equal to bending resistance ($M_{Rk}$).

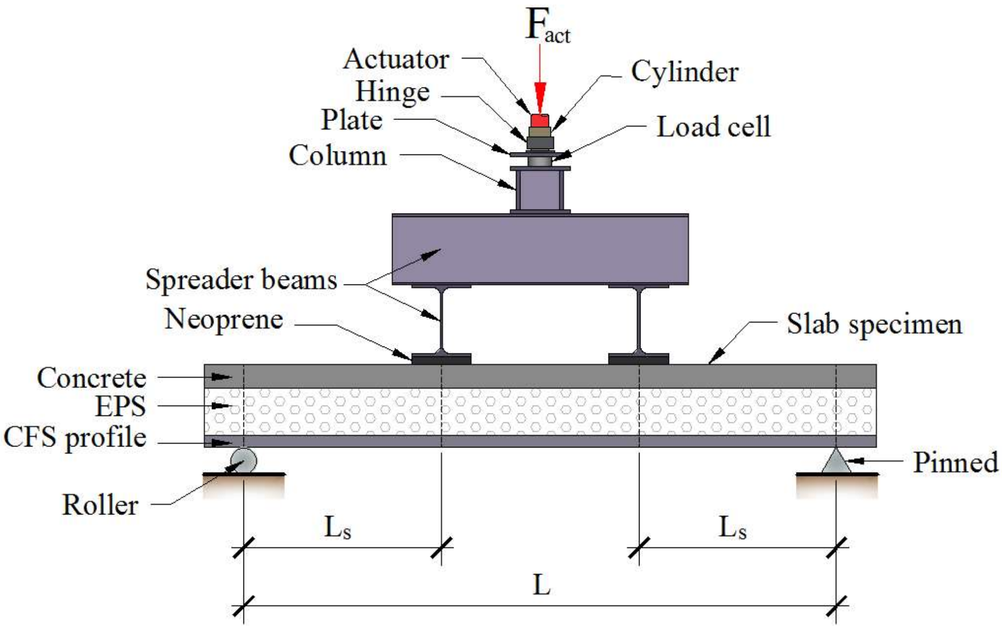


**Figure 24.** Test arrangement and apparatus.
Source: Author.

$$M_{Sk} = \frac{G_{sp}L^2}{8} + \frac{L_s}{2}\left(W_{eq} + F_{act}\right) \qquad \text{Eq. (40)}$$

$$M_{Sk} = M_{Rk} \qquad \text{Eq. (41)}$$

$$F_{act} = \frac{2M_{Rk}}{L_s} - \left(\frac{G_{sp}L^2}{4L_s} + W_{eq}\right) \qquad \text{Eq. (42)}$$

$M_{Rk}$ must be calculated according to sections 3.3.1 and 3.3.2.

### 3.3.1 Specimens TS2.5_16_0.33 (composite)

The calculation of $M_{Rk}$ was based on two different approaches as follows:

a) MR1 – it is an extension of NBR 6118 (ABNT, 2014) to concrete structures, standard already used to design of aforementioned slabs since composite action is currently neglected. The bending resistance takes into account the strength provided by rebar truss upper chord and wire mesh, which stresses are calculated based on linear strain distribution in cross section.
b) MR2 – it is a simplified way to calculate the bending resistance based on rigid-plastic analysis according to the EN 1994-1-1 (CEN, 2004), to the NBR 8800 (ABNT, 2008) and to Grossi (2016). Contributions of rebar truss upper chord and wire mesh to bending resistance are neglected.

#### 3.3.1.1 Model MR1

Design equations took into account the following hypothesis:

a) The collapse happens due to full plastification in section where maximum sagging bending moment occurred (at center, between line loads). As such, longitudinal shear is not a critical limit state.
b) Both lower chords of rebar truss and CFS channel section undergo yielding at failure. Meanwhile, concrete reaches a compressive strain $\varepsilon_{cu}$ as stated in Eq. (43) and a stress of $\alpha_c f_c$ as defined by Eq. (44), according to NBR 6118 (ABNT, 2014). The coefficient $\alpha_c$ represents the Rusch effect (RUSCH, 1960).

$$\varepsilon_c = \begin{cases} 0.0035 \quad f_c \leq 50\,MPa \\ 0.0026 + 0.0035\left(\dfrac{90 - f_c}{100}\right)^4 \quad f_c > 50\,MPa \end{cases} \qquad \text{Eq. (43)}$$

$$\alpha_c = \begin{cases} 0.85 \quad f_c \leq 50\,MPa \\ 0.85\left(1 - \dfrac{f_c - 50}{200}\right) \quad f_c > 50\,MPa \end{cases} \qquad \text{Eq. (44)}$$

c) Concrete strength in tension is neglected.
d) Depending on plastic neutral axis depth, wire mesh and rebar truss upper chord can work in tension or compression, which must be calculated based on strain distribution.
e) Strains in slab cross section vary linearly from top to bottom for both steel and concrete elements.
f) Stresses in steel reinforcements ($\sigma$) are limited to yield strength $(f_y)$ as stated in the NBR 6118 (ABNT, 2014). It means that if $\sigma = E\varepsilon > f_y$, then $\sigma = f_y$ in tension or compression.
g) Testing apparatus such spreader beams do not introduce normal forces in slab samples.

In this context, Figure 25 represents a typical T-shaped cross-section from the rebar truss composite slab analyzed in this research. In most of cases, reinforcement areas provided by CFS section and lower chords are not sufficient to bring down the reduced plastic neutral axis depth ($\lambda x$) below the concrete flange ($t_f$), i.e., $\lambda x \leq t_f$. Before calculating the bending resistance, one must settle the horizontal equilibrium of forces acting on concrete flange ($C_c$ – compression), on CFS profile ($T_{cfs}$ – tension), on lower chords of rebar truss ($T_{lc}$ – tension), on wire mesh ($F_{wm}$) and on upper chord ($F_{uc}$), according to Eq. (45) to Eq. (47). It's important to state that $F_{wm}$ and $F_{uc}$ can be tension (positive value) or compression (negative value) forces depending on neutral axis depth.

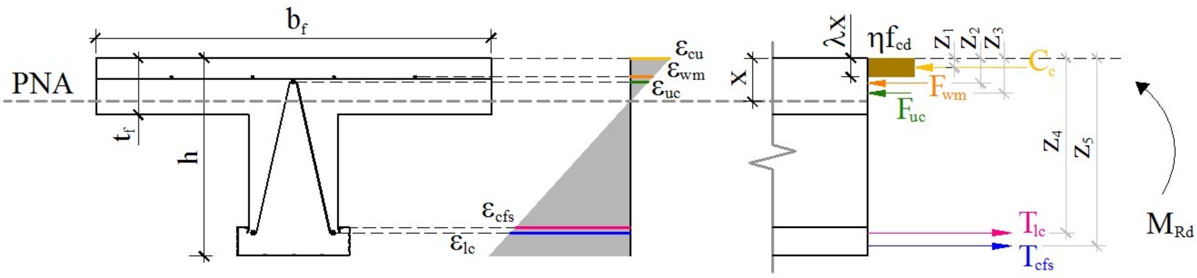


**Figure 25.** Strains, stresses and forces in a typical cross-section from the rebar truss composite slab. Source: Author.

$$\lambda = \begin{cases} 0.8 & f_c \leq 50\ MPa \\ 0.8 - \dfrac{f_c - 50}{400} & f_c > 50\ MPa \end{cases} \qquad \text{Eq. (45)}$$

$$\sum F = 0 \therefore C_c + F_{wm} + F_{uc} + T_{lc} + T_{cfs} = 0 \qquad \text{Eq. (46)}$$

$$-\alpha_c f_c b_f \lambda x + A_{wm}\varepsilon_{wm}E_{wm} + A_{uc}\varepsilon_{uc}E_{uc} + f_{yrt}A_{lc} + f_{yF}A_{cfs} = 0 \qquad \text{Eq. (47)}$$

Where $f_c$ is concrete compressive strength, $\alpha_c$ is defined by Eq. (44), $b_f$ is the width of concrete compression flange, $x$ is the plastic neutral axis depth, $A_{wm}$ is the wire mesh reinforcement area in $b_f$, $\varepsilon_{wm}$ is the strain in wire mesh, $E_{wm}$ is the Young's module of wire mesh, $A_{uc}$ is the upper chord area, $\varepsilon_{uc}$ is the strain in upper chord, $E_{uc}$ is the upper chord Young's module, $f_{yF}$ is the yield strength of CFS lipped channel section, $A_{cfs}$ is the area of CFS section, $f_{yrt}$ is the yield strength of rebar truss and, finally, $A_{lc}$ is the reinforcement area of lower chords pair.

It's important to state that $\varepsilon_{wm}$ and $\varepsilon_{uc}$ in Eq. (47) are defined according to neutral axis depth, which can be obtained through trigonometry as shown in Figure 26a. They are calculated according to Eq. (48) to Eq. (51).

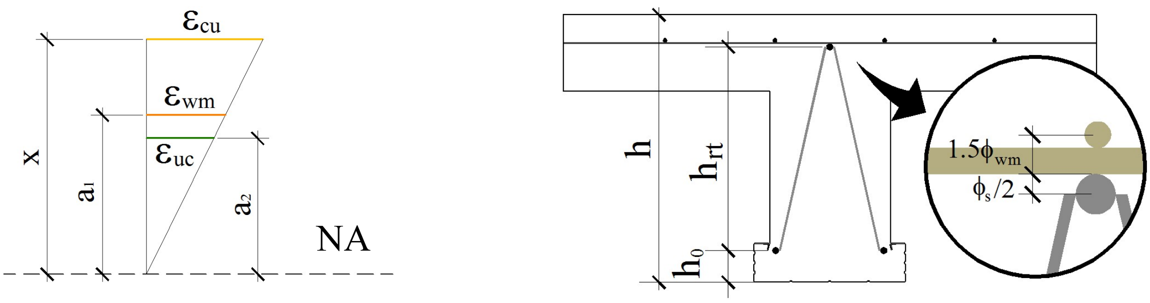


(a) (b)

**Figure 26.** Strains in upper chord of rebar truss and wire mesh.
Source: Author.

$$a_1 = x - \left[h - \left(h_0 + h_{rt} + \frac{\phi_s}{2} + 1.5\phi_{wm}\right)\right] \quad \text{Eq. (48)}$$

$$\varepsilon_{wm} = \frac{\varepsilon_{cu}}{x} a_1 \quad \text{Eq. (49)}$$

$$a_2 = x - [h - (h_0 + h_{rt})] \quad \text{Eq. (50)}$$

$$\varepsilon_{uc} = \frac{\varepsilon_{cu}}{x} a_2 \quad \text{Eq. (51)}$$

Where $h$ is the slab depth, $h_{rt}$ is the rebar truss height from center to center of chords, $h_0$ is the distance from center of lower chords to base of CFS section, taken as $25\ mm$, $\phi_s$ is the diameter of upper chord, $\phi_{wm}$ is the diameter of wire mesh and $x$ is the neutral axis depth.

If $\varepsilon_{wm} > {f_{ywm}}/{E_{wm}}$, the stress in wire mesh calculated as $\varepsilon_{wm}E_{wm}$ in Eq. (47) must be replaced by $f_{ywm}$ – the yield strength of wire mesh. Same consideration is addressed to stress in the upper chord calculated as $\varepsilon_{uc}E_{uc}$.

Afterwards, once calculated the neutral axis depth by force equilibrium, all forces depicted in Figure 25 are defined. Then, the bending resistance based on plastic analysis is obtained from Eq. (52). Moreover, the distances from all forces line action to concrete top are referred as $z_1$ to $z_5$, calculated according to Eq. (53) to Eq. (57), where $y_{G,cfs}$ is the distance from center of gravity of CFS section to bottom, taken as $10.6\ mm$.

$$M_{Rk} = C_c z_1 + F_{wm} z_2 + F_{uc} z_3 + T_{lc} z_4 + T_{cfs} z_5 \quad \text{Eq. (52)}$$

$$z_1 = \frac{\lambda x}{2} \quad \text{Eq. (53)}$$

$$z_2 = h - \left(h_0 + h_{rt} + \frac{\phi_s}{2} + 1.5\phi_{wm}\right) \quad \text{Eq. (54)}$$

$$z_3 = h - (h_0 + h_{rt}) \quad \text{Eq. (55)}$$

$$z_4 = h - h_0 \quad \text{Eq. (56)}$$

$$z_5 = h - y_{G,cfs} \quad \text{Eq. (57)}$$

3.3.1.2 Model MR2

In case of this model, all forces are included in the calculation of bending resistance. However, PNA depth is not reduced by $\lambda$ as in MR1. As such, equations took into account the following hypothesis:

a) The collapse happens due to full plastification in section where maximum sagging bending moment occurred (at center, between line loads). As such, longitudinal shear is not a critical limit state.
b) All steel components (CFS profile and rebars) undergo yielding at failure.
c) Concrete strength in tension is neglected.
d) Testing apparatus such spreader beams do not introduce normal forces in slab samples.

Figure 27 represents a typical T-shaped cross-section from the rebar truss composite slab analyzed in this research. The bending resistance ($M_{Rk}$) must be calculated according to Eq. (68) as follows.

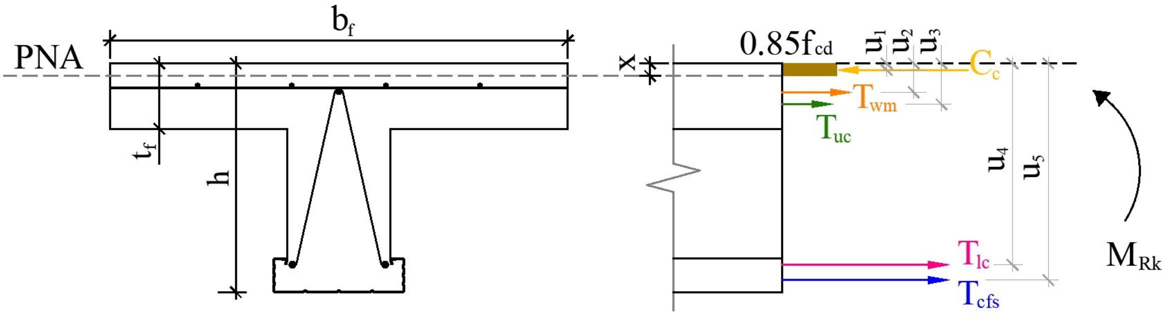


**Figure 27.** Stresses and forces in a cross-section from the rebar truss composite slab – rigid-plastic analysis. Source: Author.

$$T_{wm} = f_{ywm}A_{wm} \qquad \text{Eq. (58)}$$

$$T_{uc} = f_{yrt}A_{uc} \qquad \text{Eq. (59)}$$

$$T_{lc} = f_{yrt}A_{lc} \qquad \text{Eq. (60)}$$

$$T_{cfs} = f_{yF}A_{cfs} \qquad \text{Eq. (61)}$$

$$x = \frac{T_{cfs} + T_{lc}}{0.85 f_c b_f} \qquad \text{Eq. (62)}$$

$$u_1 = \frac{x}{2} \qquad \text{Eq. (63)}$$

$$u_2 = h - \left(h_0 + h_{rt} + \frac{\phi_s}{2} + 1.5\phi_{wm}\right) \qquad \text{Eq. (64)}$$

$$u_3 = h - (h_0 + h_{rt}) \qquad \text{Eq. (65)}$$

$$u_4 = h - h_0 \qquad \text{Eq. (66)}$$

$$u_5 = h - y_{G,cfs} \qquad \text{Eq. (67)}$$

$$M_{Rk} = T_{wm}(u_2 - u_1) + T_{uc}(u_3 - u_1) + T_{lc}(u_4 - u_1) + T_{cfs}(u_5 - u_1) \qquad \text{Eq. (68)}$$

As presented in section 3.3.1.1, $h_0$ is the distance from center of lower chords to base of CFS section, taken as $25\ mm$, and $y_{G,cfs}$ is the distance from center of gravity of CFS section to bottom, taken as $10.6\ mm$.

### 3.3.2 Specimens RCS2.5_16_0.33 (non-composite)

The bending resistance of reinforced concrete slab samples should be determined in according to section 3.3.1.1, although suppressing the contributing from CFS section by eliminating the force $T_{cfs}$ from all equations.

## 3.4 PREPARATION OF SLAB SAMPLES

All slab samples were prepared in the Laboratory of Structures from the Federal University of Espírito Santo. On account of equipment availability at the lab, specimens were cast in testing position and kept propped until concrete hardening. Preparation procedure is detailed in Table 8 and additional pictures from experiments are found into Appendix A.

**Table 8.** Details regarding production of slab samples (continues).

| STEP | DESCRIPTION | ILLUSTRATION |
|---|---|---|
| A | Wood shuttering was prepared and adjusted over both roller and pinned supports. Three propping lines divided the isostatic length of 250.00 cm in four segments of 75.00 cm each to transfer loads to ground whilst concrete had not hardened yet. Since group TS2.5_16_0.33 had the CFS shuttering, no wood formwork was needed at bottom. |  **Figure 28.** Step A. |
| B | In case of TS2.5_16_0.33 samples, two CFS profiles were fastened to rebar trusses model TB-16L through 7 uniformly distributed plastic connectors, placed inside formworks with EPS blocks. |  **Figure 29.** Step B. |
| C | On the other hand, in case of RCS2.5_16_0.33, four small pieces of CFS section were placed in each rib to grant same EPS spacing and rebar truss position than TS2.5_16_0.33. |  **Figure 30.** Step C. |
| D | The Q75 wire mesh was tied up to rebar trusses upper chord with wire. Additionally, plastic spacers supported the edges of wire mesh to grant a minimum concrete top of 2.50 $cm$ over it. | 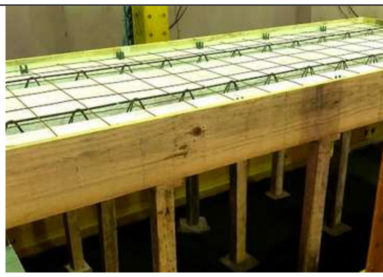 **Figure 31.** Step D. |
| E | After full assemblage, DESMOL® from Vedacit was applied over exposed wood to ease its removal after concrete hardening. |   **Figure 32.** Step E. |

**Table 8.** Details regarding production of slab samples (conclusion).

| | | |
|---|---|---|
| F | The concrete pouring operation happened with aid of mixer truck and pump. Since it was self-consolidating (SCC), no vibration was needed. | 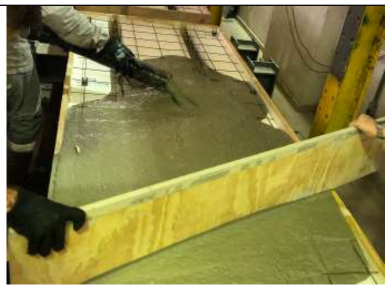 **Figure 33.** Step F. |
| G | After concreting the first slab samples (model "a"), the 18 specimens to concrete cylinder strength and modulus of elasticity were molded. |  **Figure 34.** Step G. |
| H | Immediately after step (f), chemical curing agent CURING® from Vedacit (Figure 16b) was sprayed over exposed concrete surface to avoid water loss. Then, after 6 hours, a second and thicker layer of CURING® was applied with woolen roller. Finally, a plastic canvas covered the specimen for fourteen days. |  **Figure 35.** Step H. |
| I | Formworks and props were removed 14 days after concrete casting in case of TS2.5_16_0.33 samples and 21 days later for RSC2.5_16_0.33 specimens. |  **Figure 36.** Step I. |
| | Position of line loads, strain gauges (SG) and LVDT was marked in specimen surface. |  **Figure 37.** Step J. |

The samples were instrumented in the central section $L/2$ according to Figure 38, where the maximum sagging bending moment occurs. Nine strain gauges (SG1 to SG9) were uniformly distributed in the concrete top flange of both prototypes to assess the stress distribution along the flange length $B_p$. In addition, two extra strain gauges were placed on bottom ribs to measure tension strains (SG10 and SG11). In case of samples TS2.5_16_0.33, cast with CFS shuttering, these SG's are addressed to steel while, on the other hand, they were suppressed into RCS2.5_16_0.33 specimens because the concrete works under tension at bottom ribs. SG10 and SG11 distanced $235\ mm$ from edges.

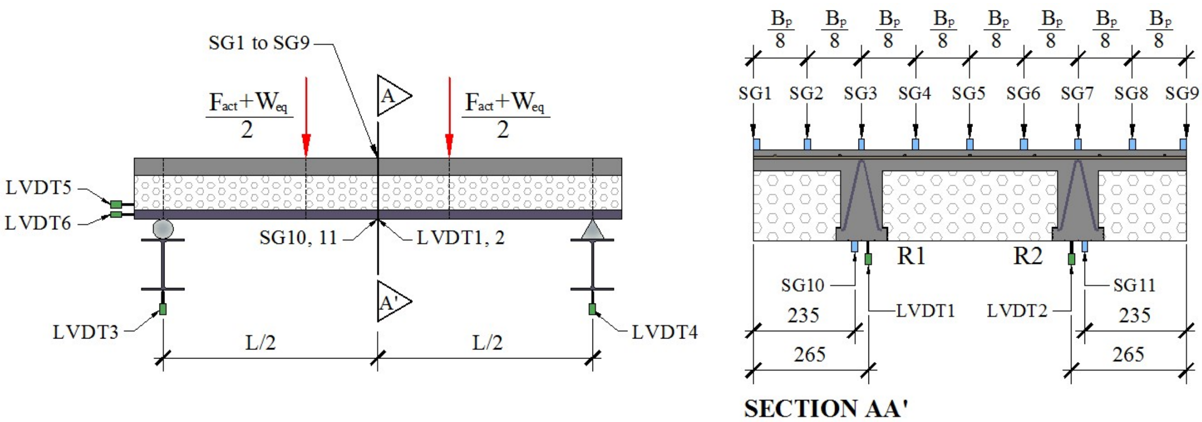


**Figure 38.** Instrumentation scheme of tested samples.
Source: Author.

In addition, LVDT1 and LVDT2 were placed on bottom of central section $265\ mm$ far from edges to assess vertical displacements at $L/2$. It allowed for the evaluation of slab's stiffness and, consequently, the load-displacement response of such samples. Two extra recorders – LVDT3 and LVDT4 – are located under supports to measure their displacements along test, which were discounted from LVDT1 and LVDT2 values not to affect measured slab stiffness. Finally, LVDT5 and LVDT6 were located in the edges of rib R2 at level of channel lips, respectively on steel and on concrete, which difference represented the relative displacement between the materials. These recordings are suppressed on RCS2.5_16_0.33 group. It's important to state that all LVDT's have a maximum stroke of $150\ mm$.

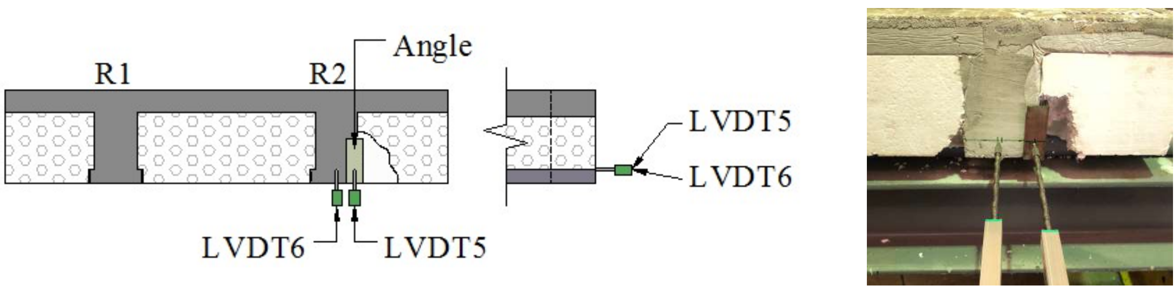


(a) (b)

**Figure 39.** Position of LVDTs in the edge of R2 to record relative displacement between steel and concrete.
Source: Author.

Whereas LVDT’s where just pointed and leveled at measuring locations in the day of testing, SG’s required previous installation, which was processed a week before. The complete process is summarized in Table 9.

**Table 9.** Installation process of strain gauges.

| STEP | DESCRIPTION | PROCESS |
|---|---|---|
| A | Concrete top was regularized with sandpaper and, afterwards, washed to remove the dust. |  **Figure 40.** Step A. |
| B | In SG positions, an epoxy resin from SIKA was applied to concrete surface to fill voids and smooth the surface. After its hardening 24h after application, the product was sanded and washed. |  **Figure 41.** Step B. |
| C | Isopropyl alcohol was applied to surface to conclude cleaning. |  **Figure 42.** Step C. |
| D | SG’s were pasted to surface with high strength glue with quick drying. |   **Figure 43.** Step D. |
| E | SG’s were installed on concrete surface. | 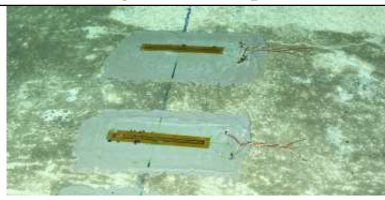 **Figure 44.** Step E. |
| F | Surface was protected with EVA until testing day. |  **Figure 45.** Step F. |

Finally, as the steel surface is more regular than concrete's, the installation of six SG's on steel ribs of followed only steps A, C and D from Table 9.

## 3.5 TESTING PROCEDURE

The bending tests were carried out in accordance with EN 1994-1-1 (CEN, 2004), as explained in 2.3.2. The first specimen (model "a") from both TS2.5_16_0.33 and RCS2.5_16_0.33 groups were loaded until failure to assess the collapse force $F_{act,max}$. Then, samples "b" and "c" were tested under cyclic loads of 30%, 37,5% and 45% of $F_{act,max}$ followed by rupture, as previously performed by Candido (2021).

Load was introduced on samples with a hydraulic actuator with capacity of $50\ tf$ and maximum stroke of $200\ mm$ (Figure 46). Nonetheless, since the equipment is hand-operated (not automated), it was not feasible to reach 5000 cycles within an hour as required by the EN 1994-1-1 (CEN, 2004). A hinge was placed immediately below the piston, transferring the load to a steel plate above the load cell, which was fabricated by Gefran with capacity of $300\ kN$. Finally, a short column was employed (as the cylinder) to compensate the height differences in assemblage. Note that both Column 1 and the hydraulic actuator are fixed to the top beam by four tie rods plus a steel plate and that's the reason why their dead loads are not deposited on samples during tests.

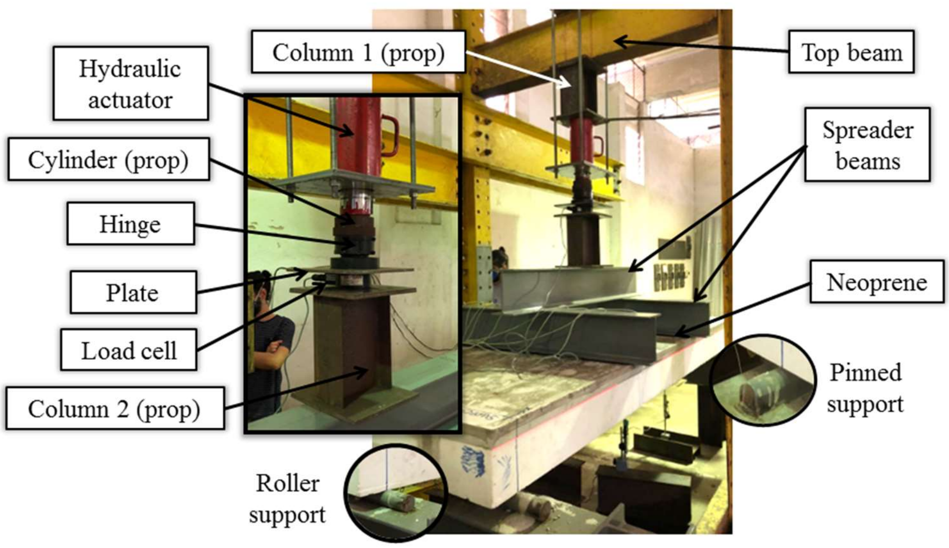


**Figure 46.** Testing apparatus: introduction of loads on slab samples.
Source: Author.

## 3.6 LOAD-DISPLACEMENT RESPONSE

As summarized in Table 2, the seven models found in the specialized literature to assess the maximum vertical displacements of composite slabs are based on the effective moment of inertia $(I_{eff})$, which takes into account the moments of inertia of uncracked $(I_{cf})$ and cracked $(I_{II})$ sections as well as the ratio between $M_a$ and $M_r$, respectively the moment acting on serviceability and the cracking moment of slab.

In this context, the calculation of aforementioned parameters must be performed after homogenizing the cross section considering short duration effect. In this case, concrete is chosen as base material and, then, properties of CFS section and rebar truss are converted according to Eq. (69) and Eq. (70).

$$\alpha_{E,s} = \frac{E_{a,s}}{E_{cs}} \qquad \text{Eq. (69)}$$

$$\alpha_{E,rt} = \frac{E_{a,rt}}{E_{cs}} \qquad \text{Eq. (70)}$$

Where $E_{a,s}$, $E_{a,rt}$ and $E_{cs}$ are the moduli of Young of shuttering, rebar truss and concrete, respectively.

### 3.6.1 Mean value of centroid position and moment of inertia of rebar truss

First, consider a general section of a given rebar truss $(0 \leq x \leq p/2)$, according to Figure 47, where $p$ is the rebar truss pitch taken as $200\ mm$. For each one, the mean value of centroid position and moment of inertia must be calculated using Eq. (73) and Eq. (75), respectively. These values were calculated for the rebar truss model previously presented in Table 6 are shown in Table 10.

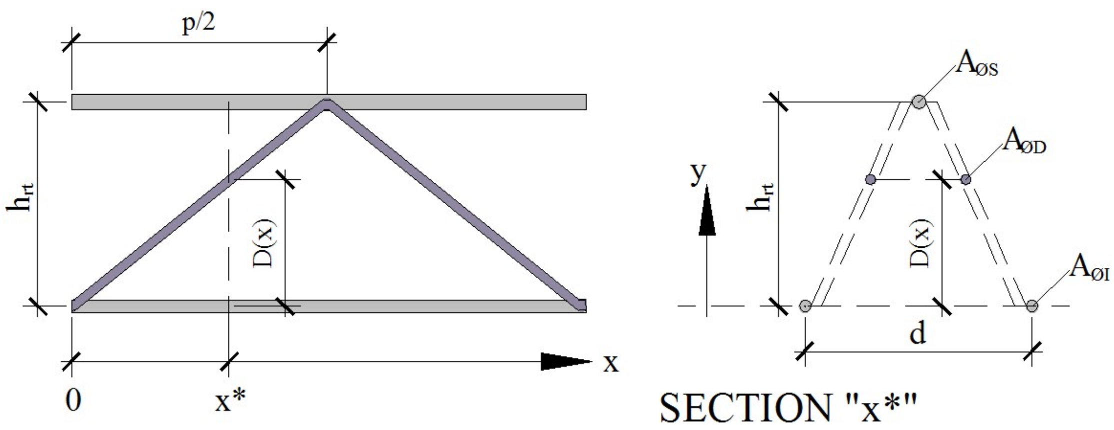


**Figure 47.** General rebar truss section.
Source: Author.

$$D(x) = \frac{2h_{rt}x}{p}, 0 \leq x \leq \frac{p}{2} \qquad \text{Eq. (71)}$$

$$\bar{y}(x) = \frac{2A_{\emptyset D}D(x) + A_{\emptyset S}h_{rt}}{2A_{\emptyset I} + 2A_{\emptyset D} + A_{\emptyset S}} \qquad \text{Eq. (72)}$$

$$y_{G,rt} = \frac{2}{p}\int_0^{p/2} \bar{y}(x)\,dx \qquad \text{Eq. (73)}$$

$$I_x(x) = \frac{\pi\emptyset_S^4}{64} + \frac{\pi\emptyset_D^4}{32} + \frac{\pi\emptyset_I^4}{32} + A_{\emptyset S}[h_{rt} - \bar{y}(x)]^2 + 2A_{\emptyset D}[\bar{y}(x) - D(x)]^2 + 2A_{\emptyset I}[\bar{y}(x)]^2 \qquad \text{Eq. (74)}$$

$$I_{G,rt} = \frac{2}{p}\int_0^{p/2} I_x(x)\,dx \qquad \text{Eq. (75)}$$

**Table 10.** Geometric properties of some rebar truss employed in this research.

| **Model** | $A_{\emptyset S}$ $[cm]$ | $A_{\emptyset D}$ $[cm^2]$ | $A_{\emptyset I}$ $[cm^2]$ | $y_{G,rt}$ $[cm^2]$ | $I_{G,rt}$ $[cm^4]$ |
|---|---|---|---|---|---|
| TB 8L | 0.283 | 0.139 | 0.139 | 4.03 | 9.96 |

Source: ARCELORMITTAL BRASIL (2017a).

### 3.6.2 Uncracked moment of inertia of the composite slab

Cross-sectional dimensions are presented in Figure 48. The calculation of neutral axis depth measured from the top and the uncracked moment of inertia must follow Eq. (76)–Eq. (80), case in which all concrete section contributes to slab stiffness.

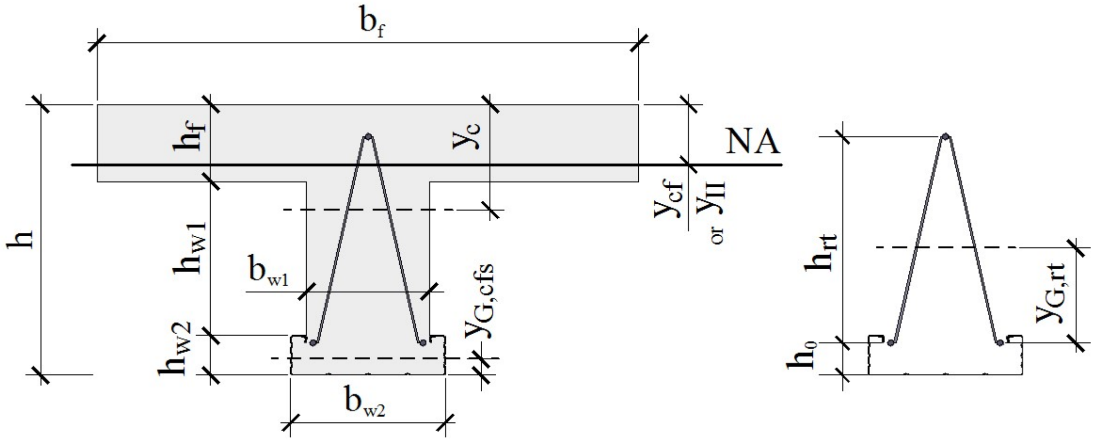


**Figure 48.** Calculation of moments of inertia of rebar truss ribbed slab analyzed in this research. Source: Author.

$$A_c = b_f h_f + b_{w1} h_{w1} + b_{w2} h_{w2} \qquad \text{Eq. (76)}$$

$$y_c = \frac{\frac{b_f h_f^2}{2} + b_{w1} h_{w1}\left(\frac{h_{w1}}{2} + h_f\right) + b_{w2} h_{w2}\left(\frac{h_{w2}}{2} + h_{w1} + h_f\right)}{A_c} \qquad \text{Eq. (77)}$$

$$I_c = \frac{b_f h_f^3}{12} + b_f h_f \left(y_c - \frac{h_f}{2}\right)^2 + \frac{b_{w1} h_{w1}^3}{12} + b_{w1} h_{w1}\left(y_c - h_f - \frac{h_{w1}}{2}\right)^2 + \frac{b_{w2} h_{w2}^3}{12} + b_{w2} h_{w2}\left(y_c - \frac{h_{w2}}{2} - h_{w1} - h_f\right)^2 \qquad \text{Eq. (78)}$$

$$y_{cf} = \frac{A_c y_c + \alpha_{E,s} A_{cfs}\left(h - y_{G,cfs}\right) + \alpha_{E,rt} A_{rt}\left(h - h_0 - y_{G,rt}\right)}{A_c + \alpha_{E,s} A_{cfs} + \alpha_{E,rt} A_{rt}} \qquad \text{Eq. (79)}$$

$$I_{cf} = I_c + A_c\left(y_c - y_{cf}\right)^2 + \alpha_{E,s}\left[I_{cfs} + A_{cfs}\left(h - y_{G,cfs} - y_{cf}\right)^2\right] + \alpha_{E,rt}\left[I_{G,rt} + A_{rt}\left(h - h_0 - y_{G,rt} - y_{cf}\right)^2\right] \qquad \text{Eq. (80)}$$

Where $A_{cfs}$ is the cross-sectional area of CFS section, $A_{rt}$ is area of rebar truss cross-section and $A_c$ is the area of concrete section. In addition, $y_c$ represents the distance between the geometric center of concrete T-shaped section and its top.

### 3.6.3 Cracked moment of inertia of the composite slab

Finally, the cracked moment of inertia must be obtained by neglecting the contribution of concrete in tension. On account of small reinforcement areas provided by both rebar truss and CFS section in comparison with concrete flange, the neutral axis $(y_{II})$ does not cross the web in most of cases as this one. Therefore, after solving Eq. (81) to $y_{II}$, the neutral axis depth is determined.

$$\frac{b_f y_{II}^2}{2} - \alpha_{E,rt} A_{rt}\left(h - h_0 - y_{G,rt} - y_{II}\right) - \alpha_{E,s} A_{cfs}\left(h - y_{G,cfs} - y_{II}\right) = 0$$

$$y_{II} = \frac{-V + \sqrt{V^2 - 4UW}}{2U} \leq h_f$$

$$U = \frac{b_f}{2} \qquad \text{Eq. (81)}$$

$$V = \alpha_{E,rt} A_{rt} + \alpha_{E,s} A_{cfs}$$

$$W = -\alpha_{E,rt} A_{rt}\left(h - h_0 - y_{G,rt}\right) - \alpha_{E,s} A_{cfs}\left(h - y_{G,cfs}\right)$$

Afterwards, the cracked moment of inertia is obtained according to Eq. (82).

$$I_{II} = \frac{b_f y_{II}^3}{3} + \alpha_{E,s}\left[I_{cfs} + A_{cfs}\left(h - y_{G,cfs} - y_{II}\right)^2\right] + \alpha_{E,rt}\left[I_{G,rt} + A_{rt}\left(h - h_0 - y_{G,rt} - y_{II}\right)^2\right] \qquad \text{Eq. (82)}$$

### 3.6.4 Effective moment of inertia

When calculating the effective moment of inertia ($I_{eff}$) based on both $I_{cf}$ and $I_{II}$, the cracking moment $M_r$ must be defined according to Eq. (35) and Eq. (36). Note that the tensile strength of concrete in bending was not assessed experimentally, which must be obtained by standardized formulae Eq. (35). Then, the moment acting in serviceability $M_a$ must be accounted as Eq. (40).

# 4

# RESULTS AND DISCUSSIONS

## 4.1 CHARACTERIZATION OF MATERIALS

### 4.1.1 Concrete

#### 4.1.1.1 Slump-flow

Firstly, results from slump flow test are shown in Table 11, where $d_1$ represents the largest diameter of the circular concrete spread, $d_2$ is the circular spread taken perpendicularly to $d_1$ and $SF$ is the slump flow (the average value of $d_1$ and $d_2$). Although the concrete from group RCS2.5_16_0.33 did not attend to SF2 flow class requirement, concrete casting was not affected.

**Table 11.** Slump flow test result.

| Test group | $d_1$ $(cm)$ | $d_2$ $(cm)$ | $SF$ $(cm)$ | Flow class (NBR 15823-2 – ABNT, 2017) | Expected SF $(cm)$ |
|---|---|---|---|---|---|
| TS2.5_16_0.33 | 70.0 | 73.0 | 71.5 | SF2 | $66.0 \leq SF \leq 75.0$ |
| RCS2.5_16_0.33 | 60.0 | 61.0 | 60.5 | SF1 | $66.0 \leq SF \leq 75.0$ |

#### 4.1.1.2 Cylindrical strength

Results calculated according to the NBR 5739 (ABNT, 2018) are reported in Table 12 and Table 13 for groups TS2.5_16_0.33 and RCS2.5_16_0.33, respectively, where MV is the mean value, SD is the standard deviation and CV is the coefficient of variation $(CV = SD/MV)$.

In the first case, mean values for both curing processes diverge 12.8% from one to another, suggesting disparity among results. However, since CC specimens were kept under the same conditions that the slab samples, compressive strength is preferably considered as $f_{c34} = 59{,}2\,MPa$. Note that $CV$ is 9% and greater deviation between $f_c$ and $MV$ is around the acceptable value of 10%.

**Table 12.** Concrete cylinder compressive strength from TS2.5_16_0.33 group.

| **Wet curing (WC)** | | | **Chemical curing (CC)** | | |
|---|---|---|---|---|---|
| **Specimen** | **$f_{ci}$ (MPa)** | **$f_c$/MV** | **Specimen** | **$f_{ci}$ (MPa)** | **$f_c$/MV** |
| WC_1 | 54.5 | 1.038 | CC_2 | 55.0 | 0.928 |
| WC_2 | 47.3 | 0.901 | CC_7 | 53.0 | 0.895 |
| WC_3 | 54.8 | 1.043 | CC_4 | 58.6 | 0.990 |
| WC_4 | 53.6 | 1.020 | CC_8 | 65.4 | 1.104 |
| WC_5 | 52.4 | 0.998 | CC_9 | 64.1 | 1.082 |
| **MV** | 52.5 | | **MV** | 59.2 | |
| **SD** | 3.0 | | **SD** | 5.4 | |
| **CV** | 6% | | **CV** | 9% | |

In the second case, mean values diverge 2.6% from one to another, indicating that both curing processes have led to same results. Since CC specimens were kept under the same conditions that the slab samples, compressive strength is preferably considered as $f_{c34} = 42{,}8\,MPa$. Note that $CV$ is 6% and greater deviation between $f_c$ and $MV$ is 7,7%, which are values less than 10%, therefore within an acceptable limit.

**Table 13.** Concrete cylinder compressive strength from RCS2.5_16_0.33 group.

| **Wet curing** | | | **Chemical curing** | | |
|---|---|---|---|---|---|
| **Specimen** | **$f_c$ (MPa)** | **$f_c$/MV** | **Specimen** | **$f_c$ (MPa)** | **$f_c$/MV** |
| WC_1 | 48.3 | 1.100 | CC_2 | 42.4 | 0.991 |
| WC_4 | 39.8 | 0.906 | CC_7 | 42.8 | 0.999 |
| WC_3 | 41.5 | 0.946 | CC_4 | 42.9 | 1.003 |
| WC_7 | 45.6 | 1.038 | CC_8 | 39.5 | 0.923 |
| WC_9 | 44.4 | 1.010 | CC_9 | 46.4 | 1.083 |
| **MV** | 43.9 | | **MV** | 42.8 | |
| **SD** | 3.4 | | **SD** | 2.4 | |
| **CV** | 8% | | **CV** | 6% | |

#### 4.1.1.3 Secant modulus of elasticity

Results obtained according to NBR 8522 (ABNT, 2017b) are reported in Table 14 and Table 15 for groups TS2.5_16_0.33 and RCS2.5_16_0.33, respectively. Note that mean values of secant modulus of elasticity for wet and chemical curing are 14% apart from each other in first case and 10% in the second one. Besides, when first concrete cylindrical specimen was tested from group TS2.5_16_0.33, the difference between $f_c$ and $f_{c,ef}$ was almost 20%, corresponding to the limit defined in the code NBR 8522 (ABNT, 2017b). As such, an extra specimen was introduced in each group to reduce result dispersion. Finally, results obtained from chemical curing were employed to calculate displacements of composite slab since they were cured under same conditions than full-scale specimens.

**Table 14.** Secant Young's module from TS2.5_16_0.33.

| **Wet curing** | | | | **Chemical curing** | | | |
|---|---|---|---|---|---|---|---|
| **Specimen** | **$E_{cs}$ (GPa)** | **$f_c$ (MPa)** | **$f_c/f_{c,ef}$** | **Specimen** | **$E_{cs}$ (GPa)** | **$f_c$ (MPa)** | **$f_c/f_{c,ef}$** |
| WC_6 | 39.2 | 41,2 | 0,81 | CC_1 | 36.9 | 62,9 | 1,16 |
| WC_7 | 38.7 | 53,0 | 1,04 | CC_3 | 30.2 | 59,8 | 1,11 |
| WC_8 | 39.6 | 50,1 | 0,98 | CC_5 | 36.9 | 58,6 | 1,09 |
| WC_9 | 39.3 | 47,3 | 0,93 | CC_6 | 33.5 | 53,5 | 0,99 |
| **MV** | 39.2 | | | **MV** | 34.3 | | |
| **SD** | 0.4 | | | **SD** | 3.2 | | |
| **CV** | 0.9% | | | **CV** | 9.3% | | |

**Table 15.** Secant Young's module from RCS2.5_16_0.33.

| **Wet curing** | | | | **Chemical curing** | | | |
|---|---|---|---|---|---|---|---|
| **Specimen** | **$E_{cs}$ (GPa)** | **$f_c$ (MPa)** | **$f_c/f_{c,ef}$** | **Specimen** | **$E_{cs}$ (GPa)** | **$f_c$ (MPa)** | **$f_c/f_{c,ef}$** |
| WC_2 | 27.9 | 45.7 | 1.04 | CC_1 | 26.4 | 45.1 | 1.06 |
| WC_5 | 30.4 | 44.1 | 1.00 | CC_4 | 28.8 | 37.5 | 0.88 |
| WC_6 | 30.3 | 40.3 | 0.91 | CC_6 | 28.3 | 45.7 | 1.07 |
| WC_8 | 31.6 | 45.5 | 1.03 | CC_7 | 26.1 | 39.0 | 0.92 |
| **MV** | 30.1 | | | **MV** | 27.4 | | |
| **SD** | 1.5 | | | **SD** | 1.4 | | |
| **CV** | 5.1% | | | **CV** | 4.9% | | |

Figure 49 shows a stress-strain curve and stress increments against time during the test, which are employed in the determination of modulus of elasticity. Graphics refer to specimen WC_8 from TS2.5_16_0.33 group. The reminiscent results are reported into Appendix B.

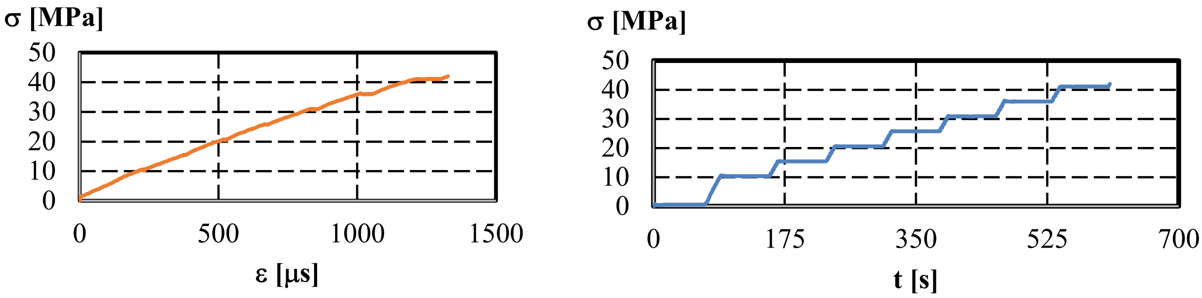


(a) (b)

**Figure 49.** Outputs from modulus of elasticity test: (a) stress-strain; and (b) stress-time curves.
Source: Author.

#### 4.1.1.4 Specific mass and weight

Results are expressed in Table 16 for the two test groups. It's important to state that data set shows to be homogeneous on account of reduced standard deviation and coefficient of variation 0.7%, which is less than 10%. As such, mean values are taken as representative specific mass and weight of concrete. Note that $\emptyset_{ave}$ is the average value of cylindrical specimen diameter, $h$ is the specimen height, $m$ is the specimen mass, $\rho_c$ is the concrete specific mass and $\gamma_c$ is the specific weight.

**Table 16.** Calculation of concrete specific mass and weight.

| SP | TS2.5_16_0.33 | | | | | RCS2.5_16_0.33 | | | | |
|---|---|---|---|---|---|---|---|---|---|---|
| | $\emptyset_{ave}$ (mm) | h (mm) | m (g) | $\rho_c$ (kg/m³) | $\gamma_c$ (kN/m³) | $\emptyset_{ave}$ (mm) | h (mm) | m (g) | $\rho_c$ (kg/m³) | $\gamma_c$ (kN/m³) |
| CC_1 | 100.7 | 197.7 | 3582 | 2275.2 | 22.3 | 100.3 | 190.9 | 3205 | 2124.2 | 20.8 |
| CC_2 | 100.5 | 196.9 | 3599 | 2303.5 | 22.6 | 100.3 | 193.8 | 3314 | 2162.2 | 21.2 |
| CC_3 | 99.8 | 198.2 | 3590 | 2314.9 | 22.7 | 100.1 | 192.0 | 3211 | 2117.8 | 20.8 |
| CC_4 | 100.7 | 198.8 | 3667 | 2318.3 | 22.7 | 101.1 | 195.5 | 3358 | 2143.0 | 21.0 |
| CC_5 | 100.2 | 197.5 | 3579 | 2297.9 | 22.5 | 100.1 | 188.5 | 3177 | 2146.4 | 21.1 |
| CC_6 | 100.2 | 197.8 | 3580 | 2296.5 | 22.5 | 100.7 | 192.0 | 3292 | 2152.1 | 21.1 |
| CC_7 | 100.9 | 197.8 | 3627 | 2292.9 | 22.5 | 100.3 | 191.7 | 3243 | 2141.2 | 21.0 |
| CC_8 | 99.6 | 199.4 | 3617 | 2326.7 | 22.8 | 99.9 | 191.9 | 3229 | 2147.9 | 21.1 |
| CC_9 | 100.0 | 198.2 | 3579 | 2298.8 | 22.6 | 100.1 | 194.5 | 3235 | 2119.4 | 20.8 |
| | | | **MV** | 2302.7 | 22.6 | | | **MV** | 2139.4 | 21.0 |
| | | | **SD** | 15.4 | 0.2 | | | **SD** | 15.5 | 0.2 |
| | | | **CV** | 0.7% | 0.7% | | | **CV** | 0.7% | 0.7% |

#### 4.1.1.5 Summary

Concrete properties employed in analysis are summarized in Table 17. Whereas all groups were based on same mix design, results did not show great accordance, in special when compared to (Candido, 2021). These sharp deviations that can be attributed to variations in additive proportions during mixture, which probably have led to air incorporation into concrete matrix, resulting in reduced strength and higher porosity of RCS2.5_16_0.33 samples as observed. Moreover, note that specific mass get reduced in $163.3\ kg/m^3$ from second to third group. On account of self-consolidation characteristic, vibration was not imposed during concrete samples preparation and, on the other hand, steel cylindrical molds were properly oiled. As such, disturbs on preparation stage may have minimally influenced on mechanical properties of employed concretes.

**Table 17.** Excerpt of concrete properties.

| GROUP | COMPRESSIVE STRENGTH $f_c\ (MPa)$ | | MODULUS OF ESLASTICITY $E_{cs}\ (GPa)$ | | SPECIFIC MASS $\rho_c\ (kg/m^3)$ | SPECIFIC WEIGHT $\gamma_c\ (kN/m^3)$ |
|---|---|---|---|---|---|---|
| | WC | CC | WC | CC | | |
| TS2.5_16_0.25 (Candido, 2021) | 68.6 | 45.8 | 35.2 | 34.5 | 2400.0 | 23.5 |
| TS2.5_16_0.33 | 52.5 | 59.2 | 39.2 | 34.3 | 2302.7 | 22.6 |
| RCS2.5_16_0.33 | 43.9 | 42.8 | 30.1 | 27.4 | 2139.4 | 21.0 |

### 4.1.2 Steel

The mechanical properties from steels employed in this research are summarized in Table 18, where $f_y$ denotes the yield strength, $f_u$ is the ultimate strength and $E$ is the longitudinal modulus of elasticity.

**Table 18.** Excerpt of steel properties.

| GROUP | CFS SECTION | | | REBAR TRUSSES | | | WIRE MESHES | | |
|---|---|---|---|---|---|---|---|---|---|
| | $f_y$ $(MPa)$ | $f_u$ $(MPa)$ | $E$ $(GPa)$ | $f_y$ $(MPa)$ | $f_u$ $(MPa)$ | $E$ $(GPa)$ | $f_y$ $(MPa)$ | $f_u$ $(MPa)$ | $E$ $(GPa)$ |
| TS2.5_16_0.25 (Candido, 2021) | 299.1 | 432.6 | 200 | 600 | 630 | 210 | 600 | 630 | 210 |
| TS2.5_16_0.33 | 299.1 | 432.6 | 200 | 600 | 630 | 210 | 600 | 630 | 210 |
| RCS2.5_16_0.33 | -- | -- | -- | 600 | 630 | 210 | 600 | 630 | 210 |

## 4.2 LOAD CAPACITY

The experiment as previously presented consisted in assessing the strength of the six slab specimens through the four-point bending test. In addition to the maximum external force applied by the hydraulic actuator $(F_{act})$, dead loads from testing apparatus $\left(W_{eq}\right)$ and slab samples $\left(G_{sp}\right)$ must be accounted for calculation of experimental bending resistance $M_{Rk}$. As such, the total forced imposed by testing equipment as depicted in Figure 46 is calculated according to Table 19, which leads to $W_{eq} = 1.44\ kN$.

**Table 19.** Dead loads of testing equipment.

<table>
<tr><th colspan="2">DESCRIPTION</th><th>MASS $(kg)$</th><th>WEIGHT $(kN)$</th></tr>
<tr><td rowspan="2">Neoprene</td><td>A</td><td>1.3</td><td>0.01</td></tr>
<tr><td>B</td><td>1.3</td><td>0.01</td></tr>
<tr><td rowspan="3">Spreader beams</td><td>Bottom A</td><td>33.2</td><td>0.33</td></tr>
<tr><td>Bottom B</td><td>33.0</td><td>0.32</td></tr>
<tr><td>Top</td><td>40.1</td><td>0.39</td></tr>
<tr><td colspan="2">Column 2 (prop)</td><td>16.5</td><td>0.16</td></tr>
<tr><td colspan="2">Load cell</td><td>6.0</td><td>0.06</td></tr>
<tr><td colspan="2">Plate</td><td>3.9</td><td>0.04</td></tr>
<tr><td colspan="2">Hinge</td><td>7.3</td><td>0.07</td></tr>
<tr><td rowspan="2">Cylinders (prop)</td><td>Top</td><td>2.0</td><td>0.02</td></tr>
<tr><td>Bottom</td><td>2.0</td><td>0.02</td></tr>
<tr><td colspan="2">$\boldsymbol{W_{eq}}$</td><td>146.3</td><td>1.44</td></tr>
</table>

### 4.2.1 Specimens TS2.5_16_0.33 (composite)

Firstly, Table 5 presented nominal dimensions and characteristics of prototypes investigated in this research. Before testing, samples were measured, which allowed for precise result analysis as well as for the calculation of concrete volume employed in each sample, summarized in Table 20 as follows.

**Table 20.** Sample dimensions – TS2.5_16_0.33.

| Parameter | TS2.5_16_0.33a | | TS2.5_16_0.33b | | TS2.5_16_0.33c | |
|---|---|---|---|---|---|---|
| | ***R1*** | ***R2*** | ***R1*** | ***R2*** | ***R1*** | ***R2*** |
| $L_T\ [cm]$ | 270.1 | 270.1 | 270.1 | 270.1 | 270.1 | 270.1 |
| $OH_L\ [cm]$ | 10.0 | 10.0 | 10.1 | 10.1 | 9.9 | 9.9 |
| $OH_R\ [cm]$ | 9.9 | 9.9 | 10.0 | 10.0 | 9.8 | 9.8 |
| $L\ [cm]$ | 250.3 | 250.3 | 250.1 | 250.10 | 250.4 | 250.4 |
| $B_p\ [cm]$ | 101.1 | | 101.0 | | 101.2 | |
| $b_b\ [cm]$ | 20.1 | 20.3 | 20.0 | 19.9 | 20.0 | 20.0 |
| $b_w\ [cm]$ | 9.8 | 10.0 | 9.6 | 9.5 | 9.5 | 9.5 |
| $h\ [cm]$ | 20.8 | 20.8 | 20.9 | 20.9 | 20.9 | 20.9 |
| $h_c\ [cm]$ | 5.1 | 5.1 | 5.0 | 5.0 | 5.3 | 5.3 |
| Shear span | 83.4 | | 83.3 | | 83.5 | |

Afterwards, all slab components were weighted as reported in Table 21. It's important to state that $G_{sp}$ was obtained from the overall slab weight divided by correspondent length.

**Table 21.** Dead loads from slab specimens – TS2.5_16_0.33.

| DESCRIPTION | VARIABLE | SPECIMEN | | |
|---|---|---|---|---|
| | | **a** | **b** | **c** |
| Concrete | $P_{conc}$ (kgf) | 524.53 | 511.75 | 526.52 |
| Cold-formed steel profile | $P_{s,left}$ (kgf) | 2.45 | 2.45 | 2.40 |
| | $P_{s,right}$ (kgf) | 2.45 | 2.45 | 2.45 |
| Light filling blocks (EPS) | $P_{EPS,left}$ (kgf) | 1.70 | 1.60 | 1.55 |
| | $P_{EPS,center}$ (kgf) | 3.35 | 3.30 | 2.80 |
| | $P_{EPS,right}$ (kgf) | 1.70 | 1.40 | 1.55 |
| Rebar trusses | $P_{rt,left}$ (kgf) | 3.15 | 3.15 | 3.20 |
| | $P_{rt,right}$ (kgf) | 3.20 | 3.20 | 3.20 |
| Wire mesh | $P_{wm}$ (kgf) | 2.50 | 2.50 | 2.55 |
| Connectors | $P_{connector}$ (kgf) | 0.16 | 0.16 | 0.16 |
| TOTAL | $P_{T,slab}\ (kgf)$ | 545.19 | 531.96 | 546.39 |
| | $G_{sp}\ (kN/m)$ | 1.98 | 1.93 | 1.98 |

In accordance with Figure 50, test "a" was monotonically performed with constant load increments until complete failure of specimen, when the load reached $95.7\ kN$ (including dead loads from test apparatus and slab) with correspondent displacement of $35.4\ mm$, the equivalent to $L/71$. As such, since maximum displacement in failure is less than $L/50$, collapse loads is taken as $95.7\ kN$ according to the EN 1994-1-1 (CEN, 2004).

In case of specimens “b” (Figure 51) and “c” (Figure 52), on the other hand, load cycles corresponding to $30\%$, $37.5\%$ and $45\%$ of $95.7\ kN$ (respectively $29.3\ kN$, $36.6\ kN$ and $43.9\ kN$) were introduced on test execution. As such, ultimate loads have reached $83.6\ kN$ and $86.8\ kN$ corresponding to samples “b” and “c”, respectively, which represent, on average, $11\%$ less than previous test. Note that maximum loads were reached with $28.2\ mm$ and $31.4\ mm$, respectively, corresponding to $L/89$ and $L/80$, lower than the $L/50$ limit imposed by the EN 1994-1-1 (CEN, 2004). Note samples “a”, “b” and “c” showed great accordance in terms of collapse load, with mean value of $88.8\ kN$ and variation coefficient equal to 7.0%. Largest dispersion happened between sample “a” and mean value, which is equal to 8.0%.

Moreover, the difference in recordings provided by LVDT1 and LVDT2 for specimens “a”, “b” and “c” was kept under $1\ mm$ until collapse, granting cohesion to analysis. Besides, it also indicates that load was balanced, being applied in the longitudinal centerline of prototypes, which avoided distortion in samples during loading. It’s important to state that the average value of support displacements (LVDT3 and LVDT4 according to Figure 38) was already deducted from LVDT1 and LVDT2 measurements.

Regarding the end-slips between steel and concrete ($\Delta$), Figure 50b and Figure 52b show that the magnitude of displacements is comprised between $0$ and $0.08\ mm$ until collapse. Nevertheless, the employed LVDT’s have a stroke of $150\ mm$ with accuracy in measuring of $\pm 0.05\%$. Therefore, since it corresponds to $0.075\ mm$, it confirms the idea that acquired data are below the precision of equipment, not indicating relative displacements between steel and concrete. As such, the information extracted from graphics must be interpreted as null displacements owing to full interaction between materials.

However, Figure 51b is incoherent with sample results “a”, “c” and Candido’s (2021). This fact was reinforced after visual inspection of bottom ribs at edge of slabs, which did not exhibit separation between structural materials after failure. It strongly evidences the hypothesis that longitudinal shear is not a critical limit state in design of such slabs.

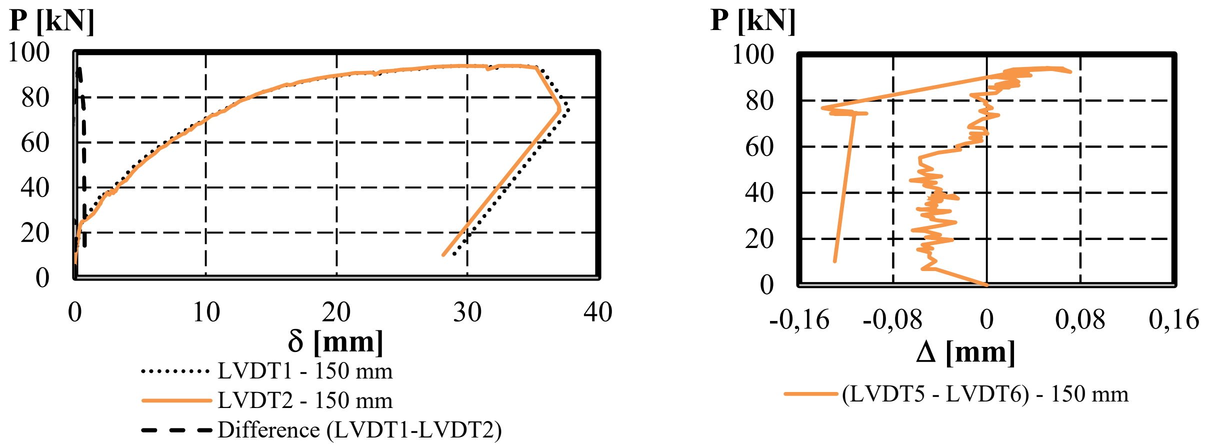


(a) (b)

**Figure 50.** TS2.5_16_0.33a testing result: (a) load displacement; (b) load slip.
Source: Author.

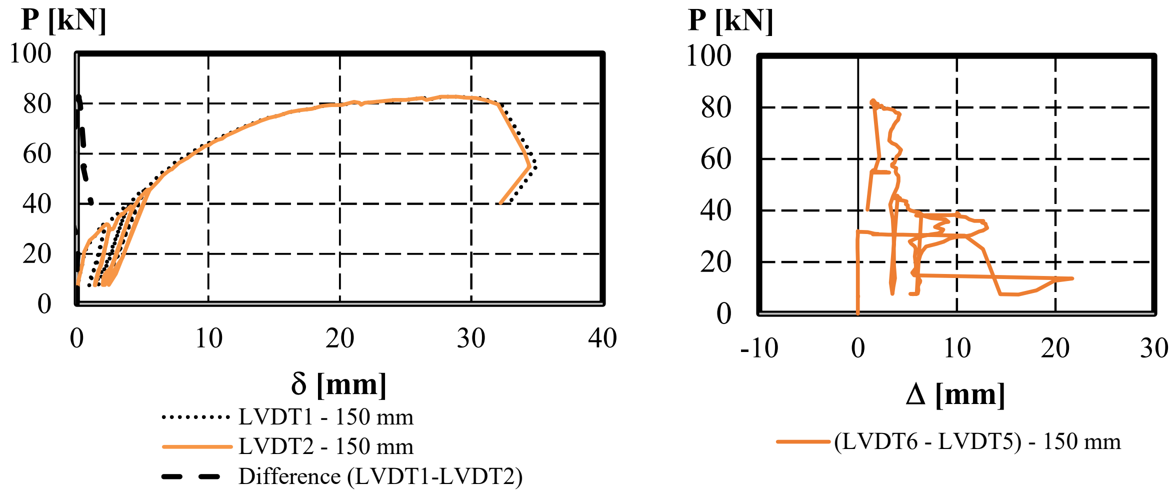


(a) (b)

**Figure 51.** TS2.5_16_0.33b testing result: (a) load displacement; (b) load slip.
Source: Author.

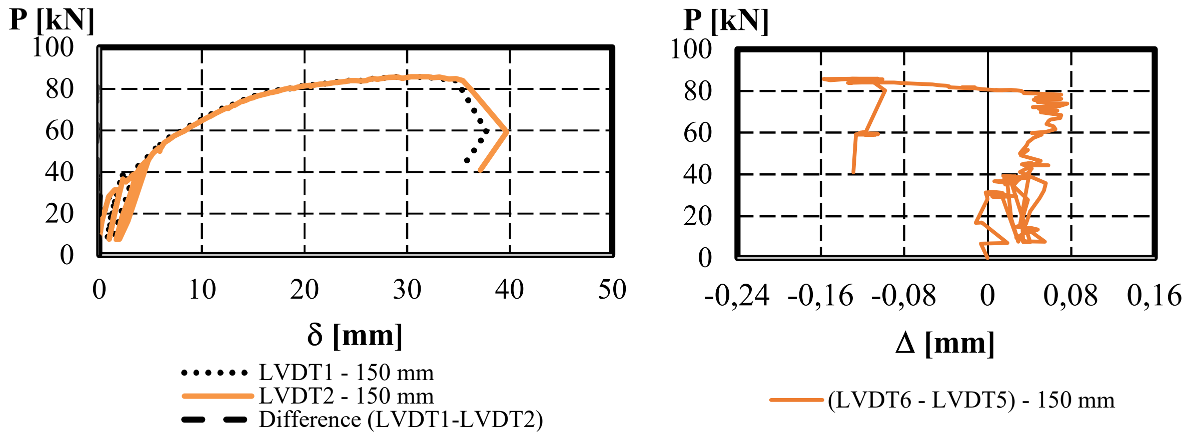


(a) (b)

**Figure 52.** TS2.5_16_0.33c testing result: (a) load displacement; (b) load slip.
Source: Author.

Moreover, to define the failure mechanism of the three slab specimens in this particular case, it’s important to pay special attention to data acquired from strain gauges. Figure 53 shows the crack opened in the ribs of slab at the end of test and its position measured from the sample edge, comprised between shear spans – where the maximum bending moment actually occurs (crack widths of 9 $mm$, 5 $mm$ and 3 $mm$, respectively, for “a”, “b” and “c”).

According to Figure 54, absolute values of strains in concrete were always less than $\varepsilon_{cu} = 3500\ \mu$, indicating that concrete did not undergo crushing in addition to visual inspection of surfaces. As such, prototypes failed due to yielding of shuttering and, as a consequence, excessive cracks in concrete matrix. Note that the strain correspondent to yielding start it $\varepsilon_y = f_{yF}/E = 299.1/200000 = 1495.5\ \mu$ and all positive strain values in Figure 54 are greater it.

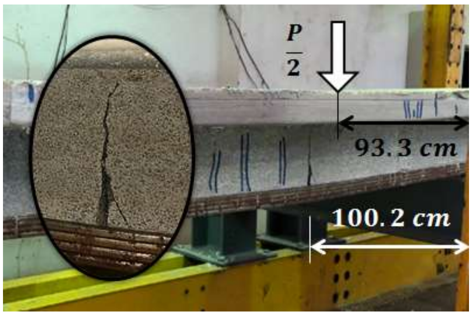


(a) Specimen TS2.5_16_0.33a.

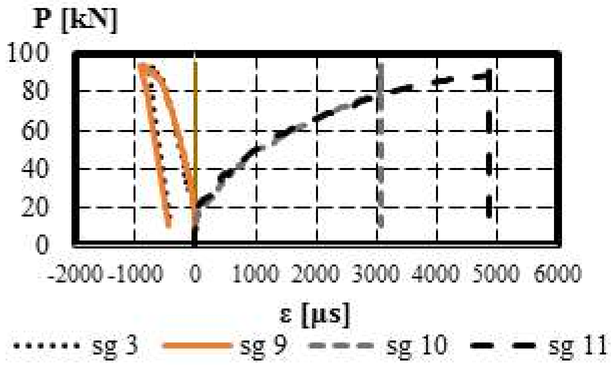


(a) Specimen TS2.5_16_0.33a.

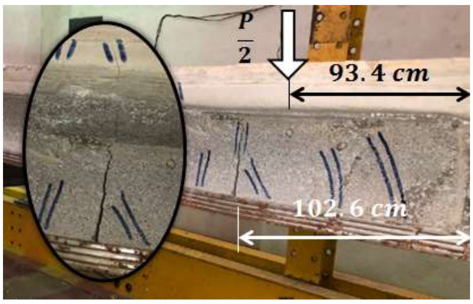


(b) Specimen TS2.5_16_0.33b.

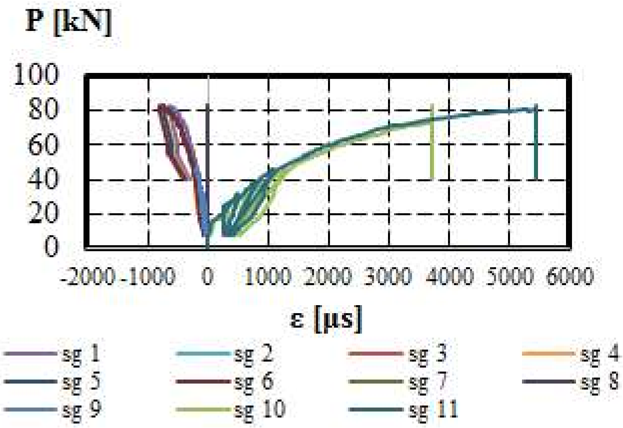


(b) Specimen TS2.5_16_0.33b.

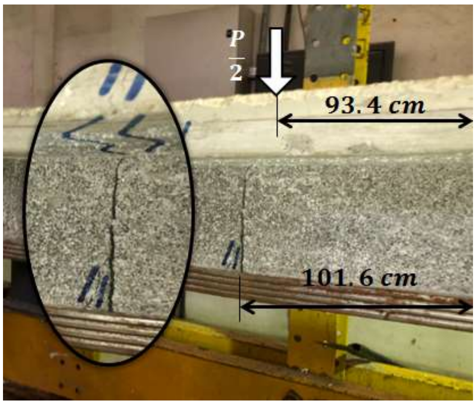


(c) Specimen TS2.5_16_0.33c.
**Figure 53.** Failure patterns of composite slab system – TS2.5_16_0.33.
Source: Author.

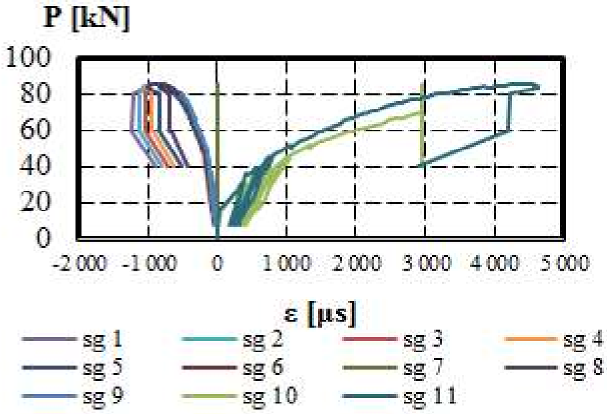


(c) Specimen TS2.5_16_0.33c.
**Figure 54.** Strains in concrete slab and CFS section.
Source: Author.

Finally, test results were used to calibrate the analytical models presented in section 3.3.1. According to Figure 55, both models MR1 and MR2 showed great accordance to samples "b" and "c", assessed with cyclic load. Note that ratios between predicted and measured values are close to unit – 0.98 and 0.94, respectively. Besides, compressive strengths arisen from wet and chemical curing processes led to almost same results – the variation of 6.7% in $f_c$ did not impact the characteristic bending resistance, producing insignificant deviations when compared to each other. Finally, note that MR1 and MR2 are equally appropriate to predict the bending resistance of such slabs.

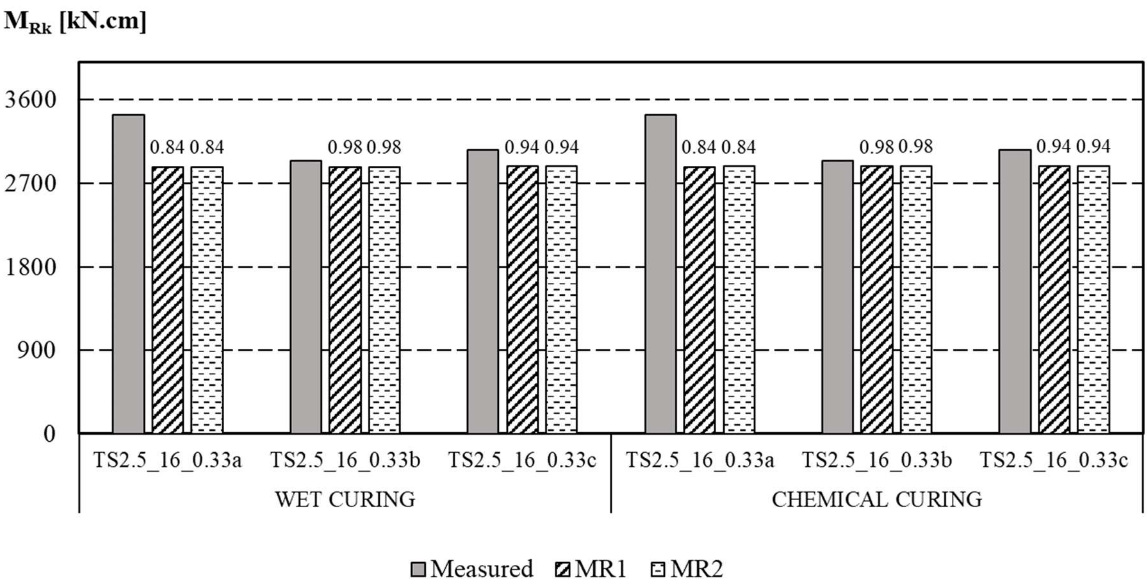


**Figure 55.** Comparison between TS2.5_16_0.33 results and analytical predictions.
Source: Author.

### 4.2.2 Specimens RCS2.5_16_0.33 (non-composite)

Firstly, samples were measured, which allowed for precise result analysis as well as for the calculation of specimens dead loads, summarized in Table 22 as follows.

**Table 22.** Sample dimensions – RCS2.5_16_0.33.

| Parameter | RCS2.5_16_0.33a | | RCS2.5_16_0.33b | | RCS2.5_16_0.33c | |
|---|---|---|---|---|---|---|
| | ***R1*** | ***R2*** | ***R1*** | ***R2*** | ***R1*** | ***R2*** |
| $L_T\ [cm]$ | 270.0 | 270.0 | 270.0 | 270.0 | 269.8 | 269.8 |
| $OH_L\ [cm]$ | 9.5 | 9.5 | 10.4 | 10.4 | 10.0 | 10.0 |
| $OH_R\ [cm]$ | 10.0 | 10.0 | 10.3 | 10.3 | 9.9 | 9.9 |
| $L\ [cm]$ | 250.5 | 250.5 | 249.4 | 249.4 | 249.9 | 249.9 |
| $B_p\ [cm]$ | 100.5 | | | | 100.5 | |
| $b_b\ [cm]$ | 19.5 | 19.5 | 19.5 | 19.5 | 19.5 | 19.5 |
| $b_w\ [cm]$ | 9.5 | 9.5 | 9.5 | 9.5 | 9.5 | 10.0 |
| $h\ [cm]$ | 20.5 | 20.5 | 20.5 | 20.5 | 20.6 | 20.6 |
| $h_c\ [cm]$ | 4.8 | 4.8 | 4.9 | 4.9 | 5.2 | 5.2 |
| Shear span | 83.6 | | | | 83.6 | |

Afterwards, all slab components were weighted as reported in Table 23. It's important to state that $G_{sp}$ was obtained from the overall slab weight divided by correspondent length.

**Table 23.** Dead loads from slab specimens – RCS2.5_16_0.33.

| DESCRIPTION | VARIABLE | SPECIMEN | | |
|---|---|---|---|---|
| | | **a** | **b** | **c** |
| Concrete | $P_{conc}$ (kgf) | 461.17 | 466.38 | 485.14 |
| Cold-formed steel profile | $P_{s,left}$ (kgf) | 0.00 | 0.00 | 0.00 |
| | $P_{s,right}$ (kgf) | 0.00 | 0.00 | 0.00 |
| Light filling blocks (EPS) | $P_{EPS,left}$ (kgf) | 1.55 | 1.70 | 1.55 |
| | $P_{EPS,center}$ (kgf) | 3.05 | 3.45 | 3.40 |
| | $P_{EPS,right}$ (kgf) | 1.50 | 1.60 | 1.65 |
| Rebar trusses | $P_{rt,left}$ (kgf) | 3.10 | 3.15 | 3.15 |
| | $P_{rt,right}$ (kgf) | 3.15 | 3.15 | 3.15 |
| Wire mesh | $P_{wm}$ (kgf) | 2.50 | 2.45 | 2.50 |
| Connectors | $P_{connector}$ (kgf) | 0.69 | 0.69 | 0.69 |
| TOTAL | $P_{T,slab}\ (kgf)$ | 476.71 | 482.56 | 501.22 |
| | $G_{sp}\ (kN/m)$ | 1.73 | 1.75 | 1.82 |

In this case, sample "a" was performed with constant load increments until complete failure of specimen, when load reached 42.8 $kN$, including dead loads arisen from apparatus and slab, showing a displacement of 17.5 $mm$, the equivalent to $L/143$ according to Figure 56. Hence, since maximum displacement in failure is less than $L/50$, collapse loads is taken as 42.8 $kN$ according to the EN 1994-1-1 (CEN, 2004).

In case of specimens "b" (Figure 57) and "c" (Figure 58), on the other hand, load cycles corresponding to 30%, 37.5% and 45% of 42.8 $kN$ (respectively 12.8 $kN$, 16.1 $kN$ and 19.3 $kN$) were introduced on testing. As such, ultimate loads have reached 29.6 $kN$ and 29.4 $kN$ corresponding to samples "b" and "c", respectively, which represent, on average, 31% less than previous test. Besides, composite tests were found to be more accurate by the deviation of 11% against 31% in this case. Note that maximum loads were reached with 18.3 $mm$ and 15.0 $mm$, respectively, corresponding to $L/137$ and $L/167$, lower than the $L/50$ limit imposed by the EN 1994-1-1 (CEN, 2004). Note samples "a", "b" and "c" did not show great accordance as TR2.5_16_0.33 in terms of collapse load, with mean value of 33.9 $kN$ and variation coefficient equal to 22.6%. Largest dispersion happened between sample "a" and mean value, which is equal to 26.1%.

Finally, as addressed to TS2.5_16_0.33 group, the difference in recordings provided by LVDT1 and LVDT2 for specimens "a", "b" and "c" was kept under 1 $mm$ until collapse, conferring cohesion to analysis. It's important to state that the average value of support displacements (LVDT3 and LVDT4 according to Figure 38) was already deducted from LVDT1 and LVDT2 measurements.

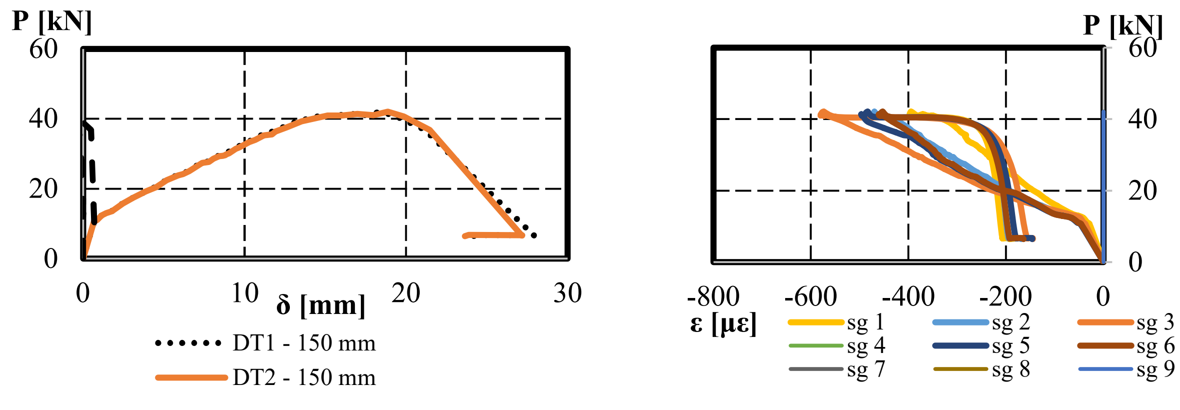


(a) (b)

**Figure 56.** RCS2.5_16_0.33a testing result: (a) load displacement; (b) strains at concrete top flange.

Source: Author.

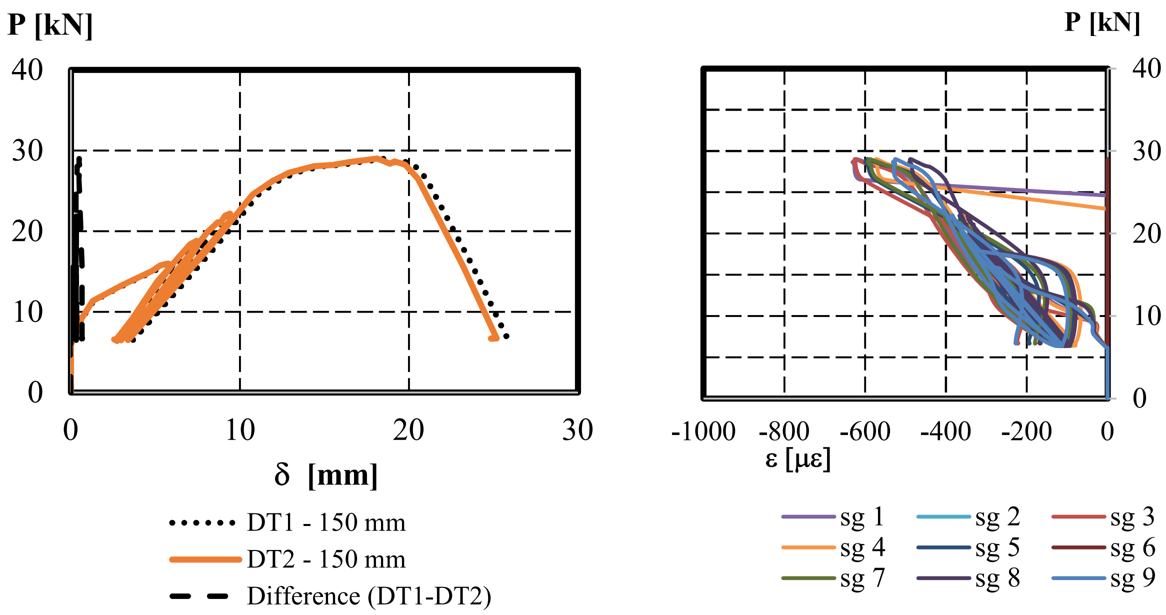


(a) (b)

**Figure 57.** RCS2.5_16_0.33b testing result: (a) load displacement; (b) strains at concrete top flange.
Source: Author.

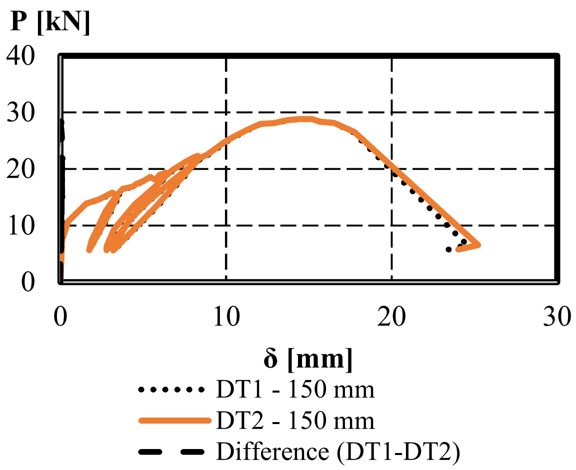


**Figure 58.** RCS2.5_16_0.33a testing result: load displacement.
Source: Author.

It's important to state that all reinforced concrete specimens have failed in a ductile manner, with the neutral axis located few centimeters in the top flange and showing yielding of tensile reinforcements. This fact can be easily noticed through the shape of the load-displacement curves with downward curvatures: in the moment when the collapse was reached, the load decreased to more than 50% of initial values.

Besides, first cracks in concrete appeared in the bottom ribs with low stage of loads (around 20%) followed by progressive propagation into concrete matrix. At failure moment, a deep crack extended from top flange to bottom rib appeared in each slab close to the load introduction point, within the length comprised between them (pure flexure), as shown in Figure 59.

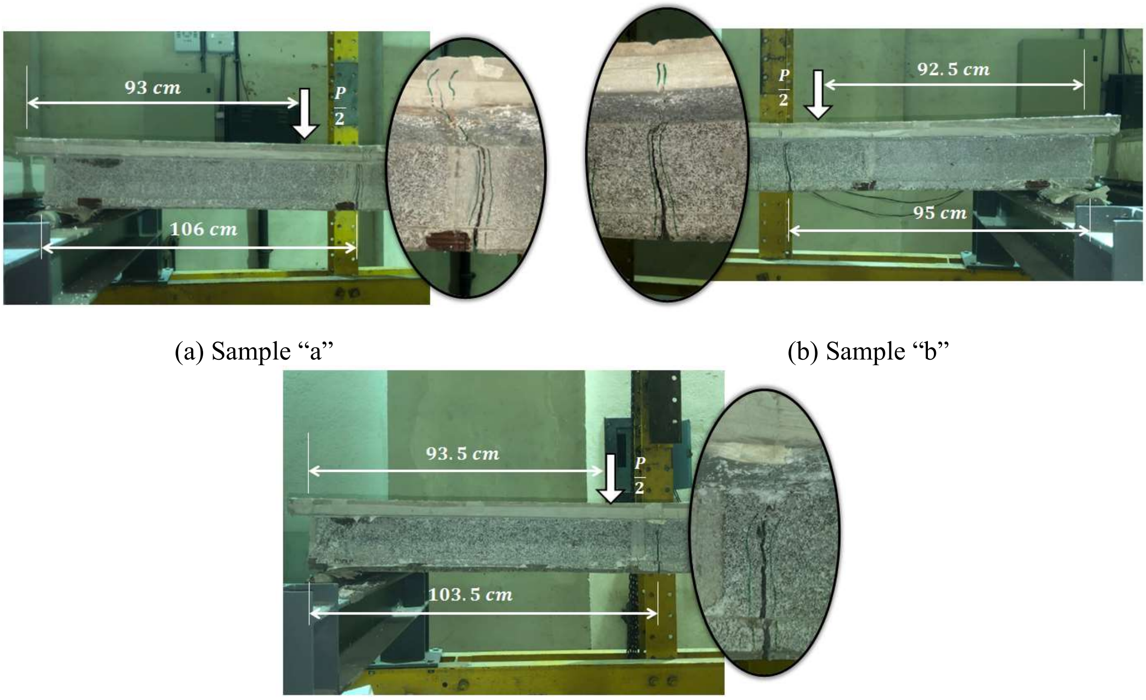


(a) Sample "a"

(b) Sample "b"

(c) Sample "c"

**Figure 59.** Failure patterns of composite slab system – RCS2.5_16_0.33.
Source: Author.

Finally, results served as basis to calibrate the analytical model presented in section 3.3.1.1 to concrete design (MR1). According to Figure 60, despite being a well-known procedure, it led to non-convergent outcomes since the ratio between predicted and measured values were 0.79 to specimen "a" (i.e., 21% lower) and 1.20 to samples "b" and "c" on average (i.e., 20% grater) and in case of wet curing. Besides, the curing process did not impact significantly on results as proved by the 1% difference between correspondent values. Nevertheless, since both samples "b" and "c" tested under cyclic loads led to same resistance, results are interpreted as consistent.

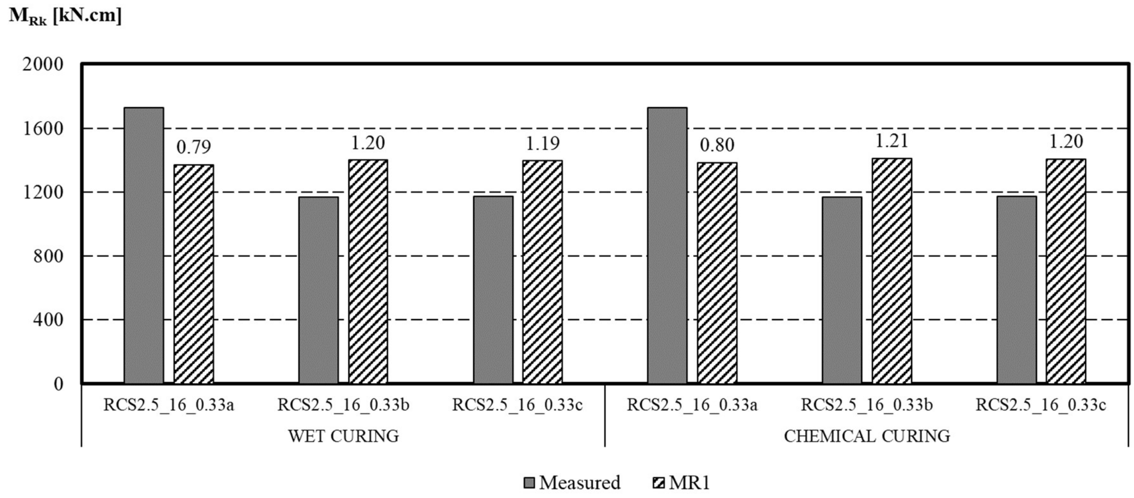


**Figure 60.** Comparison between RCS2.5_16_0.33 results and analytical predictions.
Source: Author.

### 4.2.3 Comparison

Test results in terms of load capacity are summarized in Table 24, which also includes data from Candido (2021). Firstly, according to last column, all peak loads were reached with correspondent displacement lower than $L/50$, so they are considered as ultimate load. Besides, the ratio between testing and plastification bending moments calculated by model MR1 (more accurate than MR2) are quite precise to all composite samples, with larger deviation in case of monotonic tests. Since no edge slips were identified by LVDT recordings and visual inspection, the cold-formed steel section is fully incorporated to the concrete slab, playing an important role to its resistance.

**Table 24.** Summary of test results.

| Group | Sample | L [mm] | $L_s$ [mm] | $P_{(0.1\ mm)}$ [kN] | $P_{max}$ [kN] | Load application | $M_u$ [kN.cm] | $M_{pl}$ [kN.cm] | $M_u/M_{pl}$ | $\delta_{max}$ [mm] | |
|---|---|---|---|---|---|---|---|---|---|---|---|
| TS2.5_16_0.25 (Candido, 2021) | a | 2500 | 625 | 120.07 | 120.7 | Monotonic | 3770.6 | 3471.9 | 1.09 | 30.2 | L/83 |
| | b | 2500 | 625 | -- | 112.3 | Cyclic | 3507.9 | 3460.9 | 1.01 | 33.6 | L/74 |
| | c | 2500 | 625 | -- | 113.8 | Cyclic | 3555.8 | 3487.8 | 1.02 | 27.9 | L/90 |
| TS2.5_16_0.33 | a | 2500 | 833 | -- | 95.7 | Monotonic | 3435.2 | 2876.8 | 1.19 | 35.4 | L/71 |
| | b | 2500 | 833 | -- | 83.8 | Cyclic | 2945.8 | 2880.6 | 1.02 | 28.2 | L/89 |
| | c | 2500 | 833 | -- | 86.8 | Cyclic | 3061.1 | 2884.6 | 1.06 | 31.4 | L/80 |
| RCS2.5_16_0.33 | a | 2500 | -- | -- | 42.8 | Monotonic | 1727.4 | 1371.9 | 1.26 | 17.5 | L/143 |
| | b | 2500 | -- | -- | 29.6 | Cyclic | 1168.0 | 1399.4 | 0.83 | 18.3 | L/137 |
| | c | 2500 | -- | -- | 29.4 | Cyclic | 1174.6 | 1394.7 | 0.84 | 15.0 | L/167 |

It's important to mention that the full interaction between steel and concrete can be attributed to frictional interlocking since embossments in the CFS profile are small and oriented outside the shuttering as shown in Figure 61, which is not effective to transfer shear. This subject, however, must be deeply investigated to better understand how forces are precisely transferred.

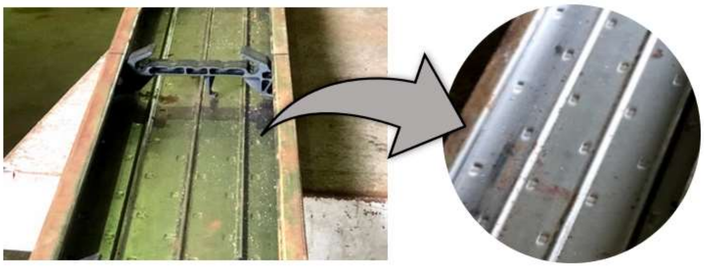

**Figure 61.** Embossments in the CFS.
Source: Author.

Plotting results from composite and non-composite tests into a same graphic as depicted in Figure 62, the contribution of the CFS lipped channel section in strength of slab system is clearly evidenced despite its reduced cross-sectional area $(1.24\ cm^2)$ and the gross moment of inertia $(1.94\ cm^4)$. Regarding the cyclic tests, the maximum average load of $29.5\ kN$ from tests RCS2.5_16_0.33b and RCS2.5_16_0.33c has soared to $85.3\ kN$ of TS2.5_16_0.33b and TS2.5_16_0.33c samples, representing almost three times the baseline value – 189% more to be precise.

In addition, observe that the inclusion of the CFS section has enhanced the stiffness to the slab, which can be attributed to the increase in the cracked moment of inertia owing to the $\alpha_{E,rt}\left[I_{G,rt}+A_{rt}\left(h-h_0-y_{G,rt}-y_{II}\right)^2\right]$ parcel in Eq. (82). Whereas $\alpha_{E,rt}I_{G,rt}$ is small when compared to $I_{cf}$, the part $\alpha_{E,rt}A_{rt}\left(h-h_0-y_{G,rt}-y_{II}\right)^2$ corresponding to the main axis shift from the CFS center of gravity to concrete top flange plays an important role in granting flexural rigidity to the composite system.

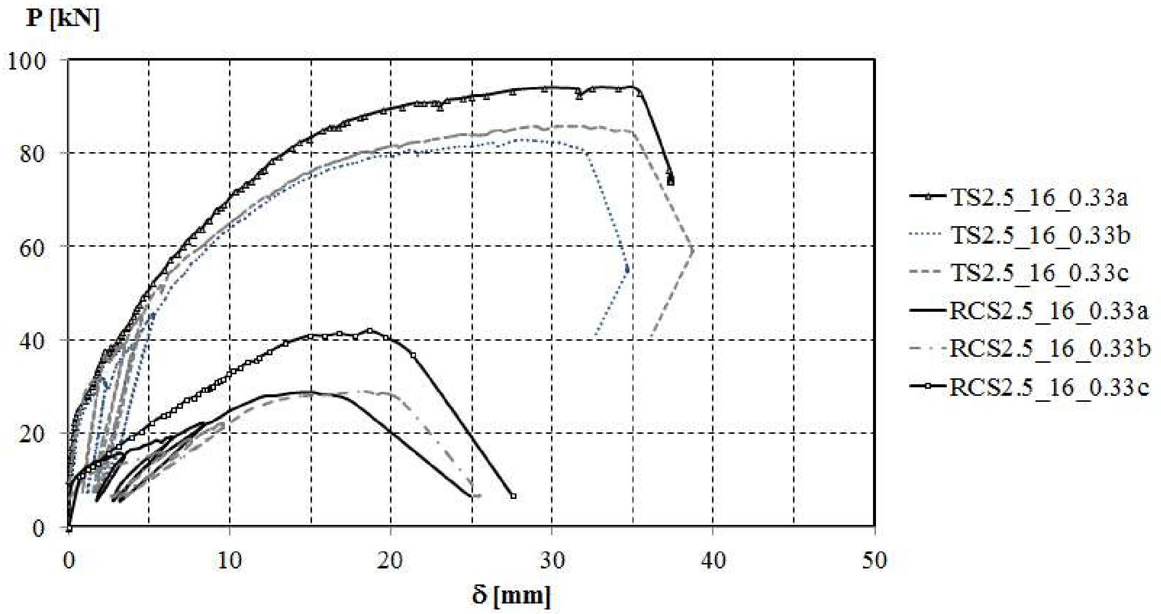


**Figure 62.** Comparison between TS2.5_16_0.33 and RCS2.5_16_0.33 outcomes.
Source: Author.

From an alternative perspective, the composite specimens have exibhited greater midpsan displacements at peak load than non-composite ones (1.79 times), which is a good first indicator of the increase in structure ductility. According to Hossain *et al.* (2016), it is the ability of a member to undergo inelastic displacements without excessive reducing in strength, properly calculated based on the energy approach as the area under the load-displacement curve until 80% of peak-load as exemplified in Figure 63 for sample TS2.5_16_0.33a. The area calculated by direct integration of load-displacement curve is firstly expressed in $kN.mm$ and converted to $N.m$ or $J$ (joule). It's important to state that load cycles are supressed from this analysis.

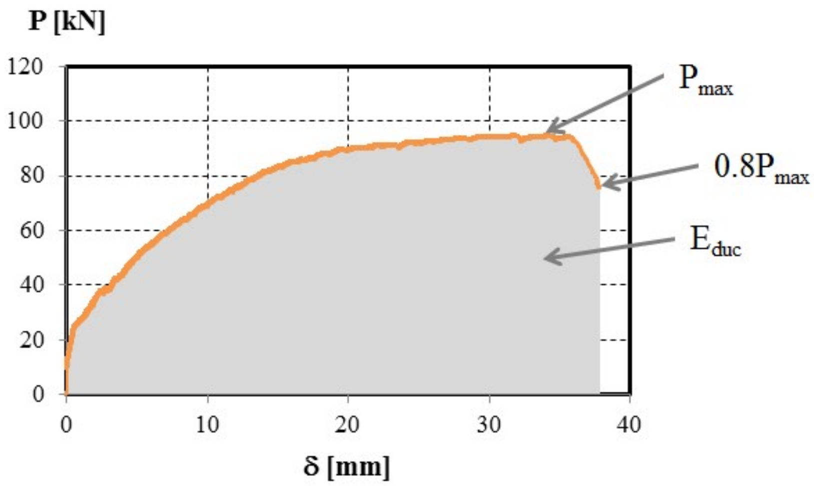


**Figure 63.** Calculation of ductility indicator of TS2.5_16_0.33a.
Source: Author.

According to Table 25, the energy absorted by composite samples is, in general, 5 times higher then non-composite ones, which can be attributed to ductile behavior of steel from cold-formed section in terms of strain capacity and cracking control in concrete. Candido's (2021) results were suppressed here because they were obtained with a different shear span.

**Table 25.** Ductility based on energy of composite and non-composite samples tested in this research.

| Group | Sample | L [mm] | $L_s$ [mm] | Load application | $E_{duc}$ [J] |
|---|---|---|---|---|---|
| TS2.5_16_0.33 | a | 2500 | 833 | Monotonic | 5853 |
| | b | 2500 | 833 | Cyclic | 4596 |
| | c | 2500 | 833 | Cyclic | 5341 |
| RCS2.5_16_0.33 | a | 2500 | -- | Monotonic | 1343 |
| | b | 2500 | -- | Cyclic | 943 |
| | c | 2500 | -- | Cyclic | 847 |

To conclude this discussion in terms of bending capacity, the analytical model MR1 presented in section 3.3 will be used to determined the flexural characteritic resistance of two identical slab systems that differ from one to another on the presence of CFS shuttering. While the the cross section dimensions are reported in Figure 64, the following material properties shall be considered:

a) Concrete compressive strenght: $f_c = 30\ MPa$;
b) CFS section:
    a. Yield strength: $f_{yF} = 280\ MPa$;
    b. Thickness: $t = 0.5\ mm$;
    c. Area: $A_{cfs} = 1.17\ cm^2$;
    d. Centroid position from bottom: $y_{cfs} = 1.06\ cm$;
c) Rebar truss model TB-16M:
    a. Height: $h_{rt} = 160\ mm$;
    b. Upper chord diameter: $\emptyset_s = 7\ mm$;
    c. Diagonal diameter: $\emptyset_d = 4.2\ mm$;
    d. Lower chord diameter: $\emptyset_i = 6\ mm$;
    e. Yield strength: $f_{yrt} = 600\ MPa$;

d) Wire mesh model Q75:

a. Reinforcement area: $A_{s,wm} = 0.75\ cm^2/m$;

b. Yield strength: $f_{ywm} = 600\ MPa$;

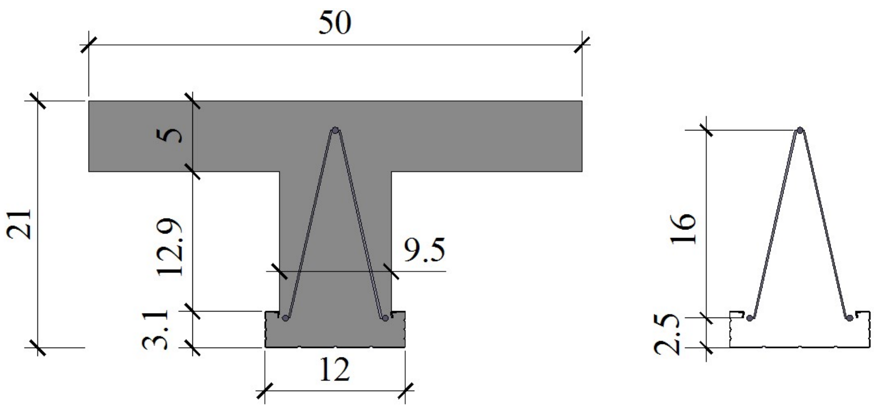


**Figure 64.** Cross-section of a slab system cast with rebar truss TB-16M.
Source: Author.

In this context, the characteristic bending resistance is increased in 88% when the CFS shuttering is introduced at the bottom rib, raising its value from $716\ kN.cm/rib$ to $1351\ kN.cm/rib$. Finally, since the CFS section unitary dead load is $0.92\ kg/m$, the resistance-to-weight ratio of this profile in the slab is around $7\ kN.m^2/kg$.

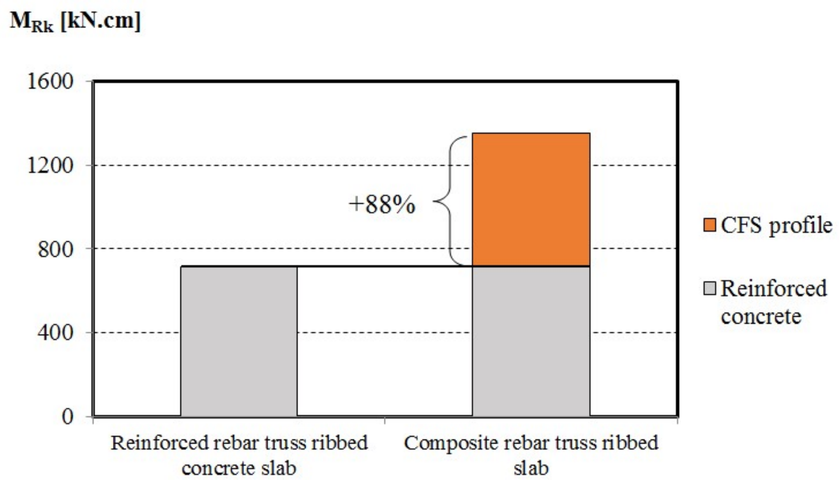


**Figure 65.** Increase in bending resistance due to incorporation of CFS shuttering in the slab bottom rib.
Source: Author.

## 4.3 LOAD-DISPLACEMENT RESPONSE OF COMPOSITE SAMPLES

The last stage of this research is dedicated to assess the suitability of models presented in Table 2 to calculate the effective moment of inertia of the composite, comparing it to experimental data from group TS2.5_16_0.33 as well as to TS2.5_16_0.25 (Candido, 2021). In both cases, the isostatic span corresponds to $L = 2500\,mm$ and, therefore, the displacement limit in serviceability is $L/350 = 2500/350 = 7.15\,mm$. Furthermore, it's important to state that load increments in all equations correspond to average value provided by the hydraulic actuator during test, taken as $40\,N$ from one point to another.

### 4.3.1 Samples TS2.5_16_0.33

In this case, the loads are introduced $L_s = 833.3\,mm$ from supports. If $F_{act}$ denotes the force introduced exclusively by the hydraulic actuator as shown in Figure 24, the midspan deflection $\delta$ for a simply supported beam must be calculated according to Eq. (83), where $E_{cs}$ is the concrete secant modulus of elasticity.

$$\delta = \frac{F_{act} L_s}{48 E_{cs} I_{eff}} (3L^2 - 4L_s^2) \qquad \text{Eq. (83)}$$

Afterwards, Figure 66, Figure 67 and Figure 68 represent the load-displacement curves of samples "a", "b" and "c", respectively, considering only the external applied force, from which the support displacements were previously deducted. In all cases, the model proposed by Souza-Neto (2001) best estimated the displacements closer to serviceability limit in a conservative way. Actually, that's expected because the rebar truss ribbed slab analyzed in this research is mainly composed by concrete and M3 adjusted Branson's (1963) equation to reduce the cracking influence on $I_{eff}$ due to the CFS shuttering.

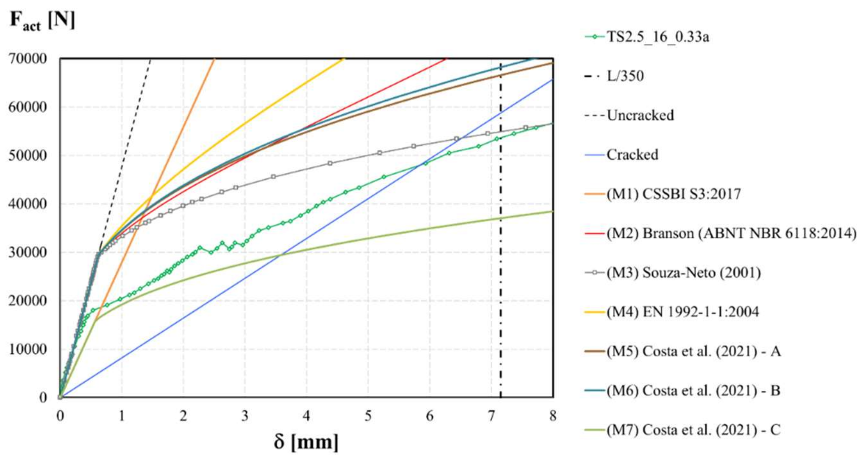


**Figure 66.** Load-displacement response: measured x predicted values – TS2.5_16_0.33a.
Source: Author.

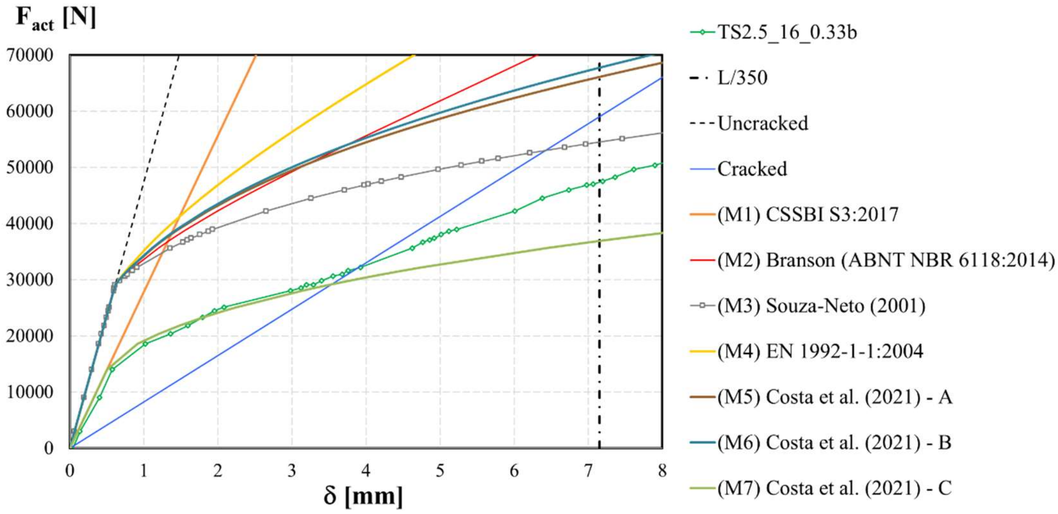


**Figure 67.** Load-displacement response: measured x predicted values – TS2.5_16_0.33b.
Source: Author.

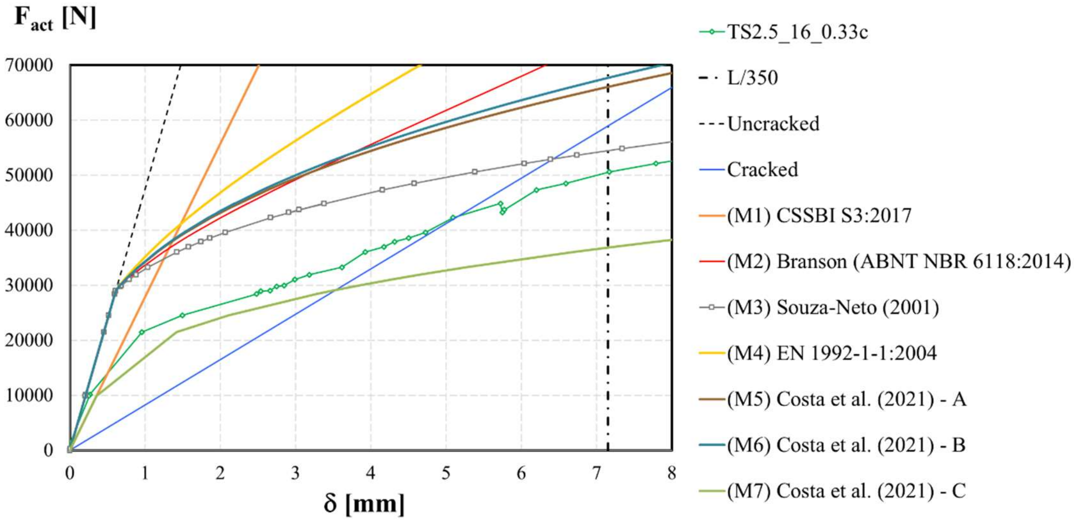


**Figure 68.** Load-displacement response: measured x predicted values – TS2.5_16_0.33c.
Source: Author.

In addition, Figure 69a shows the measured against predicted values of displacements obtained with model M3, the one that best approximated maximum displacements closer to serviceability limit. In the preliminary load steps, between 2 $mm$ and 6 $mm$, note that none of tested equations conducted to precise results, being M3 the most suitable one. Nonetheless, the criterion based on cracked moment of inertia is also precise, conservative and it is easier to apply through hand calculation (Figure 69b).

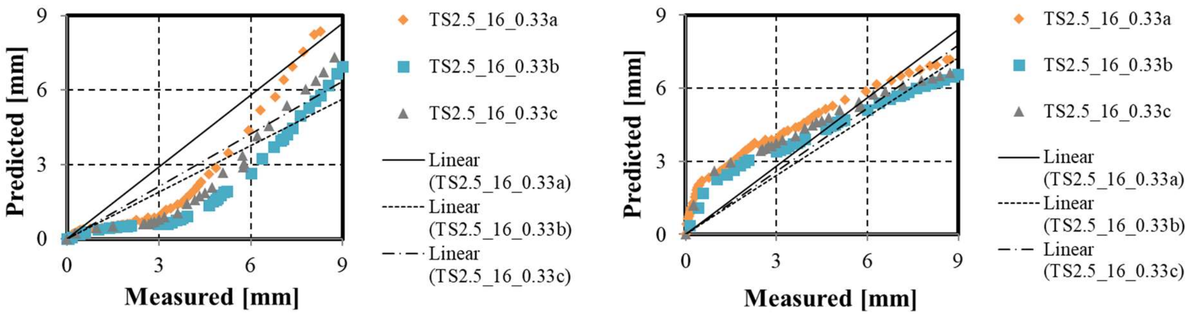


(a) Model M3 (b) Cracked moment of inertia $(I_{eff} = I_{II})$

**Figure 69.** Data fitting between measured and predicted values – TS2.5_16_0.33 group.
Source: Author.

### 4.3.2 Samples TS2.5_16_0.25

Now, loads are introduced $L_s = 625.0\ mm$ from supports. $F_{act}$ denotes the force introduced exclusively by the hydraulic actuator as shown in Figure 24 and midspan deflection $\delta$ are calculated according to Eq. (83), where $E_{cs}$ is the concrete secant modulus of elasticity.

As such, Figure 70, Figure 71 and Figure 72 represent the load-displacement response of samples "a", "b" and "c", respectively, considering only the external applied force, from which the support displacements were previously deducted.. In all cases, the M7 model presented by Costa *et al*. (2021) best estimated the displacements closer to serviceability limit in a conservative way, except for specimen "c" , which behavior differs from TS2.5_16_0.33 group. Besides, the adoption on cracked moment of inertia, a common practice among structural engineers to calculate displacements into composite slabs, well represented the experimental curve until $L/350$ in this case.

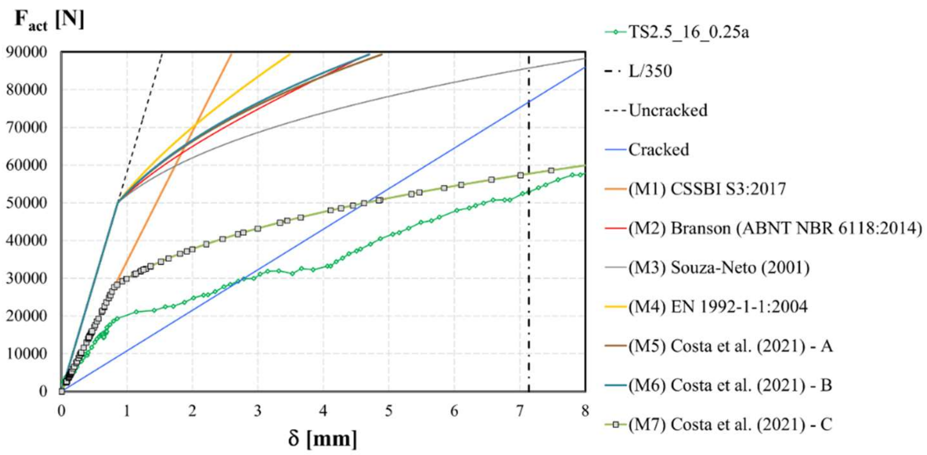


**Figure 70.** Load-displacement response: measured x predicted values – TS2.5_16_0.25a.
Source: Author.

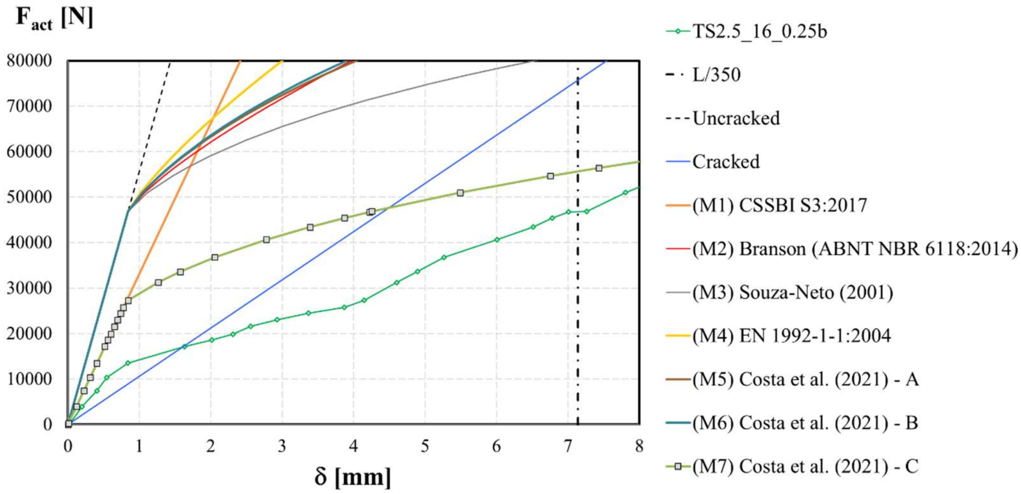


**Figure 71.** Load-displacement response: measured x predicted values – TS2.5_16_0.25b.
Source: Author.

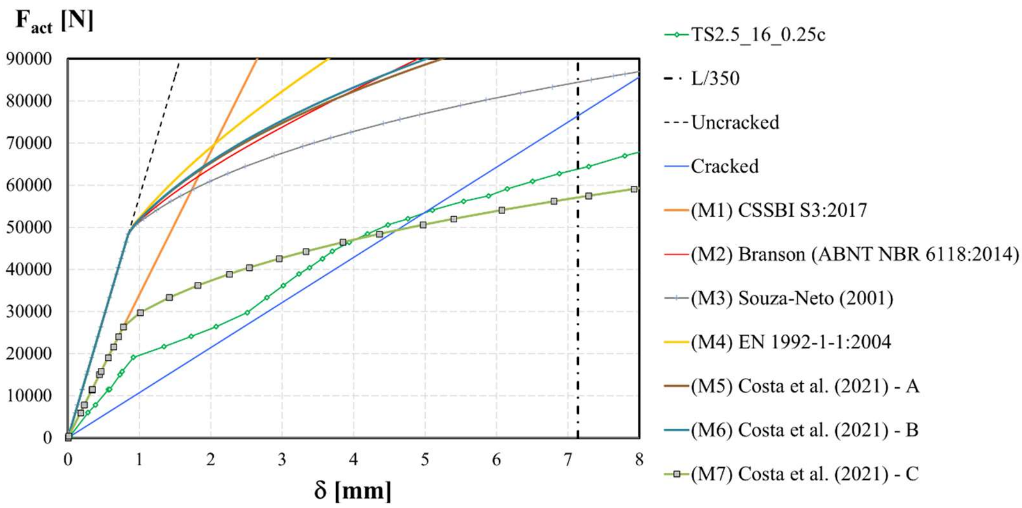


**Figure 72.** Load-displacement response: measured x predicted values – TS2.5_16_0.25c.
Source: Author.

In addition, Figure 73 shows the measured against predicted values of displacements obtained with model M7 and calculated with $I_{eff} = I_{II}$. In the preliminary load steps, between $2\ mm$ and $6\ mm$, note that the cracked moment of inertia has led to more accurate and conservative results than M7.

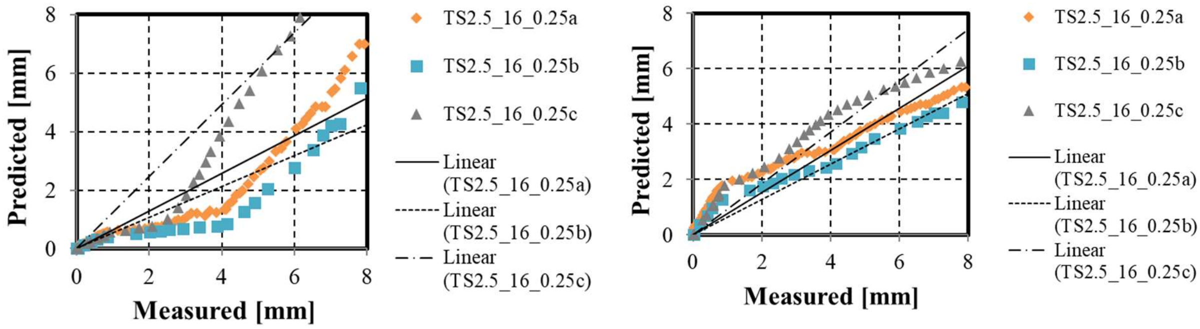


(a) Model M7 (b) Cracked moment of inertia $(I_{eff} = I_{II})$

**Figure 73.** Data fitting between measured and predicted values – TS2.5_16_0.25 group.
Source: Author.

### 4.3.3 Comparison

According to Figure 66 to Figure 73, displacements in serviceability of all specimens can be conservatively calculated by elastic analysis taking into account the cracked moment of inertia of cross section, which is the easiest and most simple alternative to hand calculation.

# 5

# FINAL REMARKS

## 5.1 CONCLUSIONS

This research has investigated the mechanical behavior of a new composite slab system composed by CFS lipped channel sections in minor bending fastened to rebar trusses through uniformly distributed plastic connectors, intended as an optimized alternative to the traditional reinforced ribbed slab with pre-cast concrete in the ribs. Distinctly from the steel decks, the intermittent shuttering is interposed with light filling blocks usually made in Expanded Polystyrene, reducing the slab dead load. Moreover, additional rebar can be placed into ribs to increase the structure sagging flexural capacity when needed due to project requirements.

In general, this system aims to replace pre-cast reinforced concrete ribbed slabs into constructions, offering as benefits the safety and ergonomics during assemblage on account of 80% reduction in rib dead load. Nevertheless, in terms of productivity, this system claims for additional labor hours due to installation of light filling blocks among ribs as well as propping before concrete casting.

Until now, no data was available in the specialized literature regarding the composite behavior of any system as this one. Furthermore, on account of absence of experimental tests on the aforementioned slab system, the CFS lipped channel section was used exclusively as shuttering during concrete casting and, thus, fabricated with non-structural steel. Notwithstanding, even though Candido (2021) tested the slab system with shear span taken as 25% of isostatic span, these results are insufficient to reach strong conclusions on its shear behavior. In passing by, the EN 1994-1-1 (CEN, 2004) required at least six specimen to outline the $m - k$ curve, which is used as a design equation to calculate the longitudinal shear resistance.

As such, six novel slab samples were cast and tested to better understand the mechanical behavior of aforementioned slab in sagging bending, being half of them composite, analyzed with a different shear span than Candido (2021), and the other half non-composite, made with reinforced concrete only. Finally, the following conclusions can be drawn:

a) All composite specimens from TS2.5_16_0.33 group ($L_S/L = 1/3$) have undergone failure due to plastification of a cross-section comprised between the line loads, i.e., in the pure bending region. Furthermore, steel and concrete have not slipped in the shear interface, which was proved either by visual inspection as by LVDT recordings. This result is in accordance with outcomes from TS2.5_16_0.25 ($L_S/L = 1/4$) from Candido (2021).
b) The analytical model based concrete design presented here (MR1), which was employed to predict collapse loads during tests, was found to be in great accordance with experimental data from both TS2.5_16_0.33 and TS2.5_16_0.25 groups. Hence, full area of CFS lipped channel shuttering can be accounted to the final flexural strength of the slab system.
c) Both models MR1 and MR2 were found to be equally appropriate to predict the bending resistance of slab specimens according to experimental data.
d) The composite specimens from TS2.5_16_0.33 have showed to be 5 times more ductile than RCS2.5_16_0.33 ones due to strain capacity and cracking control introduced in the slab by the CFS shuttering at bottom ribs. This conclusion was based on the energy approach according to which the ductility corresponds to the area below the load-displacement curve until $80\%$ of the peak load.
e) In terms of bending moment, the presence of CFS lipped channel shuttering has soared the flexural capacity in $88\%$ when compared to an exact same slab with 210 mm of height, however with no incorporated formwork. Whereas the cold-formed section area is small, this contribution to design bending moment will be more expressive in thick floors where the moment arm is greater.
f) In terms of displacements, results from seven models found in the literature were compared to the actual load-displacement curves from experiments. Firstly, TS2.5_16_0.33 showed great accordance to M3 model from Souza-Neto (2001) until serviceability limit, which reduces the contribution of cracked inertia due to cracking control introduced by the CFS shuttering. On the other hand, TS2.5_16_0.25 samples were better represented by M7 from Costa et al. (2021) when close to $L/350$ only. However, all specimens were found to be well represented by displacement response

calculated with cracked moment of inertia $(I_{eff} = I_{II})$ in a conservative way, which is the easiest and most practical alternative to design in serviceability.

## 5.2 SUGGESTIONS TO FUTURE RESEARCH

The author leaves the following suggestions for future works:

a) Investigate the mechanism that allows for the shear behavior between the CFS profile and the concrete at bottom ribs and quantify its strength by pull-out tests.
b) Expand this research with the numerical modelling of this slab system through the FE Method taking into account different input parameters such as spacing between ribs, floor depth, rebar truss model, amount of additional reinforcement bars in ribs and concrete strength. As such, FE results can better evaluate the bending resistance sensibility to all variables.
c) Employ the FE results to validate the design equation employed in this research to calculate the sagging bending resistance.
d) Prepare and test slab samples with short spans to experimentally investigate the vertical shear failure mechanism.
e) Expand the experimental program to include and test hyperestatic samples cast with continuity over internal supports, such as double or triple spans. As such, the hogging bending resistance will be also investigated experimentally.
f) Evaluate the fire performance of such slabs.
g) After aforementioned steps, generate a catalogue with spans and corresponding load capacity.

## REFERENCES


ABAS, F. M. *et al*. Strength and serviceability of continuous composite slabs with deep trapezoidal steel decking and steel fibre reinforced concrete. **Engineering Structures**, v. 49, p. 866–875, 2013. Available at: <http://dx.doi.org/10.1016/j.engstruct.2012.12.043>.

AHMED, I. M.; TSAVDARIDIS, K. D. The evolution of composite flooring systems: applications, testing, modelling and eurocode design approaches. **Journal of Constructional Steel Research**, v. 155, p. 286–300, 2019. Available at: <https://doi.org/10.1016/j.jcsr.2019.01.007>.

ARCELORMITTAL BRASIL. **Telas Soldadas Nervuradas**. 2014. Available at: <https://brasil.arcelormittal.com/produtos-solucoes/construcao-civil/telas-soldadas-nervuradas>. Accessed on June 5th, 2021.

ARCELORMITTAL BRASIL. **Treliças Nervuradas**. 2017a. Available at: <https://brasil.arcelormittal.com/produtos-solucoes/construcao-civil/trelicas-nervuradas>. Accessed on June 5th, 2021.

ARCELORMITTAL BRASIL. **Trelifácil®**. 2017b. Available at: <https://brasil.arcelormittal.com/produtos-solucoes/construcao-civil/trelifacil>. Accessed on June 5th, 2021.

ARRAYAGO, I. *et al*. Experimental investigation on ferritic stainless steel composite slabs. **Engineering Structures**, v. 174, n. July, p. 538–547, 2018. Available at: <https://doi.org/10.1016/j.engstruct.2018.07.084>.

ASSOCIAÇÃO BRASILEIRA DE NORMAS TÉCNICAS - ABNT. **NBR 5738: Concreto - Procedimento para moldagem e cura de corpos de prova**. Rio de Janeiro, 2016. 9p.

ASSOCIAÇÃO BRASILEIRA DE NORMAS TÉCNICAS - ABNT. **NBR 5739: Concreto - Ensaio de compressão de corpos de prova cilíndricos**. Rio de Janeiro, 2018. 9p.

ASSOCIAÇÃO BRASILEIRA DE NORMAS TÉCNICAS - ABNT. **NBR 6118: Projeto de Estruturas de Concreto – Procedimento.** Rio de Janeiro, 2014. 238p.

ASSOCIAÇÃO BRASILEIRA DE NORMAS TÉCNICAS - ABNT. **NBR 8522: Concreto - Determinação dos módulos estáticos de elasticidade e de deformação à compressão**. Rio de Janeiro, 2017b. 20p.

ASSOCIAÇÃO BRASILEIRA DE NORMAS TÉCNICAS - ABNT. **NBR 8800: Projeto de estruturas de aço e de estruturas mistas de aço e concreto de edifícios.** Rio de Janeiro, 2008. 237p.

ASSOCIAÇÃO BRASILEIRA DE NORMAS TÉCNICAS - ABNT. **NBR 14762: Dimensionamento de estruturas de aço constituídas por perfis formados a frio.** Rio de Janeiro, 2010. 87p.

ASSOCIAÇÃO BRASILEIRA DE NORMAS TÉCNICAS - ABNT. **NBR 15823-2: Concreto autoadensável - Parte 2: Determinação do espalhamento, do tempo de escoamento e do índice de**

**estabilidade visual - Método do cone de Abrams**. Rio de Janeiro, 2017a. 5p.

ASSOCIAÇÃO BRASILEIRA DE NORMAS TÉCNICAS - ABNT. **ABNT NBR ISO 14025: Rótulos e declarações ambientais - Declarações ambientais de Tipo III - Princípios e procedimentos**. Rio de Janeiro, 2015. 29p.

BAI, L. *et al*. Longitudinal shear behaviour of composite slabs with profiled steel sheeting and ECC. **Engineering Structures**, v. 205, n. October 2019, p. 110085, 2020. Available at: <https://doi.org/10.1016/j.engstruct.2019.110085>.

BELTRÃO, A. J. N. **Comportamento Estrutural de Lajes-mistas com Corrugações na Alma de Perfis de Chapa Dobrada.** Dissertação (Mestrado) – Departamento de Engenharia Civil, Pontifícia Universidade Católica do Rio de Janeiro, Rio de Janeiro, 2003.

BRANSON, D. E. **Instantaneous and Time-dependent Deflections of Simple and Continuous Reinforced Concrete Beams**. Alabama: State Highway Department, 1963.

BRAUN, M.; HECHLER, O.; BIRARDA, V. 140 $m^2$ Column Free Space due to Innovative Composite Slim Floor Design. **9th International Conference on Steel Concrete Composite and Hybrid Structures.** United Kingdom, Leeds, 2009.

CANADIAN SHEET STEEL BUILDING INSTITUTE. **CSSBI S3: Criteria for the Design of Composite Slabs**. Cambridge, Ontario, Canada, 2017.

CANDIDO, D. C. M. **Análise experimental de laje nervurada treliçada com incorporação de fôrma intermitente em perfil formado a frio**. Dissertação (Mestrado) – Departamento de Engenharia Civil, Universidade Federal do Espírito Santo, Vitória, 2021.

COSTA, R. S. **Análise de um sistema de lajes mistas considerando a influência do atrito dos apoios e a avaliação do momento de inércia efetivo**. Dissertação (Mestrado) - Departamento de Engenharia de Estruturas, Universidade Federal de Minas Gerais, Belo Horizonte, 2009.

COSTA, R. S. *et al*. New equations to establish the effective moment of inertia of composite slabs with profiled steel sheeting for deflection calculation. **Journal of Building Engineering**, v. 37, p. 102-135, 2021. Available at: <https://doi.org/10.1016/j.jobe.2020.102135>

COUCHMAN, G; MULLETT, D; RACKHAM, J. **Composite Slabs and Beams Using Steel Decking: Best Practice for Design and Construction**. [S.l.]: The Metal Cladding & Roofing Manufacturers Association & The Steel Construction Institute, 2009.

CRISINEL, M.; O'LEARY, D. Recent Developments in Steel/Concrete Composite Slabs. **Structural Engineering International**, v. 6, n. 1, p. 41–41, 1996.

DANIELS, B. J.; CRISINEL, M. Composite slab behavior and strength analysis. Part I: calculation procedure. **Journal of Structural Engineering**, v. 119, n. 1, p. 16–35, 1993.

DAR, M. A. *et al*. Comparison of various shear connectors for improved structural performance in CFS concrete composite slabs. **Engineering Structures**, v. 220, n. 6, 2020. Available at:

<https://doi.org/10.1016/j.engstruct.2020.111008>.

DE ANDRADE, S. A. L. *et al*. Standardized composite slab systems for building constructions. **Journal of Constructional Steel Research**, v. 60, n. 3–5, p. 493–524, 2004. Available at: <https://doi.org/10.1016/S0143-974X(03)00126-3>

EUROPEAN COMMITTEE FOR STANDARDIZATION - CEN. **EN 1992-1-1: Eurocode 2 - Design of Concrete Structures - Part 1.1: General Rules and Rules for Buildings.** Brussels, Belgium, 2004.

EUROPEAN COMMITTEE FOR STANDARDIZATION - CEN. **EN 1994-1-1: Eurocode 4 - Design of composite steel and concrete structures - Part 1.1: General rules and rules for buildings.** Brussels, Belgium, 2004.

EUROPEAN COMMITTEE FOR STANDARDIZATION - CEN. **EN 15804:2012+A1:2013: Sustainability of construction works - Environmental product declarations - Core rules for the product category of construction products**. Brussels, Belgium, 2013.

FAVARATO, L. F. *et al*. Evaluation of the resistance of trussed slabs with steel formwork in cold formed U profile. **Latin American Journal of Solids and Structures**, p.1–20, 2019. Available at: <https://doi.org/10.1590/1679-78255304>.

FAVARATO, L. F. *et al*. Proposition of a simplified analytical design procedure for lattice girder slabs with shuttering in cold-formed steel lipped channel section. **IBRACON Structural and Materials Journal**, v.13, n.5, 2020. Available at: <https://doi.org/10.1590/S1983-41952020000500004>

FAVARATO, L. F. *et al*. **Full-interaction design of composite lattice girder slabs with cold-formed channel shuttering**. 2021. Full-length paper (unpublished). Federal University of Espírito Santo, Vitória, Brazil.

FERRAZ, C. B. **Análise do comportamento e da resistência do sistema de lajes mistas**. Dissertação (Mestrado) - Departamento de Engenharia de Estruturas, Universidade Federal de Minas Gerais, Belo Horizonte, 1999.

FERRER, M.; MARIMON, F.; CASAFONT, M. An experimental investigation of a new perfect bond technology for composite slabs. **Construction and Building Materials**, v. 166, p. 618–633, 2018. Available at: <https://doi.org/10.1016/j.conbuildmat.2018.01.104>.

GHOLAMHOSEINI, A. *et al*. Longitudinal shear stress and bond-slip relationships in composite concrete slabs. **Engineering Structures**, v. 69, p. 37–48, 2014. Available at: <http://dx.doi.org/10.1016/j.engstruct.2014.03.008>.

GHOLAMHOSEINI, A.; GILBERT, R. I.; BRADFORD, M. A. Long-term deformations in continuous composite concrete slabs. **Australian Journal of Structural Engineering**, v. 17, n. 3, p. 197–212, 2016. Available at: <http://dx.doi.org/10.1080/13287982.2016.1238531>.

GHOLAMHOSEINI, A. Experimental and finite element study of ultimate strength of continuous composite concrete slabs with steel decking. **International Journal of Advanced Structural Engineering**, v. 10, n. 1, p. 85–97, 2018. Available at: <https://doi.org/10.1007/s40091-018-0183-3>.

GOMES, A. V. S. **Finite Element Modelling Of a Cold-formed Steel Profile Employed In Composite Ribbed Slabs**. Dissertação (Mestrado) - Departamento de Engenharia Civil, Universidade Federal do Espírito Santo, Vitória, 2020.

GROSSI, L. G. F. **Sobre o comportamento estrutural e o dimensionamento de lajes mistas de aço e concreto com armadura adicional**. Dissertação (Mestrado) - Escola de Engenharia de São Carlos, Universidade de São Paulo, São Carlos, 2016.

GROSSI, L. G. F.; SANTOS, C. F. R.; MALITE, M. Longitudinal shear strength prediction for steel-concrete composite slabs with additional reinforcement bars. **Journal of Constructional Steel Research**, v. 166, 2020. Available at: <https://doi.org/10.1016/j.jcsr.2019.105908>.

HOLOMEK, J.; BAJER, M. Experimental and numerical investigation of composite action of steel concrete slab. **Procedia Engineering**, v. 40, p. 143–147, 2012. Available at: <https://doi.org/10.1016/j.proeng.2012.07.070>

HOSSAIN, K. M. A. *et al*. High performance composite slabs with profiled steel deck and Engineered Cementitious Composite – Strength and shear bond characteristics. **Construction and Building Materials**, v. 125, p. 227–240, 2016. Available at: <http://dx.doi.org/10.1016/j.conbuildmat.2016.08.021>.

JOHNSON, R. P. **Composite Structures of Steel and Concrete**. 3. ed. [S.l.]: Wiley, 2004.

LAUWENS, K. *et al*. On the shear resistance of ferritic stainless steel composite slabs. **Construction and Building Materials**, v. 189, p. 728–735, 2018. Available at: <https://doi.org/10.1016/j.conbuildmat.2018.09.003>.

LAWSON, R. M.; POPO-OLA, S. Load capacity of continuous decking based on small-scale tests. **Thin-Walled Structures**, v. 69, p. 79–90, 2013. Available at: <http://dx.doi.org/10.1016/j.tws.2013.03.011>.

MOHAMMED, K.; KARIM, I. A.; HAMMOOD, R. A. Composite slab strength determination approach through reliability analysis. **Journal of Building Engineering**, v. 9, n. 11, p. 1–9, 2017. Available at: <http://dx.doi.org/10.1016/j.jobe.2016.11.002>.

PEREIRA, M.; SIMÕES, R. Contribution of steel sheeting to the vertical shear capacity of composite slabs. **Journal of Constructional Steel Research**, v. 161, p. 275–284, 2019. Available at: <https://doi.org/10.1016/j.jcsr.2019.07.005>.

PORTER, M. L.; EKBERG, C. E. Design Recommendations for Steel Deck Floor Slabs. 3rd International Specialty Conference on Cold-Formed Steel Structures, Saint-Louis, Missouri, United States, p. 2121–2136, 1976.

QIAO, W. *et al*. Flexural properties of new cold-formed thin-walled steel and concrete composite slabs. **Journal of Building Engineering**, v. 31, n. 4, 2020. Available at:

<https://doi.org/10.1016/j.jobe.2020.101441>.

QUEIROZ, G.; PIMENTA, R. J.; MARTINS, A. G. **Estruturas Mistas - Volume 1**. 2ª edição. Rio de Janeiro: Centro Brasileiro da Construção em Aço - Instituto Aço Brasil, 2012.

RUSCH, H. Researches Toward a General Flexural Theory for Structural Concrete. **ACI Journal Proceedings**, v. 57, n. 7, 1960.

SIEG, A. P. A. **Estudo de um sistema de laje com fôrma de aço incorporada**. Dissertação (Mestrado) - Escola de Engenharia de São Carlos, Universidade de São Paulo, São Carlos, 2015.

SOLTANALIPOUR, M. *et al*. Shear transfer behavior in composite slabs under 4-point standard and uniform-load tests. **Journal of Constructional Steel Research**, v. 164, 2020. Available at: <https://doi.org/10.1016/j.jcsr.2019.105774>

SOUZA-NETO, A. S. **Análise do comportamento e da resistência de um sistema de lajes mistas com ancoragem de extremidade com considerações sobre a forma de aço isolada e o atrito nos apoios**. Dissertação (Mestrado) - Departamento de Engenharia de Estruturas, Universidade Federal de Minas Gerais, Belo Horizonte, 2001.

STARK, J. W. B.; BREKELMANS, J. W. P. M. Plastic design of continuous composite slabs. **Structural Engineering International: Journal of the International Association for Bridge and Structural Engineering (IABSE)**, v. 6, n. 1, p. 47–53, 1996.

TAKEY, T. H. **Sistemas de laje mista para edificações com uso de perfis de chapa metálica**. Dissertação (Mestrado) – Departamento de Engenharia Civil, Pontifícia Universidade Católica do Rio de Janeiro, Rio de Janeiro, 2001.

TENHOVUORI, A.; KARKKAINEN, K.; KANERVA, P. **Parameters and definitions for classifying the behaviour of composite slabs.** In: Composite Construction in Steel and Concrete III. ASCE, 1996.

TUPER. Catálogo da Tuper. [S.l.] Tuper, 2013. Disponível em: <https://www.tuper.com.br/lajes/#informacao-tecnica>. Accessed on June 6th, 2019.

VELJKOVIĆ, M. Influence of Load Arrangement on Composite Slab Behaviour and Recommendations for Design. **Journal of Constructional Steel Research**, v. 45, n. 2, p. 149–178, 1998. Available at: <https://doi.org/10.1016/S0143-974X(97)00055-2>

VIANNA, Juliana Cruz. **Sistema de laje-mista para edificações residenciais com o uso de perfis embossados de chapa dobrada**. Dissertação (Mestrado) – Departamento de Engenharia Civil, Pontifícia Universidade Católica do Rio de Janeiro, Rio de Janeiro, 2005.

VIANNA, J. C. *et al*. Um sistema de laje mista para edificações residenciais usando perfis de chapa dobrada com corrugações. **Rem: Revista Escola de Minas**, v. 60, n. 2, p. 325–331, 2007. Available at: <https://doi.org/10.1590/S0370-44672007000200015>

VIEIRA, J. D. **Estudo teórico-experimental do comportamento de laje mista com perfis**

**incorporados de chapa dobrada.** Dissertação (Mestrado) – Departamento de Engenharia Civil, Pontifícia Universidade Católica do Rio de Janeiro, Rio de Janeiro, 2003.

WALDMANN, D.; MAY, A.; THAPA, V. B. Influence of the sheet profile design on the composite action of slabs made of lightweight woodchip concrete. **Construction and Building Materials**, v. 148, p. 887–899, 2017. Available at: <https://doi.org/10.1016/j.conbuildmat.2017.04.193>

YI, O. *et al*. Push-off and Pull-out Bond Behaviour of CRC Composite Slabs – An Experimental Investigation. **Engineering Structures**, v. 228, n. 2, 2021. Available at: <https://doi.org/10.1016/j.engstruct.2020.111480>

ZHANG, H. *et al*. Long-term behavior of continuous composite slabs made with 100% fine and coarse recycled aggregate. **Engineering Structures**, v. 212, 2020. Available at: <https://doi.org/10.1016/j.engstruct.2020.110464>.

ZHU, X. *et al*. Properties of an innovative shear connector in a steel-concrete composite slab. **Journal of Constructional Steel Research**, v. 172, p. 106-165, 2020. Available at: <https://doi.org/10.1016/j.jcsr.2020.106165>.

# APPENDIX A
# PREPARATION OF EXPERIMENTS

**Figure A.1.** Preparation of wood formworks before concrete casting.
Source: Author.

(a) (b)

**Figure A.2.** Preparation of CFS shuttering, evidencing the connection to rebar truss.
Source: Author.

(a) (b) (c)

**Figure A.3.** (a) Weighting of slab components; (b) Assemblage under progress; (c) Assemblage completed.
Source: Author.



(a) (b) (c)

**Figure A.4.** Specific characteristics from preparation of specimens RCS2.5_16_0.33.
Source: Author.



(a) (b) (c)

**Figure A.5.** (a) Specimen molds before preparation; (b) and (c) Slump flow test.
Source: Author.

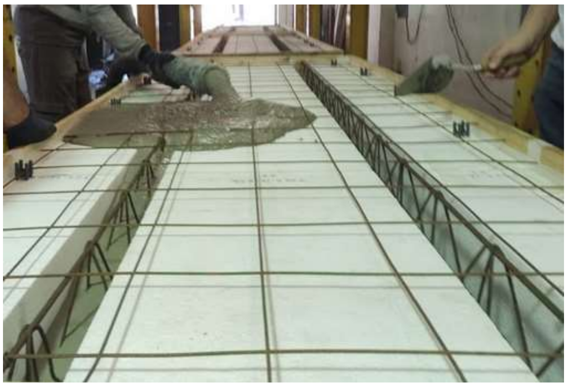


(a) (b)

**Figure A.6.** Concrete casting.
Source: Author.

(a) (b) (c)

**Figure A.7.** (a) and (b) Application of chemical curing agent to slab surface; (c) Protection with canvas.
Source: Author.

(a) (b) (c)

**Figure A.8.** (a) Concrete samples 1 day after molding; (b) Wet curing; (c) Chemical curing.
Source: Author.

(a) (b)

**Figure A.9.** (a) Propping removal; (b) Slab surface marking before installing instrumentation.
Source: Author.

(a) (b) (c)

**Figure A.10.** (a) and (b) Concrete surface preparation before installation of SG's; (c) SG's installed.
Source: Author.

(a) (b) (c)

**Figure A.11.** (a) SG addressed to steel; (b) Preparation of steel surface at bottom rib; (c) SG installed.
Source: Author.

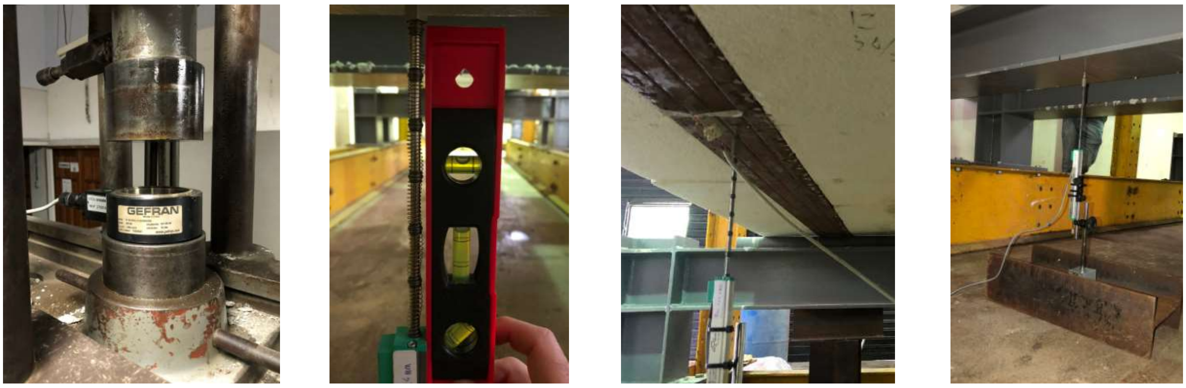


(a) (b) (c) (d)

**Figure A.12.** (a) Calibration of load cell before testing; (b) LVDT levelling; (c) Vertical LVDT installed at midspan; (d) Vertical LVDT installed under supports.
Source: Author.

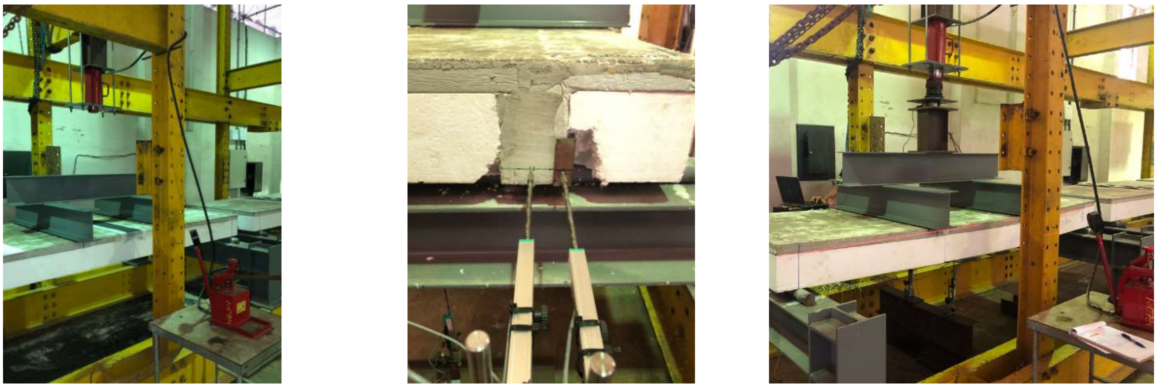

(a) (b) (c)

**Figure A.13.** (a) Assemblage of testing apparatus; (b) Horizontal LVDT’s placed at slab edges; (c) Sample after failure.
Source: Author.


(a) (b) (c)

**Figure A.14.** (a) Sample after failure; (b) Evidence of edge rotation; (c) Composite slab edge after testing (no end-slip recorded).
Source: Author.


(a) (b) (c)

**Figure A.15.** Calculation of concrete specific mass and weight.
Source: Author.

(a) (b) (c) (d)

**Figure A.16.** Concrete strength and secant modulus of elasticity tests.
Source: Author.

(a) Wet curing group. (b) Chemical curing group.

**Figure A.17.** Concrete specimens after testing, highlighting the difference in internal aspect due to different curing processes.
Source: Author.

**Figure A.18.** Removal of light filling blocks to evidence the cracking patterns of composite slabs (TS2.5_16_0.33).
Source: Author.

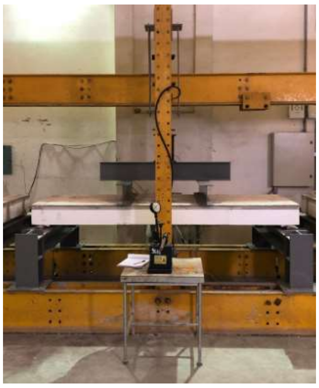


(a) (b)

**Figure A.19.** (a) Testing on reinforced concrete slab; (b) Crack at bottom rib.
Source: Author.


(a) (b)

**Figure A.20.** Removal of light filling blocks to evidence the cracking patterns of reinforced concrete slabs (RCS2.5_16_0.33).
Source: Author.


(a) (b)

**Figure A.21.** Demolition of slab samples in the Laboratory of Structures at UFES.
Source: Author.

# APPENDIX B
# CONCRETE SECANT MODULUS OF ELASTICITY

## B.1 – Group TS2.5_16_0.33

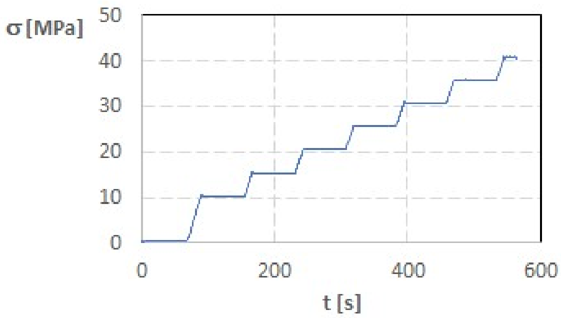


(a) Stress versus time.

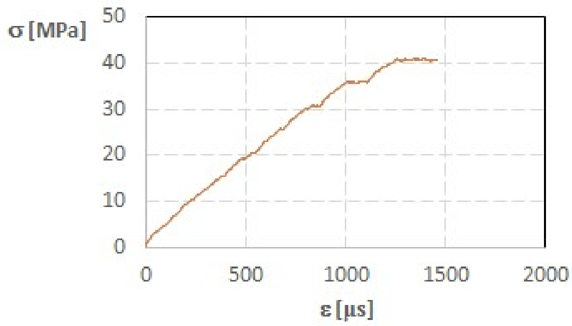


(b) Stress versus strain.

**Figure B.1.** Specimen WC_6.
Source: Author.


(a) Stress versus time.

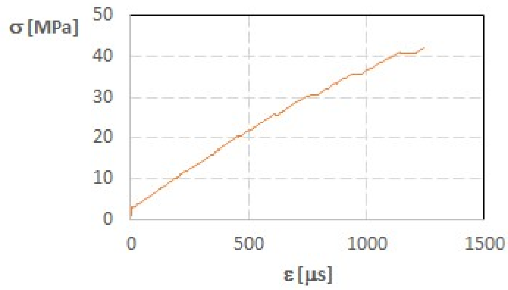


(b) Stress versus strain.

**Figure B.2.** Specimen WC_7.
Source: Author.

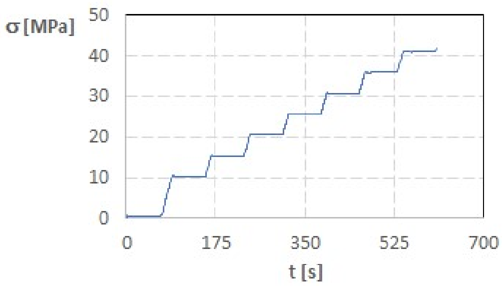


(a) Stress versus time.

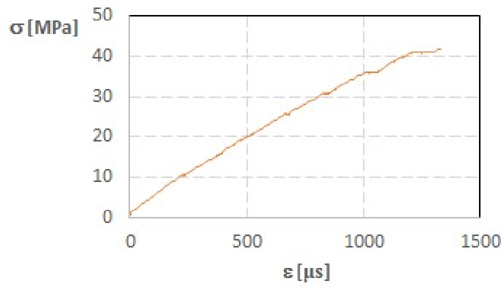


(b) Stress versus strain.

**Figure B.3.** Specimen WC_8.
Source: Author.

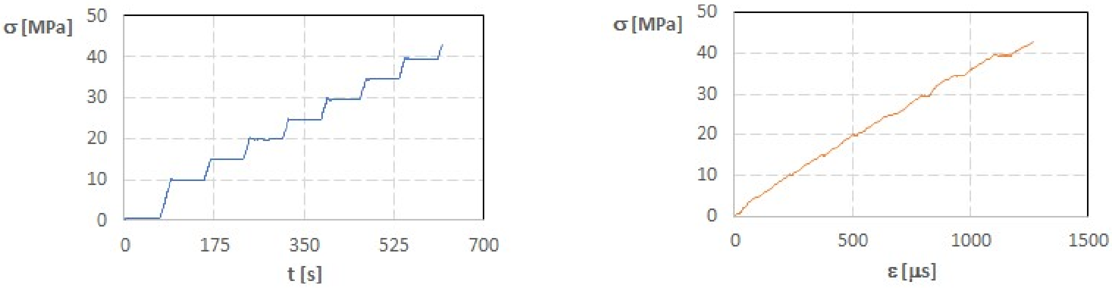


(a) Stress versus time. (b) Stress versus strain.

**Figure B.4.** Specimen WC_9.
Source: Author.

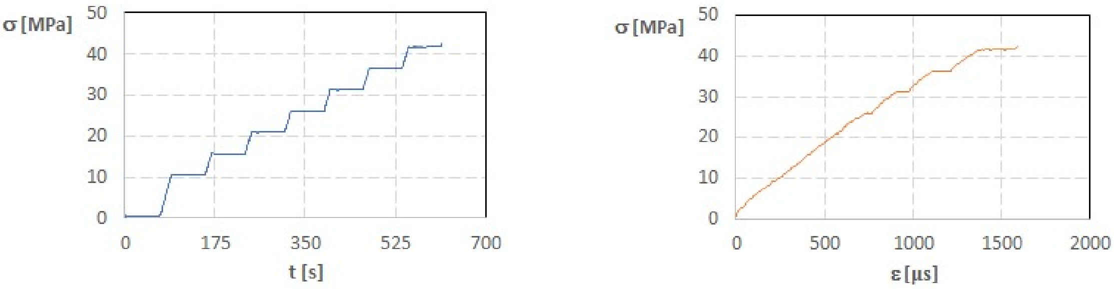


(a) Stress versus time. (b) Stress versus strain.

**Figure B.5.** Specimen CC_1.
Source: Author.

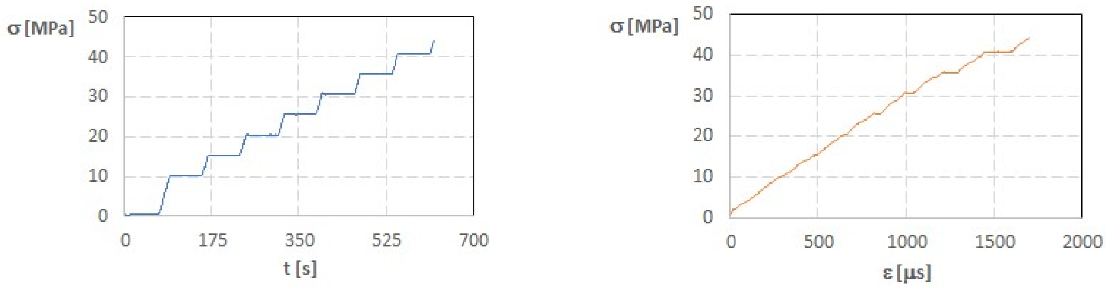


(a) Stress versus time. (b) Stress versus strain.

**Figure B.6.** Specimen CC_3.
Source: Author.

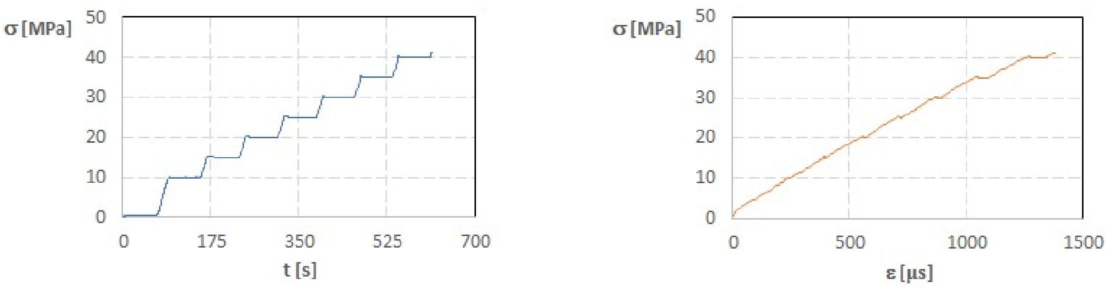


(a) Stress versus time. (b) Stress versus strain.

**Figure B.7.** Specimen CC_5.
Source: Author.

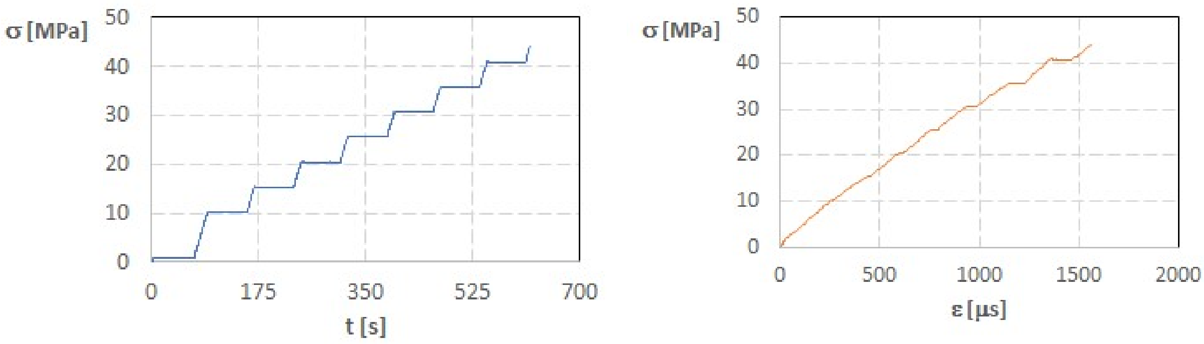


(a) Stress versus time. (b) Stress versus strain.

**Figure B.8.** Specimen CC_6.
Source: Author.

## B.2 – Group RCS2.5_16_0.33

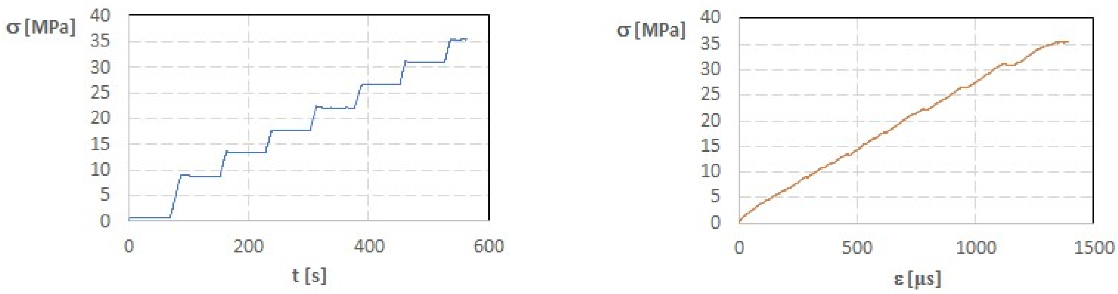


(a) Stress versus time. (b) Stress versus strain.

**Figure B.9.** Specimen WC_2.
Source: Author.

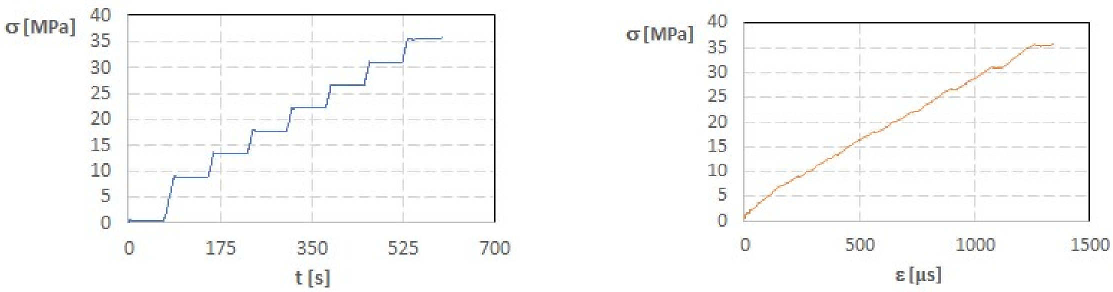


(a) Stress versus time. (b) Stress versus strain.

**Figure B.10.** Specimen WC_5.
Source: Author.

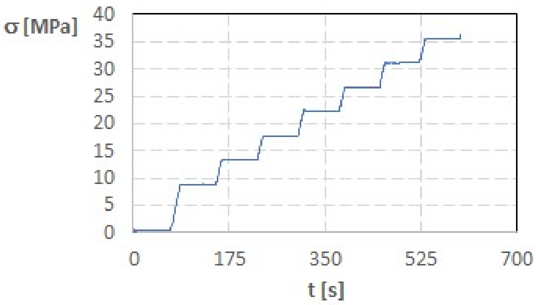


(a) Stress versus time.

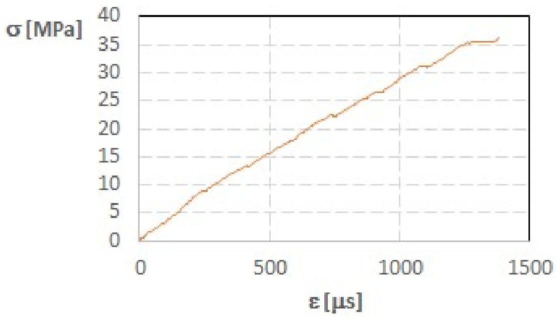


(b) Stress versus strain.

**Figure B.11.** Specimen WC_6.
Source: Author.

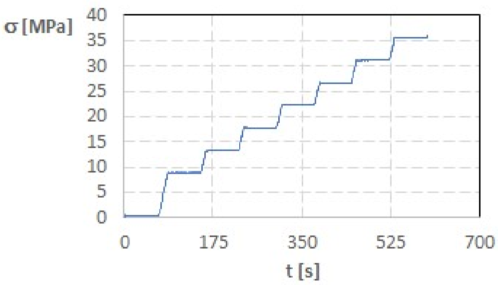


(a) Stress versus time.

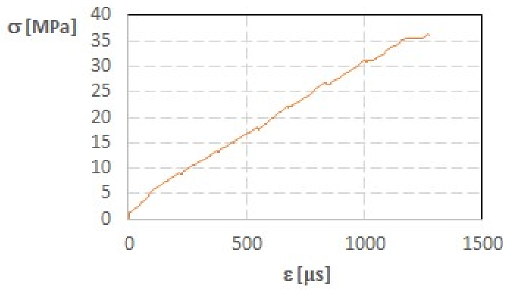


(b) Stress versus strain.

**Figure B.12.** Specimen WC_8.
Source: Author.

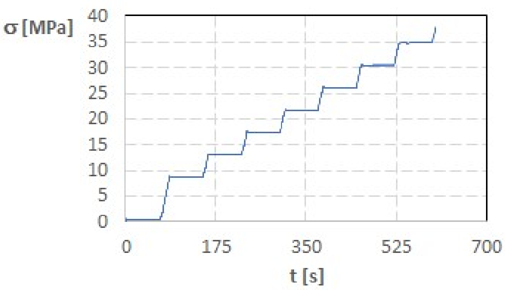


(a) Stress versus time.

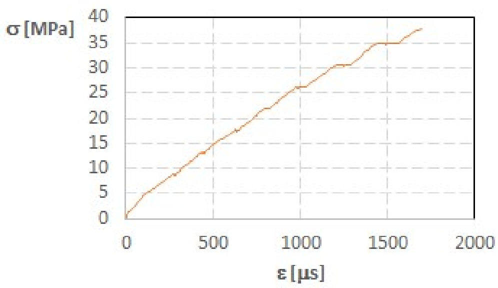


(b) Stress versus strain.

**Figure B.13.** Specimen CC_1.
Source: Author.

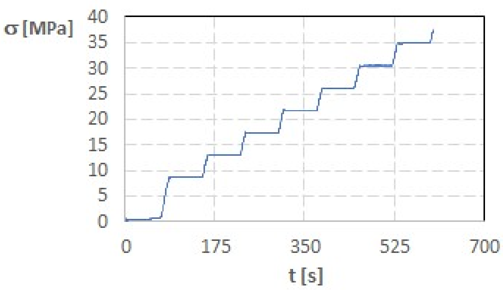


(a) Stress versus time.

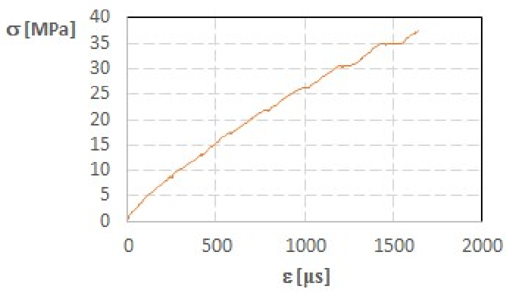


(b) Stress versus strain.

**Figure B.14.** Specimen CC_4.
Source: Author.

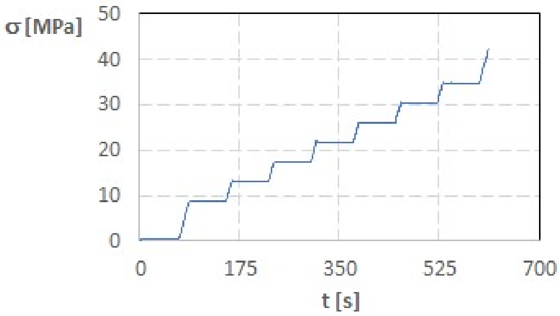


(a) Stress versus time.

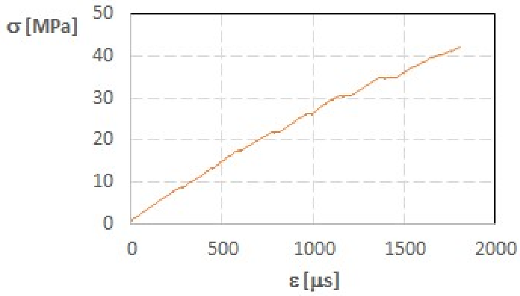


(b) Stress versus strain.

**Figure B.15.** Specimen CC_7.
Source: Author.

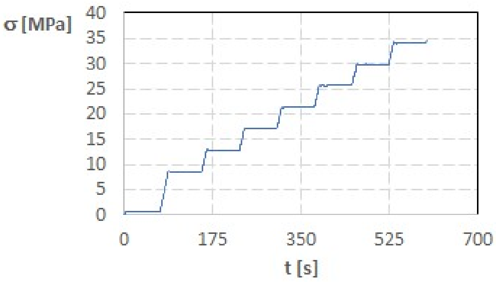


(a) Stress versus time.

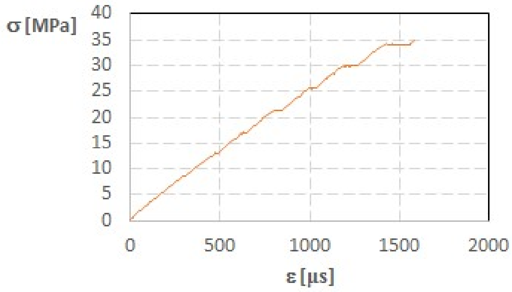


(b) Stress versus strain.

**Figure B.16.** Specimen CC_6.
Source: Author.